Crystalline, Rare-Earth-doped Sesquioxide and YAG PLD-Films

Dissertation

zur Erlangung des Doktorgrades
des Departments Physik
der Universität Hamburg

vorgelegt von
Yury Kuzminykh
aus Minsk

Hamburg
2006

Gutachter der Dissertation: Prof. Dr. G. Huber
Prof. Dr. D. Heitmann

Gutachter der Disputation: Prof. Dr. G. Huber
Prof. Dr. K. Sengstock

Datum der Disputation: 11.04.2006

Vorsitzender des Prüfungsausschusses: Dr. K. Petermann

Dekan der Fakultät für Mathematik,
Informatik und Naturwissenschaften: Prof. Dr. A. Frühwald

Vorsitzender des Promotionsausschusses: Prof. Dr. G. Huber

Abstract

Yury Kuzminykh, *Crystalline, Rare-Earth-doped Sesquioxide*
and YAG PLD-Films

This thesis presents the results of fabrication as well as structural and spectroscopic characterization of pulsed-laser-deposited oxide films. The fabricated films are activated by rare-earth ions and proven to be crystalline. Such films are promising for the fabrication of integrated optical devices or compact light sources. The application as active medium for thin disk lasers is considered as well.

The films produced include scandia (Sc_2O_3), yttria (Y_2O_3), lutetia (Lu_2O_3), ytterbia (Yb_2O_3) and yttrium-aluminum garnet ($Y_3Al_5O_{12}$) films with thicknesses in the range from 500 nm to 10 µm. Their structural properties have been investigated by means of X-ray diffraction. The influence of the deposition parameters on the characteristics of the scandia films has been investigated in more detail and the optimal deposition parameters have been determined.

The scandia films are highly textured along the <111>-direction and the crystallite dimensions reach several hundreds of nanometers. The lutetia films deposited under the same conditions demonstrate substantially smaller crystallites (<50 nm), which are mostly <111>-oriented. However, other orientations are also present in the diffraction patterns of the lutetia films.

The YAG films deposited at 700°C have been proven to be amorphous. After annealing at 1200°C the XRD analysis revealed a polycrystalline behavior of the Yb:YAG films and their spectroscopic properties resembled those of the bulk.

Waveguiding has been demonstrated in a 1.2 µm thick Eu:Y_2O_3 film as well as in 3 µm and 10 µm thick Nd:Sc_2O_3 films. The light propagation losses have been estimated to be 19.5 $dB\cdot cm^{-1}$ and 12 $dB\cdot cm^{-1}$, respectively, for the 3 µm and 10 µm Nd:Sc_2O_3 films. The excitation and emission spectra for the Nd:Sc_2O_3 films are close to those of the bulk material. The lifetime of the $^4F_{3/2}(Nd^{3+})$ multiplet in the scandia PLD-film is somewhat reduced compared to that in the bulk material.

Spectroscopic investigations of ytterbia as well as Yb-doped scandia, lutetia, and YAG films have been performed. For the ytterbia films the emission has only been detected at temperatures below 20 K. The spectra of the Yb:Sc_2O_3 and Yb:Lu_2O_3 films are bulk-like and vary slightly depending on the used substrate and the post annealing treatment (at 900°C). The luminescence quantum efficiency was up to 66% or up to 78%, respectively for the Yb-doped lutetia and scandia films.

Kurzfassung

Yury Kuzminykh, *Kristalline, Selten-Erd-dotierte Sesquioxid-
und YAG-PLD-Schichten*

Diese Arbeit präsentiert die Ergebnisse der Herstellung, sowie der strukturellen und spektroskopischen Untersuchungen der mittels Pulsed Laser Deposition hergestellten oxidischen Schichten. Die Schichten sind mit Selten-Erd-Ionen dotiert und weisen kristalline Struktur auf. Derartige Schichten können Anwendungen im Bereich der integrierte Optik finden. Auch der Einsatz als aktive Materialien für kompakte Lichtquellen und in Scheibenlasern ist möglich.

Es wurden Schichten mit Dicken im Bereich von 500 nm bis 10 µm aus den folgenden Materialien hergestellt: Scandium- (Sc_2O_3), Yttrium- (Y_2O_3), Lutetium- (Lu_2O_3) und Ytterbiumoxid (Yb_2O_3) sowie Yttrium-Aluminium-Granat ($Y_3Al_5O_{12}$). Die Struktur der Schichten wurde mittels Röntgenbeugung (XRD) untersucht. Für die Scandiumoxidschichten wurde der Einfluss der Herstellungsparameter auf die Schichteigenschaften untersucht.

Die Scandiumoxidschichten sind stark in <111>-Richtung orientiert und weisen Kristallitgrößen von einigen hundert Nanometern auf. Die Kristallite in unter gleichen Bedingungen hergestellten Lutetiumoxidschichten sind dagegen kleiner 50 nm. Die meisten dieser Kristallite sind <111>-orientiert, aber auch andere Orientierungen treten auf.

Die bei 700°C hergestellten YAG-Schichten sind amorph. Nach dem Tempern bei 1200°C haben XRD-Untersuchungen die polykristalline Struktur der Schichten bestätigt. Ihr spektrales Verhalten war ähnlich zu dem des entsprechenden Volumenkristalls.

Wellenleitung wurde in der 1.2 µm dicken $Eu:Y_2O_3$-Schicht sowie in den 3 µm und 10 µm dicken $Nd:Sc_2O_3$-Schichten experimentell nachgewiesen. Lichtausbreitungsverluste von 19.5 $dB \cdot cm^{-1}$ bzw. 12 $dB \cdot cm^{-1}$ wurden für die 3 µm bzw. 10 µm Wellenleitern ermittelt. Die Anregungs- und Emissionsspektren der Nd-dotierten Schichten ähneln denen des Volumenkristalls, wobei die Lebensdauer des $^4F_{3/2}(Nd^{3+})$-Multipletts in den Schichten etwas verkürzt ist.

Für die Ytterbiumoxidschichten ist die Emission nur bei Temperaturen unter 20 K gemessen worden. Die spektroskopischen Untersuchungen der Ytterbium-dotierten Scandium- und Lutetiumoxidschichten zeigen, dass deren Spektren denen der Volumenkristalle entsprechen, aber leicht von dem verwendeten Substrat und dem Nachtempern (900°C) abhängen. Die Lumineszenzquanteneffizienz erreicht den Wert von 66% für die $Yb:Lu_2O_3$ und 78% für die $Yb:Sc_2O_3$ Schichten.

Contents

Index of Figures

Index of Tables

List of Symbols and Abbreviations

Symbols

β	phase shift
$\beta_{i\rightarrow j}$	branching ratio coefficient
$\vec{B}$	magnetic field
c	speed of light in free space
$\mathrm{d}_{\text{targ-sub}}$	target-substrate distance
$\vec{D}$	electric displacement vector
$\vec{E}$	electric field
Φ	laser fluence
h,k,l	Miller indices
$\vec{H}$	magnetic flux density
$\vec{j}$	current density
$\vec{k}$	wave vector $(\lvert\vec{k}\rvert=\frac{2\pi n}{\lambda})$
λ	wavelength
$n_{\mathrm{0,f,s}}$	refractive index of superstrate, film, or substrate
$\mathrm{n}_{\mathrm{eff}}$	effective refractive index
ν_{laser}	pulse repetition rate of the laser
P_{O2}	oxygen pressure in deposition chamber
θ_{crit}	critical incidence angle
θ_{f}	incidence angle in film
ρ	charge density
$R^{\sigma,\pi}$	reflection coefficient for σ- and π-polarizations
$r^{\sigma,\pi}_{\mathrm{0f,fs}}$	Fresnel reflection coefficients at superstrate to film and film to substrate boundaries
$\tilde{r}^{\sigma,\pi}$	amplitude reflection coefficient for σ- and π-polarizations
σ_{em}	emission cross-section

τ	fluorescence lifetime
τ_{rad}	radiative lifetime
$\mathrm{T}_{\mathrm{sub}}$	substrate temperature
$t_{\mathrm{0f,fs}}^{\sigma,\pi}$	Fresnel transmission coefficients at superstrate to film and film to substrate boundaries
w_{inst}	width of the diffractometer instrumental function profile
w_{meas}	measured X-ray diffraction peak width
W_{nonrad}	nonradiative decay rate
w_{peak}	X-ray diffraction peak broadening
W_{rad}	radiative decay rate

Abbreviations

AFM	atomic force microscopy
CCD	charge-coupled device
CT	charge transfer (state)
CVD	chemical vapor deposition
EBV	electron beam evaporation
FWHM	full width at half maximum
GGG	gadolinium-gallium garnet ($Gd_3Ga_5O_{12}$)
HEM	heat-exchanger method
IAD	ion assisted deposition
KGW	potassium-gadolinium tungstate ($KGd(WO_4)_2$)
LPE	liquid phase epitaxy
MBE	molecular beam epitaxy
NA	numerical aperture
OPO	optical parametric oscillator
PLD	pulsed laser deposition
RE	rare earth
RHEED	reflection high energy electron diffraction

SEM	scanning electron microscopy
TE	transverse electric polarization
TM	transverse magnetic polarization *OR* transition metal
TMM	transfer matrix method
XRD	X-ray diffraction
YAG	yttrium-aluminum garnet ($Y_3Al_5O_{12}$)
YAM	yttrium-aluminum monoclinic phase ($Y_4Al_2O_9$)
YAP	yttrium-aluminum perovskite ($YAlO_3$)

Chapter 1. Introduction

§1.1 Motivation

Nowadays, most of the principal optical devices – like light generators, detectors, transmitters, splitters, etc – have been demonstrated. Currently, research is focused on reducing the dimensions of these devices and implementing them as structural elements in integrated optical systems. Hence, new techniques need to be developed for fabrication of such systems with dimensions of the individual element down to the micrometer range. One of the possibilities is to structure or modify the volume material, however, this approach is not flexible enough. A number of well-established deposition techniques should be more favorable, since a number of layers as well as several materials can be easily combined. Subsequently, the layers can be structured or deposition through a mask can be employed in order to realize two- or three-dimensional configurations.

The general tendency is to reduce the size of optical devices even if discussed in other contexts than integrated optics. For example, compact light sources are required for sensing applications, spectroscopy or analytical techniques. From this point of view devices based on waveguides are very promising. Possible applications of waveguiding films are discussed more thoroughly in chapter 6.

Lately, solid-state lasers attracted increased attention induced by the invention of the thin disk laser set-up. This concept improves the performance of high-power laser by decreasing the dimensions of the active medium in order to reduce thermal stress. The typical thickness of the active media is, currently, in the range of several hundreds of micrometers, and it is desirable to utilize even thinner layers. Thus, films of active material with the thickness in the range of tens or hundreds micrometers can find their application as active media in solid-state thin disk lasers. The application of deposition techniques can be especially favorable in this case, since the active medium, Bragg mirrors and antireflection coatings can be fabricated as a multilayer structure in a single process. Also periodic structures with photonic properties (e.g. microcavities) can be produced in a similar way. A more detailed introduction into the subject of thin disk lasers and layered structures is given in chapter 7.

The starting point for the fabrication of the devices discussed above is the deposition of films of a suitable material. Both the deposition technique and the material have to comply with some requirements. The optical properties of the material, as, for example, transparency in a certain wavelength range or the refractive index are important issues, but also mechanical, chemical, or thermal properties can be critical for certain applications. With respect to active devices, the spectroscopic properties of the material are to be considered as well.

Rare-earth-doped oxides are one of the most successful classes of active media for solid-state lasers. The only more widespread class of laser materials are semiconductors, which gained their popularity due to the capability to be electrically pumped, compactness, and very low fabrication cost. However, dielectric oxide materials demonstrate some properties that make them advantageous for certain applications. They are insulators with a wide band gap and therefore transparent in the wide wavelength range from ultraviolet to mid-infrared. Oxides reveal excellent chemical and mechanical properties and do not show deterioration. Another advantage follows from the difference in the operation principle of semiconductor and solid-state lasers. The absorption and emission in semiconductors results from band-to-band transitions and energy is stored in separated electrons and holes, which are not or only weakly localized. In dielectric laser media, transitions between the energy levels of a dopant ion occur and, thus, the excitation states are typically localized. Exceptions can occur in the case of very high doping concentrations. This situation is discussed in chapter 7. Hence dielectric materials set less strict requirements for the density of defects (which can lead to undesired deexcitation) and, consequently, for the deposition parameters and the substrate choice. Therefore, the required quality of the film should be easier to achieve in this case.

Other dielectric solid-state host materials (like fluorides, borates, tungstates, vanadates, etc.), even if superior to oxides in the spectroscopic or performance characteristics, are usually inferior to them in thermal conductivity, mechanical stability or growth simplicity and scalability. This determines the prevalence of oxides as host materials in the solid-state laser domain.

A number of different techniques can be employed for the deposition of oxide materials, including electron beam evaporation (EBV), chemical vapor deposition (CVD), molecular beam epitaxy (MBE), ion-assisted deposition (IAD), RF magnetron sputtering, and sol-gel methods. Recently, pulsed laser deposition (PLD) proved to be a favorable technique for the deposition of oxides. Its advantages are high ionization degree and high energy of the plasma species (up to 100 eV), which positively influence the films properties like density, crystallinity, and adhesion to the substrate. PLD is a very versatile technique. On the one hand it is possible to control the thickness of the film at the atomic layer scale and on the other hand pulsed-laser-deposited films with thicknesses exceeding 100 μm have been demonstrated. Adjusting the parameters of the process (laser wavelength, energy density, background atmosphere, substrate, etc.), the PLD technique can be adapted for the deposition of a wide range of materials, going far beyond the oxides discussed in this thesis. The material range expands from metals to multicomponent inorganic materials (like $YBa_2Cu_3O_{7-x}$) to polymers and complex organic molecules (like proteins). Additionally, the nonthermal character of the process allows to control the stoichiometry of the deposited material. The use of a relatively small amount of material for the target as well as the possibility of quick change of materials or parameters makes the PLD technique quite convenient from the experimental point of view.

§1.2 Overview and Structure of this Thesis

This thesis is structured in the following way. Chapter 2 gives a short overview of the properties of the materials used throughout this work. They include sapphire and quartz, used as substrates, as well as sesquioxides (scandia, yttria, ytterbia, and lutetia) and yttrium aluminum garnet. These materials have been used both for film fabrication and as substrates.

Then, in chapter 3 the description of the analytical techniques and experimental set-ups, which have been employed the for characterization of the fabricated PLD-films, is given. The techniques include X-ray diffraction analysis, scattering measurements using an integrating sphere, reflectometry and ellipsometry, as well as various spectroscopic methods.

In chapter 4 the fabrication process of the PLD-films is described. Also a short comparison with other deposition techniques is given and their advantages and disadvantages are discussed. The properties of the scandia PLD-films fabricated under different conditions are compared here as well.

The results of the structural characterization of the films produced in the course of this work by means of X-ray diffraction are discussed in chapter 5. The investigated films include ytterbia, as well as Yb-doped scandia, lutetia, and YAG. The spectroscopic properties of the films are discussed later in chapter 7 in the context of their possible application.

The sesquioxide PLD-films that showed waveguiding are considered in chapter 6. The spectroscopic and waveguiding properties of the films have been investigated, as well as the possible propagation loss mechanisms. The films are doped with rare-earth ions and their possible application in the integrated optics or for the realization of waveguide lasers is discussed. The experimental set-up for characterization of waveguides is described this chapter together with the experimental results.

Chapter 7 presents the results of spectroscopic investigations on the Yb-doped sesquioxide and YAG films. It also introduces the concept of the thin disk laser and discusses the possibility of the application of Yb-doped PLD-films as active media for such lasers.

Finally, in chapter 8 all the experimental results are summarized and their impact on the future work is discussed.

Chapter 2. Materials

This chapter gives an overview on the properties of the materials used either for film fabrication or as substrates in the course of this work. The spectroscopic and structural properties of sesquioxide (scandia, yttria, ytterbia, and lutetia) PLD-films is the main investigation topic of this thesis. These materials were also grown as bulk crystals and used as substrates. Further, properties of yttrium aluminum garnet (YAG) are described. The Yb-doped YAG PLD-films are discussed in chapter 7. Finally, relevant sapphire and quartz properties are presented. These materials are used as substrates throughout this work. The key characteristics are summarized in a table form at the end of this chapter.

§2.1 Sesquioxides

Sesquioxides, as it can be derived from their name, are oxide materials with anion to cation ratio equal 1.5 (from Latin "sesqui" – one and a half). Normally oxides of the rare-earth elements (the third group of the periodic table) are referred to as sesquioxides. Within the framework of this theses scandia, yttria, ytterbia and lutetia are discussed. Yttria is the most studied and widely used material of this class, mostly due to the wide application of Eu:Y_2O_3 as a red phosphor. Scandia and lutetia have been also paid much attention lately, as a possible laser host matrix [For99a].

The crystallographic structure of the sesquioxides depends on temperature, pressure and the cation radius [Hoe66, Rot60]. At the normal conditions scandia (Sc_2O_3), yttria (Y_2O_3), and lutetia (Lu_2O_3) form the same cubic C-type bixbyite structure (see figure 2.1). This structure is stable up to the melting point for scandia and lutetia, for yttria it changes to a hexagonal phase slightly below the melting point. The lattice

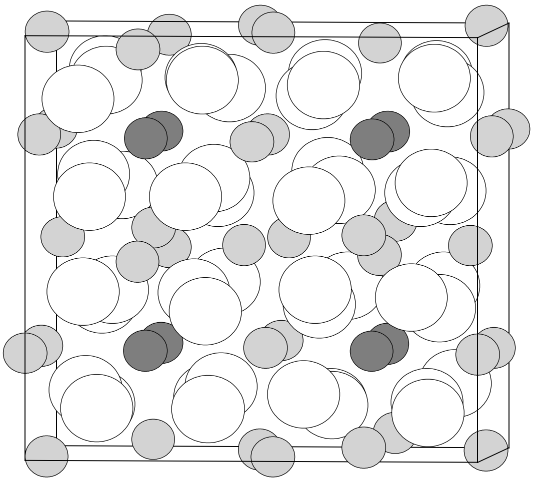

Figure 2.1: Crystal structure of cubic sesquioxides viewed nearly in <100>-direction. (white – O^{2-}, gray – $RE^{3+}(C_2)$, dark gray – $RE^{3+}(C_{3i})$).

constants are in the range of 10Å[1]. A unit cell of the bixbyite structure contains 16 formula units (80 atoms). 24 cation sites of the unit cell have C_2-symmetry and 8 cation sites have C_{3i}-symmetry, both six-fold coordinated with oxygen. The two-fold axes of the C_2-sites are oriented along the <100>-direction, the three-fold axes of the C_{3i}-sites along <111>-direction. Chemical bonds in sesquioxides have ionic character with some part of covalent bonding. Due to the identical crystal structure and relatively close ionic radii of cations, mixed sesquioxide crystals can also be produced. This mixtures, e.g. $LuScO_3$, can be used for tuning of a specific parameter as, for example, the lattice constant.

Scandia, yttria, and lutetia are insulators with a band gap of approximately 6 eV. It means that they are transparent up to the ultraviolet region (~200 nm). Detailed investigation can be found in [Abr78, Tom86]. Band structure calculations of yttria have been performed by Xu *et al.* [Xu97]. The conduction band is formed by 4d and 5p electron orbitals of Y^{3+} ions, whereas the valence band is mainly formed by the 2p orbital of oxygen ions with small contribution of yttrium 4d and 5p states. Up to now, no investigations of the electronic structure of scandia or lutetia can be found in the literature.

The fact, that the sesquioxides can be doped with rare-earth elements, is their most important property for laser applications. The first

---

[1] Here and further in this section the properties of scandia, yttria, ytterbia, and lutetia are discussed in general, see table 2.2 for the values of the specific parameters. The physical and chemical properties are of ytterbia (not given in the table) are close to that of lutetia.

investigations of spectroscopic and lasing properties of rare-earth-doped sesquioxides go back up to the late fifties [Bar57, Lev62]. The first published data on the stimulated emission in the $Eu^{3+}:Y_2O_3$ can be found in [Cha63]. The first laser operation of $Nd^{3+}:Y_2O_3$ have been demonstrated by Hoskins and Soffer [Hos64]. Thorough investigations of spectroscopic and lasing properties of rare-earth-doped sesquioxides can be found in the theses of E. Mix [Mix99], L. Fornasiero [For99] and V. Peters [Pet01].

The sesquioxides reveal excellent mechanical and chemical stability. Mohs hardness is in the range of 6-7. They are only dissolved in hydrofluoric acid and hot phosphoric acid. Sesquioxides also show quite high thermal conductivity, which even excels that of YAG, which is a widely used laser host material. This can be favorable for high-power laser applications. Average phonon energy in sesquioxides is quite low for oxide materials, which is especially beneficial for application as a host material for up-conversion lasers in the visible range, since higher phonon energies lead to faster deexcitation of the excited states.

2.1.1 Growth of Sesquioxide Crystals

Overview of Crystal Growth Techniques

Despite of the fact, that sesquioxides (and especially yttria) are well investigated and some their optical properties are quite favorable for laser applications, sesquioxide bulk crystals or substrates are not commercially available up to now. This is mainly caused by their very high melting temperature (~2400°C), which hinders the growth of large volume, stress and impurity free single crystals. Up to the end of the nineties no acceptable technique for growth of high quality sesquioxide crystals were available. Most properties of the sesquioxides have been investigated on the crystals grown by various techniques listed below, but neither of them was completely acceptable for some reasons (see [Mix99, For99, Pet01] for more detailed discription):

- ◊ flame-fusion-technique (crystals reveal strong stress, high defects density in the crystalline structure)

- ◇ scull-melting (crystallization starts from many points, so a large number smaller crystals are grown simultaneously)
- ◇ floating-zone-technique (small volume of grown crystals)
- ◇ Czochralski- and Nacken-Kyropoulos-method (small volume, due to problems with the heat abstraction at the high temperatures)

Better results can be obtained by utilizing Bridgman and, derived from it, heat-exchanger method (HEM). The latter have been employed in the course of this work to grow bulk sesquioxide crystals, which have been used for fabrication of substrates as well as for reference measurements. In detail, the application of HEM for growth of sesquioxides is discussed in [Mix99, For99, Pet01, Pet02a]. Below a short description of this method is given.

Heat-Exchanger Method (HEM)

A scheme of the used HEM crystal growth set-up is presented in figure 2.2. Due to the high melting temperature of sesquioxides, the number of the possible materials for the crucible and the insulation is quite limited. The best results have been achieved with rhenium crucibles, which were produced either by galvanic method or by pressing and sintering rhenium powder. No material was found to withstand the direct

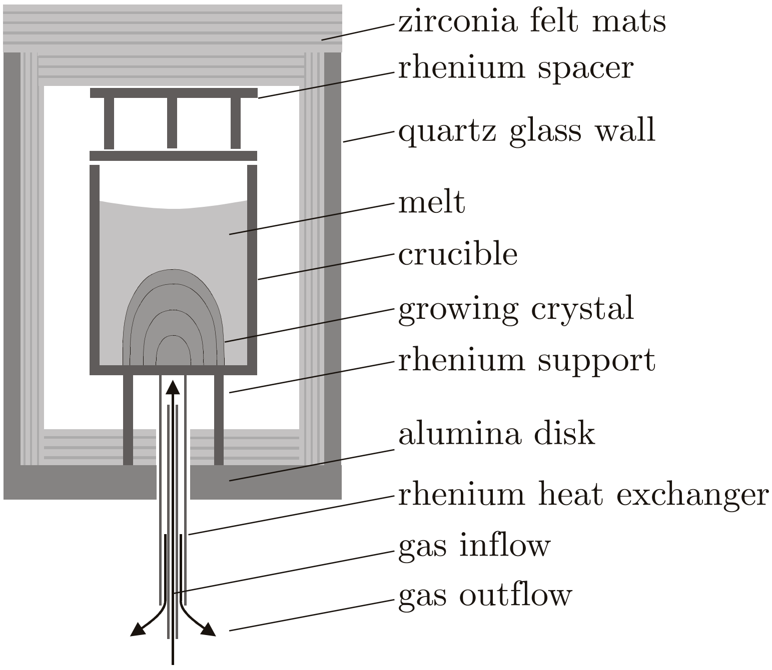

Figure 2.2: Scheme of the HEM crystal growth set-up.

contact with the crucible at the necessary temperatures without reacting. Thus the crucible was placed on the rhenium support completely surrounded by gas in a cell made of zirconia felt mats. The whole set-up was installed on alumina ceramic disk and was stabilized by the surrounding quartz glass tube.

The crucible was heated inductively through a water-cooled coil, which encircled the whole set-up and was powered by a high frequency generator (400 kHz, up to 36 kW). The crystal growth proceeds as follows: first the generator power is increased till source material is molten, then flow rate of the gas passing through the heat-exchanger under the crucible, is gradually raised. Thus, crystallization starts from the bottom of the crucible and the crystallization front gradually moves upwards during the growth process. In order to obtain large volume single crystals a seed can be used, however if large volume of source material is utilized, crystals of acceptable size can be grown without a seed. This noticeably simplifies the technique, since no precise temperature control is required in this case.

In the course of this work crystals of scandia, yttria, and lutetia have been grown, as well as a mixed scandium-lutetium oxide ($ScLuO_3$) crystal. The crystals were polycrystalline, since no seed was used. Larger single crystals have been separated and oriented using a Laue experimental set-up. Subsequently, they have been cut parallel to (111)-crystallographic plane and commercially formed and polished by CrysTec GmbH (Berlin, Germany). These substrates were then used for homoepitaxial growth of sesquioxide films.

§2.2 Yttrium-Aluminum Garnet

Yttrium aluminum garnet (YAG) is the most known modification of a large group of artificial materials named garnets. The common composition formula for garnets is $A_3B_2C_3O_{12}$, where A, B, and C denote crystallographic sites with different O^{2-} environment (see table 2.2 for details), and in the case of YAG the sites are occupied as follows: A=Y^{3+}, B/C=Al^{3+}. Garnets form a cubic, body centered lattice (space group

Ia3d). The unit cell of YAG contains eight $Y_3Al_5O_{12}$ units. Nowadays, YAG one is of the most important hosts for rare-earth-doped materials as, for example, Nd:YAG or Yb:YAG. Many of commercially produced solid-state lasers are based on this material. Apart from its favorable spectroscopic properties, also its high thermal conductivity, mechanical stability, and high optical damage threshold stimulated its wide application. YAG is an insulator with a band gap of 6.5 eV. Calculation of its electronic structure have been recently performed by Xu and Ching [Xu99, Chi99]. One can also consider YAG as a congruent mixture of two oxides (Y_2O_3 and Al_2O_3). Two more congruent compositions of the Y-Al-O system exist: $YAlO_3$ (YAP), which forms a perovskite orthorhombic crystalline lattice and $Y_4Al_2O_9$ (YAM), having a monoclinic lattice. YAP is also sometimes utilized as a host for rare-earth dopants, but in general YAP and YAM are less widely used as YAG.

§2.3 Corundum (Sapphire)

Depending on the conditions, aluminum oxide can form several crystalline structures. The most known is the α-form termed corundum. The matrix itself is colorless, but natural corundum often contains impurities, which are responsible for its coloration. The red (Cr^{3+}-doped) variation is called ruby and all the other colors – sapphire. However the mineralogical term sapphire is also widely used for pure α-Al_2O_3 along with the term corundum.

The unit cell of α-Al_2O_3 has trigonal symmetry and contains two Al_2O_3 units. Alternatively the α-Al_2O_3 lattice can be presented as a hexagonal structure. The oxygen ions build hexagonal close-packed (hcp) lattice and the aluminum ions take octahedrally coordinated intersites. α-Al_2O_3 is an insulator with a band gap of 9.5 eV. The fundamental absorption edge is however overlapped by an absorption of an excitonic state. Also, due to always present Cr^{3+}-impurities, absorption into a charge-transfer state [Fre90] is observed below the band gap of α-Al_2O_3. Details on the electronic structure of corundum can be found in [Xu91].

§2.4 Quartz

Quartz, a form of SiO_2, is a very widespread mineral (12% in the Earth's crust). Pure quartz is fully transparent, whereas natural quartz can have some coloration due to impurities. From the crystallographic point of view quartz is an α-form of silica. Depending on temperature and pressure, silica can exist in a large number of other modifications, which include β-quartz, tridymite, cristobalite, coesite, stishovite, and keatite. Thus, the α-quartz and the β-quartz should be distinguished. In the framework of this theses, where not explicitly noted, the α-form of silica is meant under the name of quartz.

The unit cell of the α-quartz lattice contains three SiO_2 units. The lattice has trigonal symmetry and is acentric, which means that two modifications (right-hand and left-hand) of the α-quartz crystalline lattice exist. The fact, that quartz is optically active, is explained by this property of the lattice.

When heated over 573°C at atmospheric pressure α-quartz transforms into β-quartz. The transformation into the β-phase is associated with slight displacements of the ions, without breaking the chemical bonds. The lattice of β-quartz has hexagonal symmetry and is center symmetric. When the temperature is lowered, the transition back into the α-phase takes place, which is associated with a small but rapid change of the lattice constant and the reduction of the lattice symmetry. This can lead to stress, due to formation of right and left-hand oriented domains. The deposition of oxide materials normally requires high substrate temperatures during the deposition (up to 700°C have been used within this work). The phase transition back to the α-quartz hinders application of quartz as a material for substrates, since the mechanical stress can cause the cracking of the deposited film. Even cracking of the substrate itself have been observed in some cases during this work. Therefore quartz substrates have been avoided in the later phase of this work. More thoroughly the application of quartz substrates for deposition of sesquioxide PLD-films has been investigated by S. Ehlert in his diploma theses [Ehl05].

§2.5 Summary of Material Properties

This section summarizes the essential properties and parameters of the oxide material discussed above in this chapter. Table 2.1 presents Sellmeier equations for this materials. In table 2.2 the other material characteristics are collected [Mix99, For99, Pet01, Bär04].

Table 2.1. Sellmeier equations (λ in μm).

Sc_2O_3	$n=\sqrt{3.83252+\frac{0.0492688}{\lambda^2-0.0237987}-0.014094\lambda^2}$	[Mix99]
Y_2O_3	$n=\sqrt{3.5387+\frac{0.0421725}{\lambda^2-0.0243226}-0.00914896\lambda^2}$	[Mix99]
Lu_2O_3	$n=\sqrt{3.83252+\frac{0.0492688}{\lambda^2-0.0237987}-0.014094\lambda^2}$	[Mix99]
YAG	$n=\sqrt{1+\frac{2.28200\lambda^2}{\lambda^2-0.01185}+\frac{3.27644\lambda^2}{\lambda^2-282.734}}$	[Zel98]
α-Al_2O_3	$n_o=\sqrt{1.5586+\frac{1.52365\lambda^2}{\lambda^2-0.01097}+\frac{5.36043\lambda^2}{\lambda^2-325.66}}$ $n_e=\sqrt{1.78106+\frac{1.27616\lambda^2}{\lambda^2-0.01242}+\frac{0.33939\lambda^2}{\lambda^2-17.03}}$	[NDL]
α-SiO_2	$n_o=\sqrt{1.30979+\frac{1.04683\lambda^2}{\lambda^2-0.01025}+\frac{1.20328\lambda^2}{\lambda^2-108.584}}$ $n_e=\sqrt{1.32888+\frac{1.05487\lambda^2}{\lambda^2-0.01053}+\frac{0.97121\lambda^2}{\lambda^2-84.261}}$	[NDL]

Table 2.2. Summary of material properties.

Name	**Scandia**	**Yttria**	**Lutetia**	**Yttrium-Aluminum Garnet**	**Sapphire**	**Quartz**
Formula	Sc_2O_3	Y_2O_3	Lu_2O_3	$Y_3Al_5O_{12}$	α-Al_2O_3	α-SiO_2
Crystal structure	cubic	cubic	cubic	cubic	trigonal/ hexagonal	trigonal/ hexagonal
Symmetry	Ia3 (T^7_h)	Ia3 (T^7_h)	Ia3 (T^7_h)	Ia3d (O^{10}_h)	R3c (D^5_{3d})	P31 2 1
Lattice constant [Å]	9.857	10.603	10.391	12.003	4.762 (a) 12.989 (c)	4.914 (a) 5.405 (c)
Density [$\frac{g}{cm^3}$]	3.847	5.03	9.42	4.5	3.99	2.2
Hardness (Mohs)	~6.8	6.8	~7	~8.5	9	7
Melting temperature [°C]	~2430	2430	~2450	1930	2040	1550
Thermal conductivity [$\frac{W}{m\cdot K}$]	17	14	13	11	46	
Thermal expansion coefficient [10^{-6} K^{-1}]	9.6	7.9	8.6	6.9	5.3 (‖c) 4.5 (⊥c)	
Maximal phonon energy [cm^{-1}]	672	597	618	857	950	
Possible doping	RE	RE	RE	RE, TM	TM	-
Site symmetry (coordination number)	$C_2(6)$ $C_{3i}(6)$	$C_2(6)$ $C_{3i}(6)$	$C_2(6)$ $C_{3i}(6)$	$D_2(8)$ /Y^{3+}, $C_{3i}(6)$ /Al^{3+}, $S_4(4)$ /Al^{3+}		
Refractive index (at 1 μm)	1.967	1.89	1.911	1.816	1.756(n_o) 1.747(n_e)	1.535(n_o) 1.544(n_e)
Transparency range [μm]	0.21..8	0.21..8	0.22..8	0.22..6	0.14..6.5	0.18..2.5
Density of RE-cations [10^{22} cm^{-3}]	3.355	2.687	2.852	1.38	-	-

Chapter 3. Analytical Techniques

In this chapter the analytical methods and experimental set-ups employed throughout this work are described. They include X-ray diffraction, reflectometry and ellipsometry, as well as spectroscopic techniques, such as emission, excitation, and lifetime measurements.

§3.1 X-Ray Diffraction

Theory

The X-ray diffraction (XRD) is a non-destructive technique, which allows to examine the crystalline structure of the material. It is based on analyzing the angular intensity distribution of the monochromatic X-rays reflected from the sample. When the X-rays propagate through the material, they are scattered at electrons in the atomic shells. If atoms are chaotically arranged in the space (e.g. amorphous material), the scattered X-rays are incoherent and the resulting intensity is proportional to the total number of scattering centers N. In case atoms are arranged in periodic structure (e.g. crystal) and the path differences for the X-rays scattered from the individual atoms is multiple to wavelength λ, positive interference of the scattered

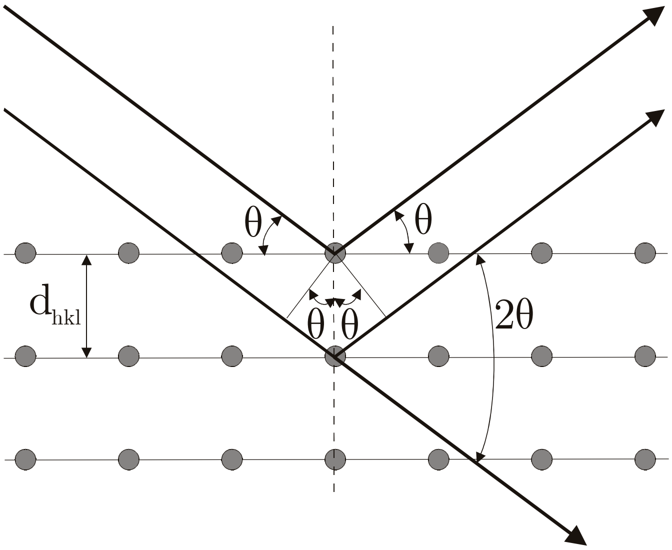

Figure 3.1: X-ray diffraction on crystal lattice.

X-rays occur (see figure 3.1). In this case the intensity is proportional to N^2. Since N is the number of atoms, which is very large, the effect is very pronounced. Thus, the coherently reflected (diffracted) X-rays are easily detected in the background of the incoherently scattered X-rays. The conditions for the positive interference is described by the Bragg diffraction law

$$2d\sin(\theta)=n\lambda \quad , \tag{3.1}$$

where λ is the X-rays wavelength, θ is the incidence angle (equal to the reflection angle), as it is defined in figure 3.1, and d is the distance between the atomic planes.

For a cubic crystalline lattice, as in the case of sesquioxides or YAG, discussed in this thesis, the interplane distance d can be expressed as follows

$$d_{hkl}=\frac{a}{\sqrt{h^2+k^2+l^2}} \quad , \tag{3.2}$$

a is the lattice constant and h,k,l are Miller indices, which are commonly used to denote a certain plane or orientation in the crystalline lattice.

In the course of the work two types of XRD measurements were employed. During the θ-2θ scan (figure 3.2a), as it follows from the term itself, both angles θ and 2θ are scanned synchronously. The crystallites with the defined orientation and various interplane distances are detected. From such a measurement, the informa-

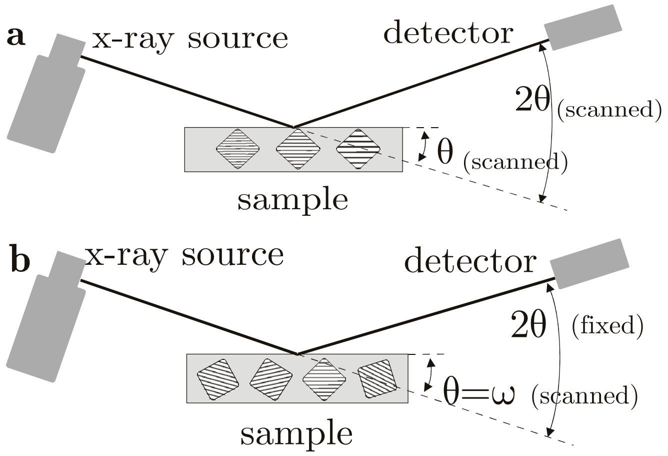

Figure 3.2: (a) θ-2θ scan – domains with different interplane distances detected; (b) ω-scan (rocking curve) – domains with certain interplane distance and different orientations detected.

tion about the crystalline phase of the material, the size and orientation of crystallites (preferred or random), and the lattice constant is gained. For the rocking-curve measurement (ω-scan), the 2θ angle is kept constant and the θ angle (also termed ω in this case) is scanned (figure 3.2b). It is performed to investigate the distribution of crystallites orientations.

Whereas from the position of the diffraction peaks, acquired from the θ-2θ scan, lattice constants can be determined (equations 3.1 and 3.2), the width of the peaks contains information on the dimensions of the coherently scattering domains in the sample, which are roughly equal to the size of the crystallites. The relation between the size of the domains (L) and the peaks width ($\omega_{\text{peak}}=\Delta 2\theta$) is given by Scherrer equation [Cul78]

$$w_{\text{peak}}=\frac{K\lambda}{L\cos(\theta)} \quad , \tag{3.3}$$

λ is the X-ray wavelength and K is a factor depending on the form of crystallites (K=0.9...1). It should be noted, that this equation is not accurate and presents only a rough estimation. Assuming the X-ray source with the Cu-Kα1 radiation ($\lambda_{\text{Cu-K}\alpha 1}$=1.5404 Å) and K=1, the size of crystallite can be estimated using the following simplified equation

$$L^{(\text{nm})}=\frac{8.827}{w_{\text{peak}}^{(\text{deg})}\cos(\theta)} \quad . \tag{3.4}$$

Practically, the intrinsic diffraction peak width (ω_{peak}) is not equal to the measured peak width (ω_{meas}) and is influenced by the finite instrumental resolution of the diffractometer (ω_{inst}). In case the diffraction peaks and instrumental broadening have Gaussian profile, the intrinsic peak width can be determined by

$$w_{\text{peak}}=\sqrt{w_{\text{meas}}^2-w_{\text{inst}}^2} \quad . \tag{3.5}$$

Actually, the diffraction lines have a form close to that described by a Pseudo-Voigt function, which is the mixture of Gaussian and Lorentzian profiles. However, in practice it was found that the line profiles do not deviate substantially from the Gaussian form. Thus, in this approximation equation 3.7 was used to estimate the intrinsic peak.

Experimental

The XRD measurements were performed at Fachhochschule Wedel using the Siemens Kristalloflex 810 diffractometer supplied with a copper X-ray source operating at 40 kV and 20 mA. The emission was not monochromated. Only a Ni-foil filter was used to suppress the Cu-Kβ emission, therefore both Kα1 and Kα2 lines with some residue of the Kβ radiation are present in the emission spectrum ($\lambda_{\text{Cu-K}\alpha1}$=1.5406 Å, $\lambda_{\text{Cu-K}\alpha2}$=1.5444 Å, $\lambda_{\text{Cu-K}\beta}$=1.3922 Å). The radiation spot at the sample was 0.4×8 mm^2. The overview scans (e.g. figures 5.4 and 5.6) were performed with the slit set providing the nominal resolution of 0.15°. The high resolution θ-2θ scans, which were used to determine the width of the diffraction peaks, as well as the rocking-curve measurements were performed using slit sets with the nominal resolution 0.05° or 0.018°.

In figure 3.3 a high resolution scan (0.018° slit) of the <222> reflection for Sc_2O_3 crystal is presented. Since both Cu-Kα1 and Cu-Kα2 emission lines are present in the spectrum of the X-ray source, two peaks are observed in the diffraction pattern. The peak width $w=w_{\text{meas}}$ and the position of the peak maximum $2\theta_0$ were determined by fitting the peak profile $I_{\theta\text{-}2\theta}(2\theta)$ with the function

$$I_{\theta\text{-}2\theta}(2\theta)=c+A\cdot \mathrm{e}^{-4\ln2\left(\frac{2\theta-2\theta_0}{w}\right)^2}+k\cdot A\cdot \mathrm{e}^{-4\ln2\left(\frac{2\theta-2\theta_0-\Delta2\theta_{K\alpha}}{w}\right)^2}, \tag{3.6}$$

where c is the background signal, A is the intensity of the Kα1 reflection, $\Delta2\theta_{K\alpha}$ is the separation of the reflection peaks for Kα1 and Kα2 lines, and k is the intensity ratio for the both reflections. Thus, the reflection peaks were fitted with the double-peak Gaussian function, which, as it can be seen in figure 3.3, describes the peak form quite accurately. The following fitting procedure was used in all cases, when the peak width or position were to be analyzed. The line separation $\Delta2\theta_{K\alpha}$ was calculated using equation 3.1. The parameters c, A, $2\theta_0$, and w were fitted. The peak intensity ratio k was fitted, if the reflection peaks for the Kα1 and Kα2 lines were resolved, and the value determined for the bulk crystal was used, if the peaks were not resolved due to the reflection broadening (e.g. figure 5.5).

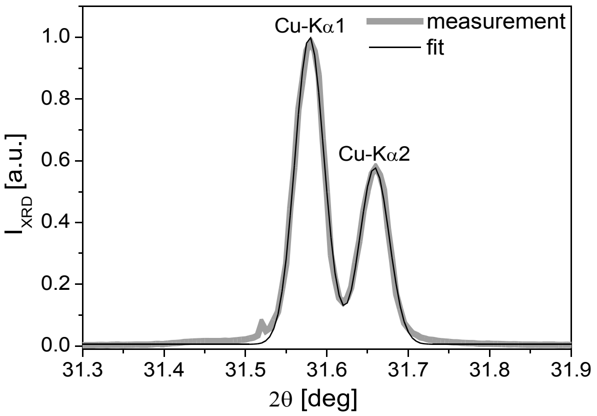

Figure 3.3: High resolution scan of the <222> diffraction peak for the Sc_2O_3 crystal.

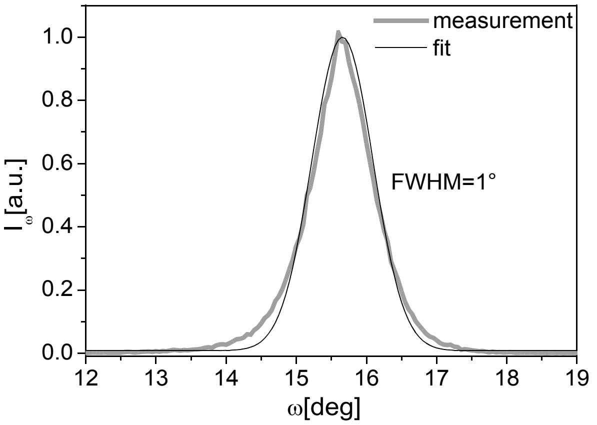

Figure 3.4: Rocking curve of the <222> diffraction peak for the 500 nm Sc_2O_3 PLD-film on α-Al_2O_3 substrate.

The width of the <222> reflection determined for the Sc_2O_3 crystal was 0.040°. This value was used as an instrumental resolution of the diffractometer w_{inst} in equation 3.5, since the crystal itself provides much narrower reflections. For the peaks with the width close to the resolution limit, equation 3.5 would result a high error. Thus, for the peaks narrower than w_{meas}=0.050° only the lower limit for the crystallite dimensions of about 330 nm is given.

A number of measurements of the <222> reflection peaks for the bulk Sc_2O_3, Y_2O_3 and Lu_2O_3 crystals were performed. A mean systematic shift of +0.05° and random deviations of ±0.03° were observed in the peak positions compared to the values calculated from the lattice constants found in the literature (see table 2.2). The measurement data were not corrected, however the peak position was analyzed with respect to the determined offset.

The width of the rocking curve peak w_ω, which describes the distribution of crystallite orientations, have been determined by fitting the measured curve $I_\omega(\theta)$ with the Gaussian profile

$$I_\omega(\theta) = c + A \cdot e^{-4\ln 2\left(\frac{\theta-\theta_0}{w_\omega}\right)^2}, \tag{3.7}$$

where c is the background, A is the peak amplitude, and θ_0 is the position of the peak maximum. The measured rocking curve and the fitting function profile for the 500 nm Sc_2O_3 deposited on the sapphire substrate is presented in figure 3.4 as an example. For the narrow peaks the width about 1° and below the form of the ω-scans deviated slightly from the Gaussian profile, as it can be seen in the figure. For consistency, fitting with equation 3.7 was used also in these cases as well.

§3.2 Ellipsometry and Reflectometry

Both ellipsometry and reflectometry are based on the analysis of light reflected from the sample surface. The measurements are non-destructive and can be performed remotely. Thus, they can be employed in the situations, where application of other techniques might be problematic, as, for example, in a vacuum chamber during the deposition process.

Reflection of Light from Layered Structure

When coherent laser light is reflected from a thin layer of material between two dielectric media (see figure 3.5), infinite number of reflections should be considered with respect to of the interference effects. The field amplitude reflection coefficient $\tilde{r}$ is defined as a ratio of the complex amplitudes, containing both amplitude and phase information, for the electric field of the incident and reflected light

$$\tilde{r}=\frac{\tilde{\mathcal{E}}_{\mathrm{ref}}}{\tilde{\mathcal{E}}_{\mathrm{inc}}} \quad , \quad \tilde{\mathcal{E}}=\mathcal{E}_0 \mathrm{e}^{i\phi} \quad . \tag{3.8}$$

In case presented in figure 3.5 $\tilde{r}$ is given by the infinite series

$$\tilde{r}=r_{0\mathrm{f}}+t_{0\mathrm{f}}r_{\mathrm{fs}}t_{\mathrm{f0}}\mathrm{e}^{-2i\beta}+t_{0\mathrm{f}}r_{\mathrm{fs}}^2 r_{\mathrm{f0}}t_{\mathrm{f0}}\mathrm{e}^{-4i\beta}+\ldots \quad , \tag{3.9}$$

where r_{xx} and t_{xx} are Fresnel reflection and transmission coefficients for the amplitude of electric field at the boundary between two dielectric media. The first index denotes the media on the incident side of the boundary, the second index – media on the other side. Here and further in this section the variables with tilde denote the complex values containing phase information in addition to the amplitude. The expressions for the Fresnel coefficients are polarization dependent and can be found in appendix B. The phase shift β between the light reflected directly from the front surface of the film and the light reflected from the film-substrate boundary is given by

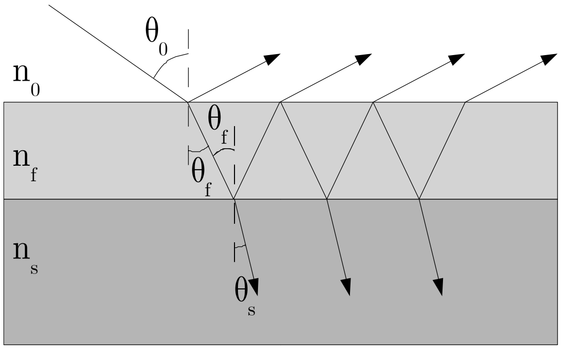

Figure 3.5: Reflection of light from layered structure.

$$\beta = 2\pi \frac{n_f d_f}{\lambda} \cos(\theta_f) \quad , \tag{3.10}$$

where n_f is the refractive index of the film material, d_f is the film thickness, λ is the wavelength of the light, and θ_f is the light incidence angle inside of the film.

Equation 3.9 can be also adapted for the more complicated case, when more than one layer is present. In case a single layer between two half-infinite media (film on substrate) is considered, the infinite series of the multiple reflections presented by equation 3.9 converges into

$$\tilde{r}^{\sigma,\pi} = \frac{r_{0f}^{\sigma,\pi} + r_{fs}^{\sigma,\pi} e^{2i\beta}}{1 + r_{0f}^{\sigma,\pi} r_{fs}^{\sigma,\pi} e^{2i\beta}} \quad . \tag{3.11}$$

σ and π denote two versions of the equation for the σ- and and π-polarizations, respectively.

In the case of reflectometry the intensity of the reflected light is measured. Thus, only the intensity reflection coefficient, which contains no phase information, is determined. Using equation 3.11 the intensity reflection coefficient can be presented as

$$R^{\sigma,\pi} = \left| \tilde{r}^{\sigma,\pi} \right|^2 = \frac{(r_{0f}^{\sigma,\pi})^2 + (r_{fs}^{\sigma,\pi})^2 + 2 r_{0f}^{\sigma,\pi} r_{fs}^{\sigma,\pi} \cos(2\beta)}{1 + (r_{0f}^{\sigma,\pi})^2 (r_{fs}^{\sigma,\pi})^2 + 2 r_{0f}^{\sigma,\pi} r_{fs}^{\sigma,\pi} \cos(2\beta)} \quad . \tag{3.12}$$

The intensity measurements have not very high accuracy and contain little information, therefore single reflection coefficient measurements are almost not used. Typically, the reflection (or transmission) of the sample is measured over a certain wavelength region, so that the measured curve can be fitted with a calculated one. This helps to obtain more precise values for the thickness or refractive index of the film.

Another possibility is to monitor the reflection coefficient continuously during the deposition of the film. In the framework of this thesis the reflectometry was employed to control the thickness of the deposited films in situ. The absolute intensity can be disregarded in this case, since the form of the signal gives enough information to determine the thickness, if the reflective indices are known. The experimental implementation of the method and the data analysis are discussed below in section 4.2.

The ellipsometry is based on the comparison of the polarization states of the light incident to the sample and reflected from it. The polarization state of light is usually named according to the shape, which is imaginary outlined by the end of the electric field vector, when looking in the light propagation direction. Elliptical polarization is the most general polarization state, whereas linear and circular polarizations being special cases. The polarization state is described by ellipticity ε and orientation θ, which define the form of the ellipse (see figure 3.6).

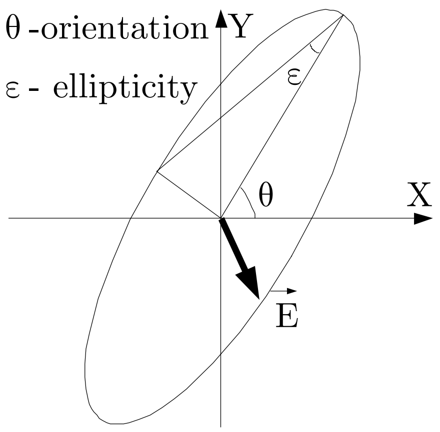

Figure 3.6: Polarization state of light described with ellipticity and orientation.

The ellipsometry considers the ratio of the reflection coefficients for σ- and π-polarization.

$$\rho = \frac{\tilde{r}^{\pi}}{\tilde{r}^{\sigma}} = \tan(\Psi) e^{i\Delta} \tag{3.13}$$

This complex ratio is usually expressed through two real quantities Ψ and Δ, which are determined by solving the matrix equation

$$\begin{pmatrix} 1 \\ X_{det} \end{pmatrix} = \begin{bmatrix} 1 & 0 \\ 1 & \tan(\Psi) e^{i\Delta} \end{bmatrix} \begin{pmatrix} 1 \\ X_{sour} \end{pmatrix} , \tag{3.14}$$

where $X_{det,sour}$ are expressed through experimentally measured $\theta_{det,sour}$ and $\varepsilon_{det,sour}$

$$X_{det,sour} = \frac{\tan(\theta_{det,sour}) + i \tan(\varepsilon_{det,sour})}{1 - i \tan(\theta_{det,sour}) \tan(\varepsilon_{det,sour})} . \tag{3.15}$$

Thus, oppositely to the reflectometry, where the ratio of intensities is determined, the ellipsometry is intrinsically more precise technique, since the experimentally determined angles ε and θ can be measured with higher accuracy than intensity. This makes the ellipsometry a much more sensitive technique. The ellipsometric measurement also maintains the phase value, therefore more information about the sample is gained in such a measurement. The wavelength dependent measurements can be performed to determine the dispersion of the material.

Ellipsometry (Experimental)

The ellipsometric measurements were performed using a commercial ellipsometer EL X-02C (DRE GmbH, Germany), which was designed in the rotating analyzer configuration. Schematically, the ellipsometer is presented in figure 3.7. The left arm contains a He-Ne laser (λ=632.8 nm) used as a light source. Since the laser emission is linearly polarized, no additional polarizer is needed. The laser is aligned to deliver approximately equal light intensities in σ- and π-polarizations with respect to the sample. In the right arm detector and analyzer,

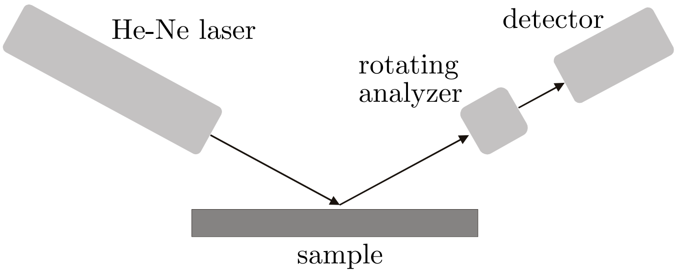

Figure 3.7: Ellipsometer.

rotated with a high-precision step motor (specified accuracy of 0.002°), are located.

Manually adjusting the position of both arms, the measurements can be performed at different light incidence angles. The reference measurement of the light source is performed, when the arms are set horizontally, so that the laser beam directly meets detector. The ellipsometer was controlled by a computer and data was acquired and analyzed with the supplied software.

As mentioned above, ellipsometry is a very sensitive technique. It can be, for example, used to examine silica films on silicon with the thickness in the range of several nanometers. However, generally, the ellipsometric measurements are not quite simple to analyze. The analysis of the ellipsometric data is based on the comparison of the experimentally obtained values with that, derived from the simulation (see scheme in figure 3.8). The measurements might not be interpreted uniquely, in case the model parameters deviate substantially from the real ones. For example, scattering in the investigated sample and substantial deviations of the refractive index hindered the correct analysis in some cases. Thus, the ellipsometry is an appropriate technique for precise investigation of the samples with approximately known thickness, refractive indices and extinction coefficients of the film and the substrate and is not quite suitable, if the parameters are completely unknown.

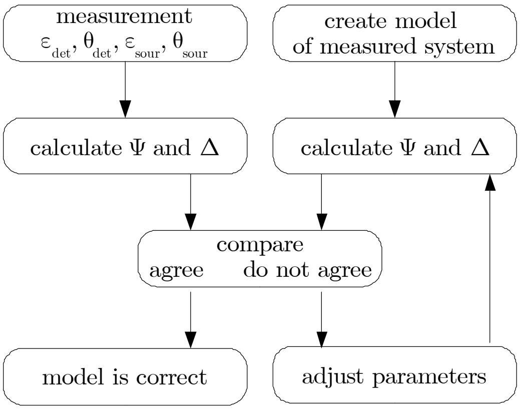

Figure 3.8: Scheme of ellipsometric measurement.

Additionally, some technical problems arose in the course of the experiments. Most of the analyzed films were deposited on both-sides-polished sapphire substrates. Due to the limitations in the supplied software, birefringence of α-Al_2O_3 (n_o=1.768, n_e=1.760 at λ=632.8 nm) and the incoherent reflection from the back side of the substrate could not be included into the simulation. A refractive index matching gel (n=1.780 at λ=589.3 nm) and another sapphire substrate with the dispersive back side was used to suppress the undesired reflection. However, the birefringence and the residual reflection still might influence the accuracy of the measurements. Therefore the results obtained from these measurements were only used to compare the properties of the films. The absolute values of the determined refractive indices should be treated with care.

§3.3 Scattering Measurements

In some cases scattering degree of the sample needs to be investigated. The transmission measurements might be a possibility, however absorption and scattering cannot be separated in this case. In order to examine scattering directly, it is necessary to account for the light scattered in all directions, since the directional distribution of the light intensity can be inhomogeneous. Thus, an integrating sphere (also termed Ulbricht sphere) is employed in this case. The idea of such measurement is to place the sample inside of a sphere with diffuse reflecting inner surface, so that the light intensity is homogenized through the multiple reflections. Hence a local intensity measurement at a single position can be scaled to determine the integral intensity over the whole surface.

The set-up used in the course of this work in order to compare the scattering behavior of the PLD-films is presented in figure 3.9. The

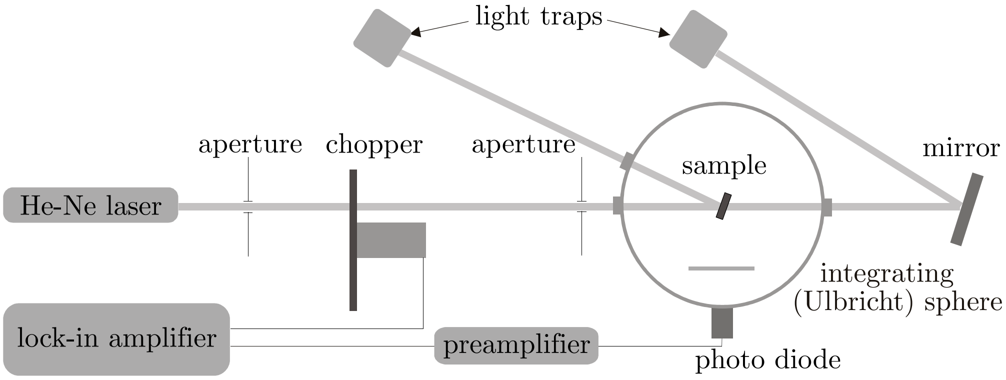

Figure 3.9: Experimental set-up used for the scattering measurements using integrating (Ulbricht) sphere.

samples were placed in the middle of the sphere with the diameter of 15 cm, which inner surface was covered with the $BaSO_4$ based paint reflecting about 98% of light at the wavelength of the He-Ne laser (632.8 nm) used as the light source. An entrance opening with the diameter of 6 mm, as well as two 8 mm windows for the transmitted and reflected light were provided. A Si-detector with the area of 7 mm^2 is build-in into the sphere wall. A barrier in front of the detector blocked the light coming directly from the sample, thus only the averaged light intensity was detected. Since the lock-in detection technique have been used, the environment light did not influence the measurements noticeably. However, the light traps were required for the reflected and transmitted laser beams, so that the light was not scattered back into the sphere. Also two apertures were placed along the beam path to block the fluorescence emission and scattered light coming out of the He-Ne laser.

It have been found, that the measurements are strongly influenced by dust and pollution on sample surface. Thus, the experiments using the integrating sphere were performed before all other investigations. The samples were thoroughly cleaned with pressed air. Up to ten measurements have been performed for each sample at different positions, then strongly deviating values were discarded and a mean value was calculated.

§3.4 Spectroscopic Measurements

Infrared Spectroscopy

The excitation and emission spectra in the infrared region have been measured for the Nd^{3+} and Yb^{3+}-doped PLD-films. The excitation spectra were used to determine favorable wavelength for pumping. Typically, the absorption spectroscopy is performed for this purpose, since it allows the quantitative analysis. However, due to the film thickness in the range of several micrometers, the absorption was too low to measure by conventional methods. The emission cross-sections of the dopant, which is an important parameter to estimate lasing potential of the medium, were determined from the emission spectra. Also inferences about disorder of

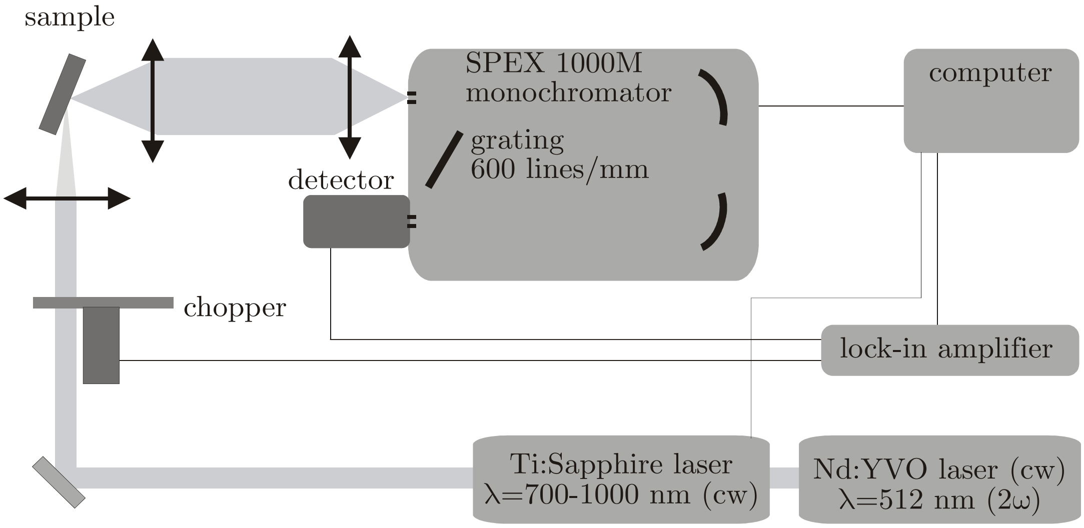

Figure 3.10: Scheme of experimental set-up for the spectroscopic measurements in near- infrared region.

the crystalline structure of the PLD-film can be made from the inhomogeneous broadening of the dopant spectra.

The measurements have been performed using the set-up presented in figure 3.10. The continuous emission of the Ti:Sapphire laser was used for excitation. Two sets of resonator mirrors allowed operation either in 700 nm – 850 nm or in 850 nm – 1000 nm ranges. The emission has been detected by a InGaAs photo diode. The measurements have been performed at room temperature. The excitation spectra were corrected for the wavelength dependency of the output of Ti:Sapphire laser. Using the emission spectrum of a tungstate lamp at the temperature of 2600 K and the calculated intensity distribution of the black-body (Planck's law), the spectral response function of the set-up was calculated to calibrate the emission spectra.

The emission cross-section spectra $\sigma_{\mathrm{em}}(\lambda)$ for the transition between two multiplets i and j of the RE-ion were calculated from measured emission spectra $I(\lambda)$ using the Füchtbauer-Ladenburg equation [Aul82, Pay92]

$$\sigma_{\mathrm{em}}(\lambda)=\frac{\beta_{i\rightarrow j}\,\lambda^5 I(\lambda)}{8\pi n^2 c\tau_{\mathrm{rad}}\int\lambda\cdot I(\lambda)\,d\lambda}\quad . \tag{3.16}$$

τ_{rad} is the radiative lifetime of the excited state i of the dopant, n is the refractive index of the medium, c is the speed of light in free space, and $\beta_{i\to j}$ is the normalized probability of the radiative transition from the excited state i into the lower state j, termed as a branching ratio coefficient.

Spectroscopy in Visible Region (Fluorolog)

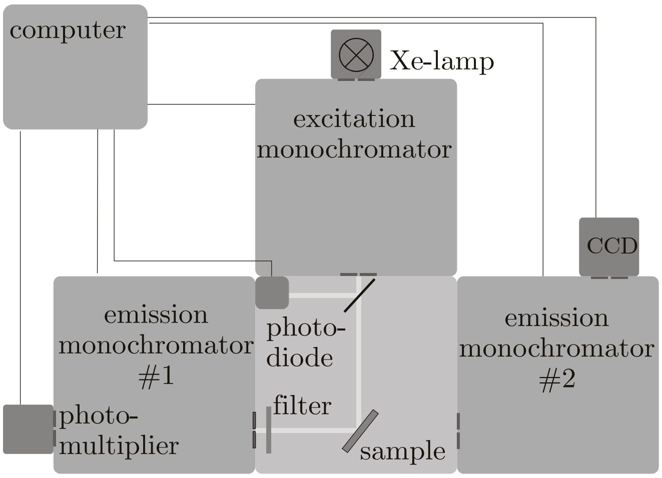

Figure 3.11: Scheme of Fluorolog spectrometer set-up.

The emission and excitation spectra for the Eu-doped PLD-films were measured using the modular spectrometer FL321 Fluorolog-3 (Jobin Yvon). The monochromated light of the high-pressure Xenon lamp was used for excitation. The emission was detected by the R928 (Hamamatsu) photomultiplier, cooled down to -15°C to reduce electronic noise. The emission spectra were corrected with the known spectral response of the emission channel. The intensity of the excitation light, measured by a reference photo diode with known sensitivity, was used for correction of excitation measurements. The set-up was fully computer controlled. The second emission channel with the CCD detector was not employed in the framework of this thesis.

Time Resolved Emission Measurements

The time resolved emission measurements were used to determine the lifetimes of the excited states of Nd^{3+} and Yb^{3+}-dopants. This data was used to evaluate the quality of the crystalline lattice of PLD-film, since lattice defects and local symmetry distortion can substantially reduce the lifetimes. The excited state lifetimes are also an important parameters to estimate the possibility of laser operation in the medium.

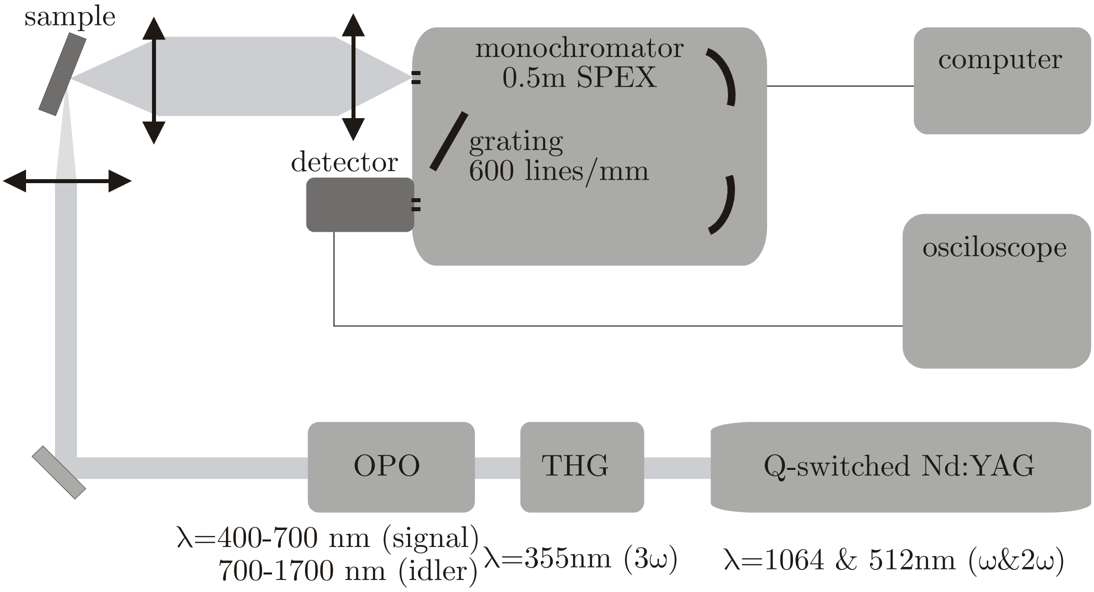

Figure 3.12: Scheme of experimental set-up for the fluorescence lifetime measurements.

The fluorescence decay curves were recorded at room temperature using the set-up presented in figure 3.12. The pulsed radiation (~20 ns, 10 Hz) of an optical parametric oscillator (OPO) pumped by the third harmonic (λ=355 nm) of a Nd:YAG laser was used for excitation. The wavelength of the OPO emission can be tuned in the broad region (400 nm – 1700 nm). The emission of the dopant was spectrally separated from the OPO radiation by the 0.5 m SPEX monochromator and detected with the S1-photomultiplier. The signal was recorded recorded using the LeCroy 9360 oscilloscope. It was averaged up to 5000 times to improve the signal-to-noise ratio.

In case only linear deexcitation process are present and the fluorescence decay is exponential, the lifetime of the upper excited state of the dopant τ is given by

$$\frac{1}{\tau}=\frac{1}{W_{\mathrm{rad}}+W_{\mathrm{nonrad}}}\ ,\quad W_{\mathrm{rad}}=\frac{1}{\tau_{\mathrm{rad}}} \qquad (3.17)$$

where τ_{rad} is the radiative lifetime and W_{rad}, W_{nonrad} are radiative and nonradiative decay rates, respectively. If the radiative lifetime of the excited state is known, the quantum efficiency of the emission η_q can be estimated

$$\eta_q = \frac{W_{rad}}{W_{rad} + W_{nonrad}} = \frac{\tau}{\tau_{rad}} \quad . \tag{3.18}$$

The quantum efficiency of the active material influences the performance of laser operation and amount of the produced heat. Thus, high quantum efficiency is desired, especially for the material used as an active medium in the high power lasers.

SuperLumi Experimental Set-up

Some emission measurements were performed at the SUPERLUMI station (DESY, Hamburg, Germany), which is mainly designed for the spectroscopic investigations in the UV region. The excitation source is synchrotron radiation from the positron storage ring DORIS, which spectrally is filtered by the primary monochromator. The radiation in the range 60 nm – 330 nm with the resolution of 0.3 nm is available for experiments. Since the radiation in the wavelength region below 200 nm is strongly absorbed by any material (including air), no window could be placed to separate the set-up from the synchrotron ring. Thus the sample chamber, the primary monochromator, and the light channels are constantly maintained under ultra-high vacuum conditions. The samples were placed on a copper bar, which could be cooled with liquid helium down to 10 K. The emission was analyzed using a secondary monochromator and a cooled (-114°C) CCD-camera. A more detailed description of the set-up can be found in [Neg03, Möl86]. Combination of intense radiation source, sensitive detector, and possibility to work at low temperatures allowed to detected emission for the Yb_2O_3 PLD-films, which could not been observed using other set-ups.

Chapter 4. Film Preparation by Pulsed Laser Deposition

First section of this chapter gives an overview on different deposition techniques, that can be used to produce doped and undoped oxide films for optical applications. Also waveguide fabrication techniques not based on deposition methods are mentioned. Practical aspect of pulsed laser deposition and film preparation is discussed in more detail in the second part of the chapter. Analysis of scandia film properties and optimal deposition parameter is presented in the last section.

§4.1 Deposition Techniques

4.1.1 Overview

Film fabrication methods can be classified into several categories depending on the phase of material, which is deposited on substrate. Also a separate group of waveguide fabrication methods, based on modification of substrate material, can be distinguished:

- ◇ solid
  - direct or thermal bonding
- ◇ liquid
  - liquid phase epitaxy (LPE)
  - sol-gel process
- ◇ gas or plasma
  - chemical vapor deposition (CVD)
  - molecular beam epitaxy (MBE)

  - pulsed laser deposition (PLD)
  - sputtering
  - thermal evaporation (resistive heating, EBV, IAD)
- ◇ modification of material
  - indiffusion
  - ion exchange
  - ion implantation
  - direct laser writing

Below short descriptions of the techniques are given.

Bonding

Bonding in based on the attraction due to Van der Waals forces, which appear, if two very smooth surfaces are attaches together closely (hundreds of nanometers). Both substrate and active material are usually polished with epitaxial quality and attached together. Sometimes additional pressure or heating is applied to enhance bonding strength. After that the structure is quite stable, so that the active layer can be polished down to the necessary thickness or finishing of the end faces can be done. If necessary a cladding layer can be attached on top.

Due to the fact that bulk material is used and all surfaces perfectly polished, bonding seems to be a suitable technique to produce high quality and low loss waveguides. High-power laser operation have been demonstrated in a bonded waveguide structure [Mac01]. However, the technique is time consuming and it might be complicated to produce waveguides thiner than some tens of micrometers.

Liquid Phase Epitaxy (LPE)

To produce a LPE-film a suitable substrate is immersed in a oversaturated melt or solution of material, it precipitates onto the substrate and a film is formed. The solution in low temperature melting substances (flux) is often used to reduce the process temperature. LPE is quite simple and scalable technique, since multiple substrates can be used simultaneously. It was widely used for growth of semiconductor materials, but also active oxide materials for laser applications can be grown. For example Nd:YAG waveguide laser grown by LPE was demonstrated [Cha92], also Yb:YAG LPE-films have been used as active medium for a thin disk laser [Ubi04]. The method provides quite low degree of film thickness control, therefore fabrication of thin films can be complicated. Another disadvantage of the technique is the necessity to find a suitable flux material. In some cases contamination of the film with flux material and cracking of grown films can occur.

Sol-Gel Process

Sol is a colloidal suspension of solid particles in liquid, which is produced by hydrolysis of metalorganic compounds (precursors) and subsequent water condensation. This particles with the size from some nanometers to a few hundreds nanometers are precipitated from solution onto a substrate either by dipping it into suspension or by spinning. At this stage colloidal particles condensed on the substrate form *gel*. After drying at room temperature or with some heating a xerogel film is formed. Afterwards, annealing at higher temperatures can be used to improve density and crystallinity of the film, so that ceramic- or glass-like film is produced. The advantage of the process is its simplicity, since no special equipments is required and the whole process can be carried out at relatively low temperatures ($<$100°C). Thus, temperature sensitive compounds can be incorporated into the film. However, in order to produce high quality films, proper precursors and process parameter need to be found, which is not always trivial. Also stress and cracking of films can be a issue.

Chemical Vapor Deposition (CVD)

In case of chemical vapor deposition source material for the film fabrication is a gaseous compound (precursor), containing the ions intended for the film formation. Decomposition of the molecules is catalyzed at the surface of the heated substrate. Rests of the compound are desorbed from the substrate and removed. Thus, in order to deposit films of certain material, first a suitable precursor is to be found.

Contamination of the chamber and usage of reactive materials as precursors might result some difficulties for use of this technique in an experimental environment.

Molecular Beam Epitaxy (MBE)

The idea of MBE is to deposit every single substance of the multi component film separately. Every component is placed into an effusion cell, which is isothermally heated to evaporate the material. Through an aperture in the cell wall evaporated substance is expanding towards a substrate forming a molecular beam. Intensity of each beam and thus deposition of individual components can be controlled very precisely. Uultra high vacuum (~10^{-10} mbar) is a necessary condition for the MBE process. High substrate temperatures are also required to produce high quality films, due to the thermal character of the deposition process.

Very high quality, epitaxial films can be produced by MBE. However, due to vacuum requirements, this technique is quite expensive and inflexible. Thus, MBE is typically employed to fabricate semiconductor films, where film quality is a critical factor. MBE scandia films have been reported recently [Kle05].

Thermal Evaporation

A resistive heating or electron beam evaporation (EBV) can be used to melt and evaporate source material, which is then deposited on substrates. Since typical particles energy is less 1 eV, typically amorphous, not quite dense films are produced. Substrates are usually heated, in order to improve the density of the films. An ion beam assistance can also be employed. In this case the technique is typically referred to as ion-assisted deposition (IAD). The thermal evaporation techniques are often used to fabricate optical coatings. However, this methods are not suitable for deposition of high quality crystalline films. Also deposition of complex materials is an issue, since different vapor pressures of the components can result in different deposition rates, thus the stoichiometry is often not preserved.

Sputtering

Sputtering effect can be achieved by acceleration of inert gas ions, which bombard the target and mechanically eject the material. DC acceleration (in kV range) is used to sputter conductive material. In order to avoid charging effects, RF sputtering is utilized for deposition of insulators. Sputtering is distinguished by high deposition rates and broad angular distribution of the plume, which allows large area depositions. Along with the thermal evaporation, this method is often used to fabricate optical coatings. Crystalline film growth can be achieved, if substrate is heated. Additional voltage can be applied to accelerate the particles in the plume, which typically have energies in the range 0.1-1 eV. A disadvantage of the technique for experimental applications is a large amount of material, which is necessary for the target.

Indiffusion and Ion Exchange

Indiffusion is a waveguide fabrication technique based on increase of refractive index of material, when appropriate ions are incorporated into it. First material, that is to be incorporated, is deposited onto the substrate, which is then placed into oven at high temperature (>1000°C) for some period of time for diffusion to occur. Ion exchange method is based on similar principle. The substrate is placed in the bath of appropriate molten material, so that the ions from the substrate and from the melt exchange slowly.

Thus, a layer of modified material is produced. In case of correct material choice, the layer will have higher refractive index and can be used as a waveguide. Masking can be employed in both methods to produce channels or other structures. Since crystalline material is taken as a source, high quality of layers can be expected. For example Ti:sapphire waveguide laser have been realized by indiffusion [Hic98]. However long processing times, which can be up to several days long, and incapability to produce sharp, well defined structures are major disadvantages of both techniques.

Ion Implantation and Direct Laser Writing

Modification of material can be achieved by bombarding it with high energy ions in the range of MeV. At high energies ions do not affect the crystalline lattice, and material is destroyed only when they are decelerated. Thus, the effect can be produced in the underlying material and buried structures can be fabricated. Material can also be modified by depositing energy into it by laser light. High intensity femtosecond laser pulses are often utilized for this purpose. Due to nonlinear absorption, this allows processing of transparent materials. Using appropriate focusing it is achieved, that damage occurs only in focal area itself not affecting surrounding material. Thus, volume processing is possible.

Both techniques allow fabrication of complex structures by masking or by scanning of focused beam. Disadvantages might be relatively small induced refractive index change and undesired effects, which are introduced due to the damage of material. Ion implantation and laser writing can also be combined with deposition methods. This would result a very flexible method, since it should be possible to combine multiple materials or layers and to produce more complicated structures.

4.1.2 Pulsed Laser Deposition Technique

The history of pulsed laser deposition (PLD) started, when Smith and Turner [Smi65] demonstrated films deposited from materials ablated using a ruby laser. Various semiconductor, oxide and chalcogenide films with varying quality have been produced. However, strong attention to the pulsed laser deposition has been attracted only when it has been demonstrated, that this technique is suitable for deposition of complex compounds like $YBa_2Cu_3O_7$ (YBCO), which was considered a promising high temperature superconductor [Dij87].

The principle of PLD is quite simple. When beam of a pulsed laser is focused onto some material. Due to the deposited energy it is evaporated, expands from the target surface and is deposited on a substrate placed on the opposite. Ablation is carried out under vacuum conditions or reduced ambient atmosphere, since the ablated material can not reach the substrate under atmospheric pressure.

In spite of the simplicity of the general idea and its realization, processes occurring during ablation and deposition are quite complex. Up to now some of them are not fully understood and most are difficult to described analytically. Thus, most of research in this area is empirical.

The deposition process can be separated into several stages: ablation, plasma plume expansion, deposition onto a substrate, nucleation and formation of the film structure. The ablation process depends strongly on the properties of the target material and surface quality as well as on characteristic of laser radiation. The laser radiation is absorbed by electronic subsystem and then the energy is transferred to the lattice. In case of oxides (insulators) free electrons first need to be produced. It occurs as a result of one or several mechanisms: linear absorption, multiphoton absorption, impact avalanche ionization. Depending on the time scale, either the dissociation of material can take place, when a certain free electron density is exceeded (laser-induced breakdown), or energy is transferred from electrons to lattice, so that thermal melting and evaporation occur. The former scheme take place, when pulse duration is less then time constant of energy transfer from electrons to the lattice ($\tau<\tau_{\text{e-ph}}$). $\tau_{\text{e-ph}}$ is typically in picosecond range, thus it is true for femtosecond and picosecond pulses. The latter case occurs for longer pulses ($\tau>\tau_{\text{e-ph}}$), including the nanosecond radiation used in this work.

Thus, gaseous or, more often, partly ionized material (plasma) is formed and expands from the target. The evaporation is very fast, plasma is not thermalized and expansion has ultrasonic character This plasma can also absorb some part of laser radiation and thus further influence course of the ablation process. Plume is usually very strong directed, which might result difficulties for large area coatings. Individual species in the plasma plume has energies up to 100 eV. This feature of PLD is often utilized to produce crystalline films even at relatively low substrate temperatures. Ambient gas plays a crucial role in the plume expansion process. It can be used to reduce the velocities of plasma species and partly thermalize the plume. Reactive atmosphere is often used to prevent the deficiency of some volatile component, e.g. oxygen.

In the case of nanosecond pulses, not completely evaporated, liquid droplets can be desorbed from the target. Loosely attached solid particles can also be dislodged due to stress produced by ablation. This droplets or macro particles deposited on substrate (termed particulates) are one of the major issues of PLD technique, since they degrade the quality of fabricated films.

A number of processes take place, when plume species reach substrate surface. Depending on their energy, they are adsorbed at the surface or are implanted into the volume of material. Subsequently diffusion and recrystallization processes take place which are usually stimulated by heating of the substrate. When particle energies is too high, they can result destruction of the already formed film and even desorption of film material. Depending on process parameters and interaction between substrate and arriving plume species, film formation can occur in different regimes. Typically three such regimes are distinguished: (1) layer-by-layer growth, when previous layer is completed before the growth of the next one starts; (2) island growth, first three-dimensional islands are formed, and only afterwards they grow together to form a closed film; (3) mixed mode, first some monolayers are formed and then island growth start to prevail. Generally, due to the high kinetic energy, particles on the surface have enough mobility. Therefore growth of crystalline films is relatively easy to achieve for PLD process.

Essential characteristics of pulsed laser deposition can be summarized as follows:

- ◇ advantages
  - flexibility in choice of material, background atmosphere, etc., due to the fact that energy source (laser) is located outside of the deposition chamber
  - high energy of plume particles and high degree of ionization stimulate crystalline film growth

  - nonthermal character of plume formation, thus stoichiometry of material is usually preserved and even materials non-existent under thermal equilibrium conditions can be produced

- ◇ disadvantages
  - large area, uniform coatings are problematic, due to strongly directed plasma plume
  - high particulates density in the deposited film

More information on pulsed laser deposition can be found in following books [Bäu00, Chr94] as well as in review articles by Saenger [Sae93a, Sae93b].

Experimental set-up used in the course of this work is described below in the next section. Influence of PLD-process parameters on the films characteristics for the particular case of Sc_2O_3 is experimentally investigated in section 4.3.

§4.2 Preparation of PLD-Films

Experimental Set-up (PLD-Machine)

The films prepared in the course of this work have been deposited using PLD-machine, which is located in Institut für Laser-Physik, Universität Hamburg and was built by PINK GmbH Vakuumtechnik. Schematically, the machine is presented in figure 4.1. It consists of two joined vacuum chambers, which can be isolated by the vacuum valve. The bigger chamber is utilized as a main chamber for deposition process. The smaller one is used as an air-lock to transfer substrates and targets into the machine and to unload deposited films without flooding the main chamber with air. This make the transfer process faster and the main chamber is always maintained under ultra-high vacuum conditions, which contributes to its purity. With the installed turbo-molecular pump the base pressure in the deposition chamber up to 10^{-7} mbar can be achieved. The substrates and targets are mounted in unified metal frames. From the air-lock chamber they are first transported into a magazine in a main chamber, which is capable to hold eight such frames. Inside of the

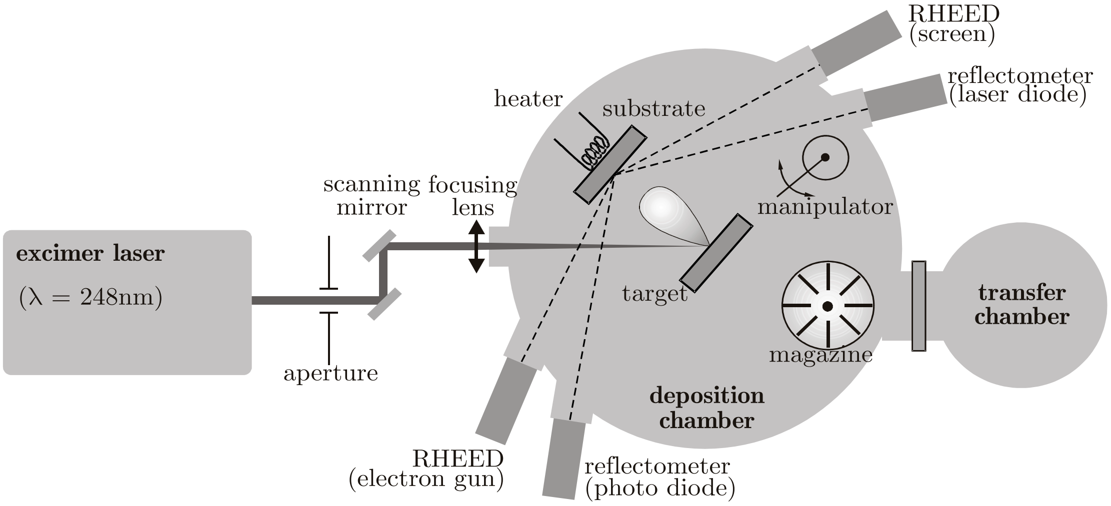

Figure 4.1: Pulsed laser deposition machine.

deposition chamber these frames can be transferred either to a substrate holder or to a target holder by a manipulator arm. Behind the substrate holder a resistive heater (SiN-ceramic) is located. The temperature of the substrate is controlled by a one-color pyrometer and can reach up to 700-750°C. It is essentially lower than the heater temperature itself (up to 1000°C), since no direct thermal contact is present. After the deposition the cooling down rate was kept at 20°C/min.

The gas pressure in the chamber was controlled by a full-range gauge and, additionally, by a baratron (capacitance pressure detector), which was designed for more precise measurement in the range of 10^{-4}-1 mbar. However nonlinear behavior in the range $<10^{-2}$ mbar was discovered for the baratron in the course of experiments. Thus, only the full-range detector have been employed later. The background gas is let in through the gas flow controller and the necessary pressure is achieved dynamically by balancing the gas inflow and pumping strength. The complete vacuum chamber with all detectors, pumps, motors and controller is computer controlled.

An excimer laser (Lambda Physik LPX 305) was utilized for ablation. The laser was operating with KrF mixture and delivered up to 1.2 J per pulse of 248 nm radiation with up to 50 Hz repetition rate. The pulse length was about 25 ns. In order to obtain a roughly homogeneous energy distribution in the laser spot on the target, an aperture was used to cut off the edges of the laser beam, where the intensity is varying strongly. Only the central part of the beam was utilized for ablation. The laser beam was scanned over the target surface. This prevented formation of craters on the target surface and also ensured the homogeneous film thickness over the whole substrate surface, since plasma plume is strongly directed. The beam was focused onto the target with a lens (f=400 mm) placed in front of the window of the vacuum chamber. Both lens and the window were anti-reflection coated for 248 nm.

First a piezoelectric scanner have been utilized to tilt the mirror, which was used to scan the laser beam. However, this scanner was designed for high scanning frequencies and was not able of holding heavy mirrors. Only small, 10 mm in diameter mirror could be mounted on this scanner. This resulted a very small aperture for the excimer laser beam, which had approximately 15×30 mm cross-section. Therefore a ×2.5 telescope was used to reduce the beam size. Nevertheless only ~7% of laser energy could be transmitted into the chamber. Bad quality of the excimer laser beam and aberrations, due to the telescope lens, resulted in an asymmetrical, dash-like spot on the target. The focusing was kept constant and the laser fluence was varied by tuning the energy emitted by the excimer laser.

Later the piezoelectric beam scanner was replaced by a deflection unit with two galvanometer scanners. They could bear larger mirrors resulting in an aperture of 20 mm in diameter. The telescope was not used in this case, consequently the laser spot on the target had rectangular form (determined by the aperture) and its size could be varied by changing the focusing lens position.

The thickness of the growing film was controlled during deposition process by a reflectometer. It is discussed below in more detail. Also a RHEED[1] equipment was installed on the PLD-machine, including a detecting screen and an electron gun with a double differential pumping stage for operating at high chamber pressures. However, this facility was not utilized in the framework of this thesis.

---

[1] RHEED – Reflection High Energy Electron Diffraction.

Substrates and Targets Preparation

Sapphire, quartz, and YAG substrates used in the course of the work were supplied by CrysTec GmbH (Berlin, Germany). All the substrates were either both-side or single-side polished with epitaxial quality. Sapphire (α-Al_2O_3) and quartz (α-SiO_2) substrates were (0001)-oriented, since they provide good lattice matching with sesquioxides, as discussed below in section 4.3.2. YAG substrates were (100)-oriented. Yttria, lutetia, and scandia substrates are not available commercially. Thus, bulk crystals of scandia, yttria, and lutetia have been grown by a heat-exchanger method (HEM), which is described in section 2.1.1. Subsequently, the crystals were oriented using a Laue method, cut, and commercially polished with epitaxial quality at Crystec GmbH. The substrates were cleaned with pressed air, before they were loaded into the machine.

Ceramic pellets, which served as targets for ablation, were prepared as follows. The source materials in the form of powders were mixed together in the necessary proportion. Afterwards, powder was pressed with a pressure up to 600 bar using a hydraulic press and sintered in air at 1650°C for 24 hours. When a target was utilized for ablation for the first time, it was "cleaned" in the chamber with up to 5000 excimer laser pulses under the same conditions, as the subsequent deposition. A dummy was put into the substrate holder, so that the heater was not contaminated.

Film Thickness Control (Reflectometry)

The thickness of deposited films was controlled in situ by a reflectometer, which consists of a laser diode and photo diode (see figure 4.1). The intensity of the laser beam reflected from the sample in the chamber is measured with the photo diode, amplified with a DC-amplifier and recorded with a computer during the whole deposition process. A special software was designed to record the reflectometer signal and to analyze it instantly. Thus, real-time control of the film thickness was possible. The signal was fitted using a genetic algorithm[1] with a model, which is

---

[1] The idea of *genetic algorithm* lies in taking one or more sets of initial parameters, mixing and varying this sets randomly. Thus, a large number of such

discussed below. The excimer laser was controlled with the same software, therefore the deposition process could be set up to stop automatically at the necessary thickness.

During the growth process the film thickness is changing. Subsequently, changes the phase shift between the light reflected from the front film surface and the light reflected from the film-substrate. This causes the variation of intensity of the detected signal, resulting from the interference of the both reflected beams. Actually, one have to deal with infinite number of reflections and in detail this was discussed in section 3.2. If the film is not absorbing or scattering, the reflectometer signal is expected to have a form of periodical function of the film thickness (d_{film}) described by equation 3.12. Simplified it can be presented as

$$R = f\left(\cos\left(2\pi \frac{d_{\text{film}}}{P_{\text{thickness}}}\right)\right);\ P_{\text{thickness}} = \frac{\lambda}{2 n_{\text{film}} \cos(\theta_{\text{film}})}\ , \tag{4.1}$$

where $P_{\text{thickness}}$(nm) is the period of the function, which can be calculated. The laser wavelength light (λ), incidence angle (θ_{film}) and refractive index (n_{film}) of the film should be known.

Experimentally, the reflectometer signal was recorded as the function of the number of pulses of the excimer laser – $I(N_{\text{pulses}})$. The following equation was used to fit the measured signal

$$I = C + A \cdot R\left(\cos\left(2\pi \frac{Z_{\text{rate}} \cdot N_{\text{pulses}}}{P_{\text{thickness}}}\right)\right) \tag{4.2}$$

where R is the reflectometer signal as described by equation 3.12 (r_{xy} parameters are calculated), C is a constant shift, which can result from

---

parameter sets is generated. Afterwards “selection” takes place. A certain number of sets that give better results, in our case smaller deviation from the measured reflectometer curve, are kept and than serve as a seed for the next “generation” of parameter sets. This process continues cyclically, until some quality condition, which can be given as a maximum allowed deviation value, is not satisfied. In our case, since the dataset of the measured values was updated constantly, the fitting algorithm was running during the whole deposition process.

the amplifier or an incoherent reflection from the back side of the substrate, A is scaling factor (amplitude), Z_{rate} is the deposition rate in nm/pulse. Fitting the measured signal with equation 4.2, the deposition rate (Z_{rate}) and, consequently, the film thickness ($d_{\mathrm{film}}=Z_{\mathrm{rate}}\cdot N_{\mathrm{pulses}}$) are determined.

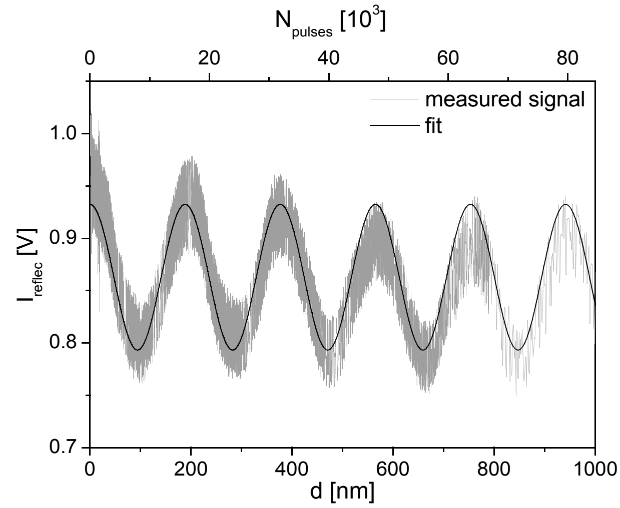

Figure 4.2: Reflectometer signal recorded in situ during deposition of a 1 µm thick Sc_2O_3 film.

An example of recorded reflectometer signal and the fitted curve is presented in figure 4.2. The quite large fluctuations of the measured signal intensity were caused, by the heater controller. It was operating in an active-idle modus with the period of a couple of seconds. Thus, the heater power was oscillating as well as the temperature, resulting in slight mechanical deformations of the holder. This deformations caused intensity fluctuations, since the reflected beam slightly moved off the photo diode, which had the area of only a couple of square millimeters. At the thickness of approximately 800 nm signal acquisition rate was reduced, causing the measured signal to look more sparsely.

§4.3 Optimization of PLD Process Parameters

Pulsed laser deposition is a quite complex process with many parameters, that can be varied. One the one hand this provides flexibility, so that the process can be adapted for deposition of a large number of materials, on the other hand this parameters need be optimized for every material in order to achieve the required quality of deposited films. Only few reports on systematic investigations of influence of PLD process parameters on the properties of oxide films can be found, most concerning Eu:Y_2O_3 (e.g.

[Lan04]). The research into the PLD fabrication of Y_2O_3 films is also presented in the theses of Burmester [Bur02] and Bär [Bär04]. The deposition of gadolinium-gallium garnet (GGG) and Ti:sapphire films has been investigated in the theses of Barrington [Bar01] and Anderson [And98].

Rare-earth scandia is an interesting active material due to its favorable spectroscopic properties, which are discussed more detailed in chapters 6 and 7. Up to now, no reports on PLD fabricated Sc_2O_3 films can be found. Hence, a systematic analysis of the influence of PLD process parameters on the properties of Sc_2O_3 films was performed in order to determine optimal conditions for the film fabrication.

4.3.1 Laser and Target

Laser

The properties of the laser radiation used for ablation influence substantially the character of ablation process. Usually, it is desired, that the absorption of laser pulse occurs in the smallest possible volume. This ensures, that all the removed material is completely evaporated, so that as little particulates as possible are formed. Thus, the typical requirements are short wavelength radiation, ideally below the fundamental absorption edge, where the linear absorption is high. Another possibility is to use intense ultrashort pulses in the femtosecond range, where nonlinear absorption plays the major role. Theoretical and experimental considerations of different ablation regimes, depending on wavelength and pulses duration of the laser, can be for example found in review by A. Vogel *et. al* [Vog05].

In our case a KrF excimer laser was used, therefore the laser wavelength and the pulse duration were fixed (λ=248 nm, τ=20 ns) and no experiments could be carried out to investigate their influence on the films characteristics. However, this kind of laser is typically used for such applications and a number of reports on successful fabrication of oxide materials with excimer lasers can be found in the literature.

Target Surface

The quality of the target influences the ablation process as well. In the course of this work ceramic targets have been utilized. Such targets are much easier to fabricate compared to crystalline ones, since scandia crystals are not available commercially. However, as it will be discussed below in section 6.3.4, they can be one the reason for the high scattering losses in waveguiding PLD-films. This is due to the fact, that loosely attached fragments of the target can be dislodged from it without being fully evaporated. The use of crystalline, high density targets should reduce the amount of particulates.

Laser Fluence

An important parameter is the energy deposited into the target per unit area. This quantity is usually termed laser fluence. If it is below a certain value, no material is removed. Ablation occurs only if a threshold value, specific for every material, is exceeded. The deposition process is usually carried out at fluences somewhat higher than the threshold value to ensure congruent evaporation.

When the older set-up with the small aperture scanning mirror (piezoelectric scanner) was utilized, the excimer laser beam was focused into the area of about 1.5 mm^2 (see figure 4.3). One can note the irregular spot size, due to aberrations on the telescope lenses. Typically, laser was operating at 700 mJ per pulse, 49 mJ (7%) was transmitted through the optics into the deposition chamber. This resulted in the fluence of 3.3 J·cm^{-2}. When the newer set-up with larger aperture (galvanometer-scanner) was used, about 20% of the laser energy was transmitted into the chamber. The area of the ablation spots on a Sc_2O_3 ceramic for different positions of the focusing lens and fluence was determined for different laser energies and spot areas. In

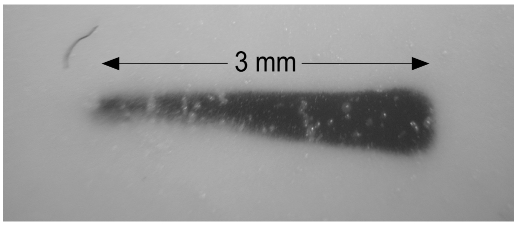

Figure 4.3: Ablation spot on the Y_2O_3 target resulting from 10 laser pulses (3.3 J·cm^{-2}). Older PLD set-up (small aperture piezoelectric beam scanner with telescope) is used.

figure 4.4 three of such ablation spots are presented as an example: (a) laser beam was focused two strongly (3.7 J·cm^{-2}), so that satellite spots resulting from higher transversal modes of excimer laser beam are seen; (b) a rectangular spot with clearly defined borders is observed (2.6 J·cm^{-2}); (c) spot was too large and fluence too low (0.7 J·cm^{-2}), so that ablation took place only in the middle, upper and lower regions of the spot were only slightly darkened.

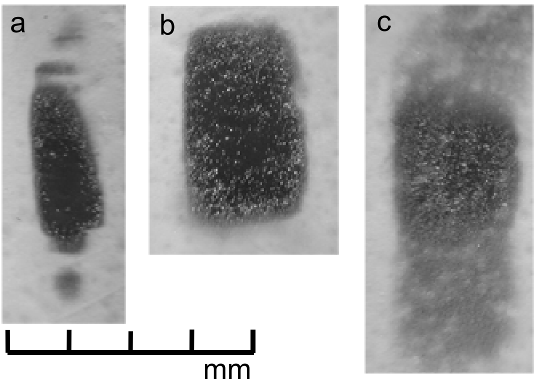

Figure 4.4: Ablation spots on the Sc_2O_3 target resulting from 50 laser pulses at different fluences: (a) 3.7 J·cm^{-2}; (b) 2.6 J·cm^{-2}; (c) 0.7 J·cm^{-2}. Newer PLD set-up (large aperture galvanometer scanner) is used.

The situation like in figure 4.4c was observed, when the laser fluence was less than about 1.5 J·cm^{-2}. Thus, this can be treated as an estimation of the ablation threshold of Sc_2O_3 for 248 nm radiation and pulse length of 20 ns. Since the energy distribution over the ablation spot is still not quite homogeneous and is lower in outer regions, the value of 1.5 J·cm^{-2} can be only considered the upper limit for the real threshold value. The value obtained for the ablation threshold cannot be compared with the literature, since no Sc_2O_3 PLD-films were reported up to now. The regime, like observed in figure 4.4b, was used for deposition of Sc_2O_3 films. The laser was operating at 800 mJ per pulse, 160 mJ transmitted into the chamber, laser fluence on the target was 2.5 J·cm^{-2}.

4.3.2 Substrate

Crystalline Lattice Matching

The growth of the film is strongly influenced by the substrate, especially at the early stages of the deposition. An important factor here is the crystalline structure of the substrate (lattice symmetry and lattice constant). A suitable substrate stimulates the growth of large crystallites and define their orientation or even induce formation of a single crystalline epitaxial film. In the case of oxide films for optical applications, good crystallinity of the film will ensure high emission and absorption cross-sections of dopants and high refractive indices. However, the extremely low lattice defect density in the film is not required for optical application, as it is for example in semiconductor technology. Some other substrate properties might be essential: refractive index, to achieve guiding, and hardness, for homogeneous material removal during polishing process, are important for waveguide fabrication. Since the necessary film thickness can be in micrometer range, film cracking due to thermal stress, when cooling down after the deposition, might be an issue. Thus, matching of thermal expansion coefficients is desired. For applications in thin disk laser set-up, thermal conductivity can be a crucial factor.

In the course of this work sapphire and quartz substrates have been used. Quartz substrates have been abandoned later, due to the phase transition of α-quartz into β-quartz at 573°C. As it have been investigated by S. Ehlert [Ehl05], quartz substrates delivered unsatisfying results for deposition of sesquioxide PLD-films.

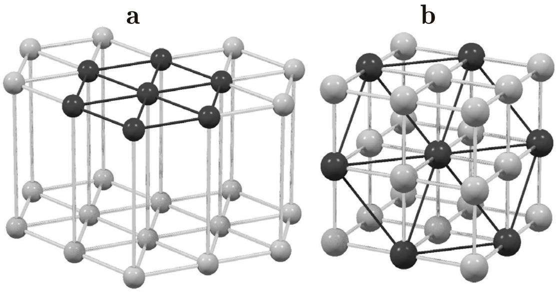

Figure 4.5: Illustration of symmetry matching of hexagonal and cubic lattices.

Both sapphire and quartz have trigonal unit cell, however their structure can also be presented as a hexagonal lattice. At the same time the cubic lattice of sesquioxides, when viewed alone <111>-direction, also show hexagonal symmetry (figure 4.5). Thus, this allows matching of cubic and hexagonal lattices, if the lattice constants are suitable. The lattice matching for different materials combinations can be characterized by a lattice mismatch parameter, which was evaluated in the following way

$$\eta=\frac{\sqrt{2}\,a_{\text{cubic}}-3\cdot a_{\text{hex}}}{\sqrt{2}\,a_{\text{cubic}}} \quad , \tag{4.3}$$

where a_{cubic} is the lattice constant of cubic sesquioxides and a_{hex} is sapphire or quartz lattice constant, which denotes the hexagon side. The mismatch in case of Sc_2O_3 and α-Al_2O_3 substrate is about 2.6%. It is also in the range of several percents for other material combinations (see table 4.1). It can be reduced by mixing two cations with different radii, e.g. mixing Sc^{3+} and Lu^{3+} in 1:1 proportion will give only 0.17% misfit.

Table 4.1. Lattice mismatch parameter (in %) for sesquioxide films on sapphire and quartz substrates.

	Y_2O_3	Sc_2O_3	Lu_2O_3	$ScLuO_3$
α-Al_2O_3	4.74	-2.62	2.82	0.17
α-SiO_2	1.74	-5.85	-0.25	-2.97

The refractive indices of sesquioxides in the visible region are in the range of 1.9-2.0. Refractive index of both sapphire and quartz are lower. This fact opens the possibility of light guiding in sesquioxide films deposited on quartz or sapphire substrates. In detail the waveguiding properties of sesquioxide films are discussed in chapter 6. Essential characteristics of substrate and film materials used in this work can be found in table 2.2.

Substrate Temperature

The temperature of the substrate determines the mobility of ions on the film surface. It has dramatical effect on crystallinity of the film.

A series of 500 nm thick Sc_2O_3 films[1] have been deposited at different substrate temperatures in order to investigate the influence of this parameter on the film properties. Except for the temperature, which has changed through the values 20°C, 300°C, 500°C, and 700°C, all the other deposition parameters have been maintained constant: $P_{O2}=1\times10^{-3}$ mbar, $\Phi=2.5\ \text{J}\cdot\text{cm}^{-2}$, $d_{\text{sub-targ}}=9.5$ cm.

The results of high resolution θ-2θ scans and rocking-curve measurements of the <222> reflection peak as well as the results of scattering and

---

[1] The samples L06-L08, L10 are discussed. Here and further in the footnotes, the samples are mentioned as they are denoted in the list of fabricated samples in appendix A.

ellipsometric measurements (refractive index) for the this films are presented in figure 4.6. Here and below in this chapter measurements have been performed and analyzed using set-ups and techniques discussed in section 3.1.

From the XRD analysis follows, that at high temperatures larger crystallites are formed. This behavior is typical for all crystalline materials, since at higher temperatures ions on the film surface have more kinetic energy and can easier reach their position in the crystalline lattice. The drop out of the crystallite size value at 500°C is believed to result from an undetermined deviation of deposition conditions. The intensity of the <222> diffraction peak increases along with the crystallite

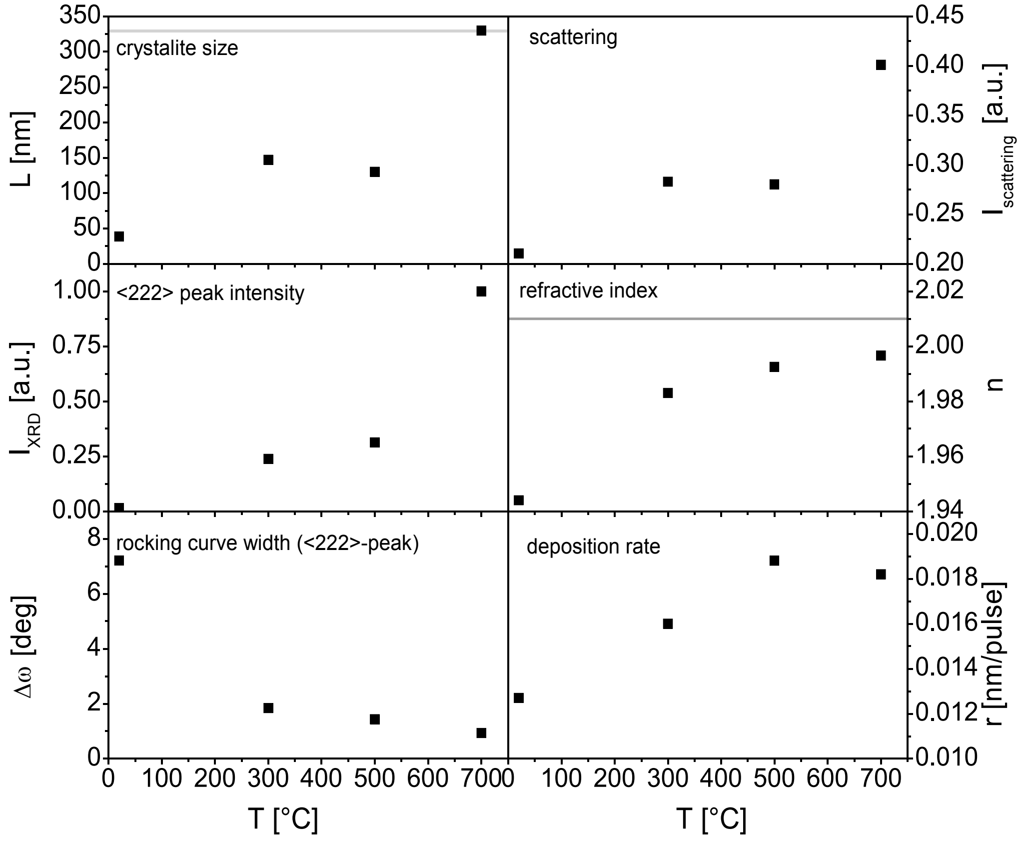

Figure 4.6: Properties of the Sc_2O_3 PLD-films deposited at different substrate temperatures. Gray lines denote: the detectable crystallite size limit determined by the resolution of diffractometer; refractive index value measured for bulk Sc_2O_3 crystal.

dimensions, which is also to expect. For the film deposited at 700°C crystallites are estimated to be larger 330 nm. The real value cannot be determined, since the width of the XRD-peak reached the limit, determined by the resolution of the diffractometer. The width of the rocking curve decreases from 7° to 1°, when the substrate temperature is increased from 20° to 700°C. The value of 1° is still much higher than the value observed for the bulk Sc_2O_3 crystals (0.11°).

It should be noted that even the film deposited at 20°C is not or only partly amorphous. Crystallite dimensions of about 50 nm were detected. This, for example, have not been observed for Y_2O_3 films deposited by PLD at room temperature [Bär04]. However, the refractive index reaches the value of Sc_2O_3 crystal only for at 700°C deposited film.

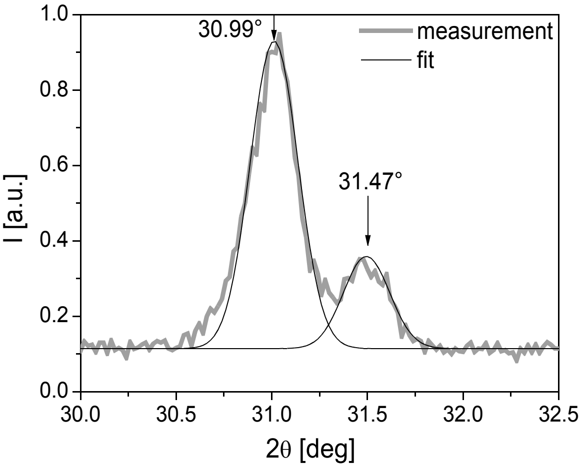

Figure 4.7: Double-peak structure of the <222> diffraction peak for the Sc_2O_3 PLD-film deposited at 20°C.

In the XRD pattern of this film a double-peak structure was observed (figure 4.7). This case should not be confused with the double-peak structure observed due to the presence of Cu-Kα1 and Cu-Kα2 emission lines (figure 3.3). Both reflection peaks at 31.47° and 30.99° are shifted from the <222> refections for Sc_2O_3 crystal (31.58°), which results from higher lattice constant 0.3% and 1.8%, respectively. This increase of lattice constant might originate from implantation of plasma ions into the film, due to their high kinetic energy. However, the formation of two distinct peaks is still not understood. A shift in <222> diffraction peak position was also observed for Yb-doped Sc_2O_3 and Lu_2O_3 films and is discussed in section 5.3.

4.3.3 Background Atmosphere

A reactive ambient atmosphere during the deposition is often used to improve the composition of the PLD-films. Since oxide films are deposited, the natural choice for the background gas is oxygen, which ensures that films are not O^{2-}deficient. Background gas is also used to control the energy of plasma particles, which can affect the film growth regime.

The partial oxygen pressure in the deposition chamber have been changed though the series[1] of Sc_2O_3 films to investigate its impact on the film properties. The other deposition parameters were maintained constant: T_{sub}=700°C, $d_{targ\text{-}sub}$=9.5 cm, Φ=2.5 J·cm^{-2}. All the films were deposited on sapphire substrates and were 500 nm thick. According to the results presented in figure 4.9, one can separate three regimes for deposition of Sc_2O_3. In the range of oxygen pressures from 10^{-3} mbar to 10^{-2} mbar crystalline films with almost identical properties were produced. The crystallite dimensions reached 330 nm. No estimation could be made beyond this limit (shown as a gray line), which is determined by the diffractometer resolution (see section 3.1). The rocking curve, showed the width of about 1°. The refractive index reached the value of the bulk crystal presented as a gray line in the figure It is ~0.02 higher as the refractive index obtained from the Sellmeier equation (1.989 at 632.8 nm).

At the lower oxygen pressure ($<10^{-3}$ mbar), which means higher kinetic energies of plasma particles, crystallites only up to 100 nm are build. The rocking curve is also broader (~2°). These both effects can be understood through the bombardment of the film by high energetic plasma particles, which produce higher density of crystallization centers. They also partly destroy the lattice of the already deposited film and break the orientation given by the underlying layers. Dense films are produced, which is confirmed by their high refractive index.

For oxygen pressure over 10^{-2} mbar the properties of the deposited films change essentially. The XRD analysis reveals, that beside the <222> diffraction peak also the <400> diffraction peak appear. For the films

---

[1] L09-L16 (appendix A).

deposited at 1.8×10^{-2} mbar and 3.4×10^{-2} mbar only the <400> reflection and no evidence of the <222> reflection have been observed. For the film deposited at 10^{-1} mbar only very weak reflection in the XRD pattern have been detected, so that quantitative analysis was not possible. Only nanocrystallites are formed under this growth conditions, possibly with portion of amorphous material. It should be noted, that ω-scan curve for <400> reflection peak was substantially narrower (0.1°) than for <222> reflections (0.5°), which means that <100>-oriented crystallites are very strong aligned in spite of quite small dimensions. Thus, it is believed, that they are only formed immediately on substrate surface. This means that two types of crystallites, <111> and <100>-oriented, are formed and no randomly oriented crystallites are present.

Background oxygen pressure has a dramatical impact on the refractive index of the deposited film (figure 4.9). The films deposited at pressure over 2×10^{-2} mbar show the drop of the refractive index values down to 1.6. These anomalous properties of the films deposited at pressures above 1×10^{-2} mbar have been already observed in the behavior of the reflectometry signal during the deposition. In figure 4.8 the reflectometry signals for the films deposited at 1×10^{-2} mbar and 1×10^{-1} mbar are presented as an example. One can note, that for the latter film the signal is inverse compared to that for the former one. For the given polarization, angle of incidence and refractive index of substrate, this can only be explained by the fact, that the refractive index of Sc_2O_3 film deposited at 1×10^{-1} mbar is lower than that of the α-Al_2O_3 substrate, whereas it is expected to be higher.

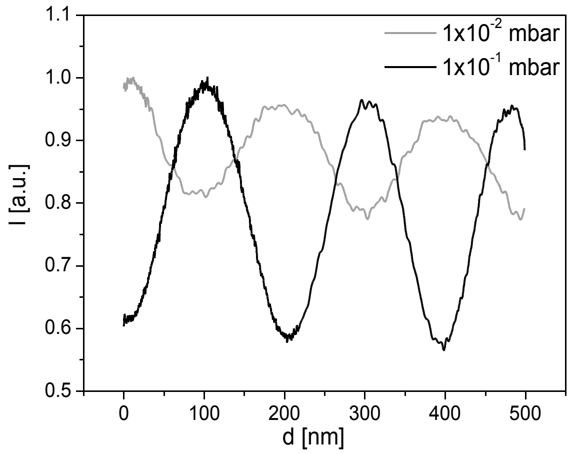

Figure 4.8: Reflectometer signals for the Sc_2O_3 PLD-films deposited at different oxygen pressures.

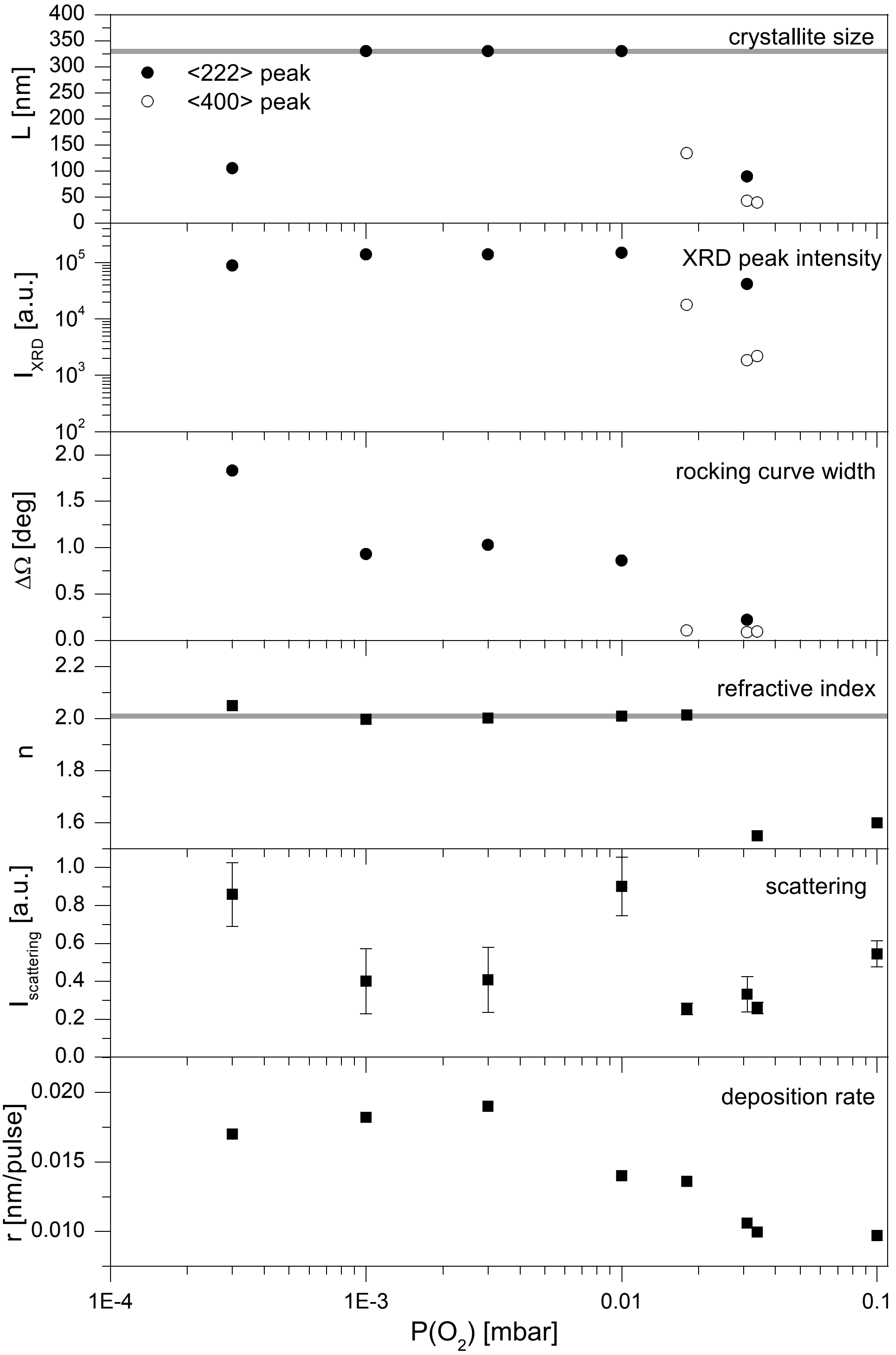

Figure 4.9: Properties of the Sc_2O_3 PLD-films deposited at different oxygen pressures. Gray lines denote: the detectable crystallite size limit determined by the resolution of diffractometer; refractive index value measured for bulk Sc_2O_3 crystal.

4.3.4 Summary and Discussion

In this section Sc_2O_3 PLD-films and influence of PLD process parameter on their properties have been discussed.

Ablation threshold of Sc_2O_3 ceramic target for KrF excimer laser radiation (248 nm, 20 ns) has been estimated to be <1.5 J·cm^{-2}. Thus, somewhat higher fluence of 2.5 J·cm^{-2} have been used for deposition of the films.

Deposition at different substrate temperatures has revealed, that even at 20°C (room temperature) films were not completely amorphous and crystallites with dimensions of about 50 nm have been detected. Crystallites with slightly larger lattice constant (up to 1.8%) have been observed in the RT-deposited film in addition to crystallites with typical Sc_2O_3 lattice. This was explained by implantation into the lattice of high energetic plasma particles. At 700°C films were highly <111>-textured and crystallites in the range of several hundreds of nanometers (>330 nm) have been observed. Real dimensions could not be determined due to the limited resolution of the used diffractometer.

Depending on the background oxygen pressure three film growth modes were observed: for pressures in the range 10^{-3} mbar – 10^{-2} mbar large crystallites (>330 nm) grew, for pressures lower 10^{-3} mbar, dense films with smaller crystallite dimensions (~100 nm) were formed, and for pressures higher than 10^{-2} mbar not quite dense films with low refractive index (~1.6) were observed. In the latter case <100>-oriented crystallites were detected in addition to typically observed <111>-oriented crystallites.

The dramatic change of film properties, when background oxygen pressure is raised over 10^{-2} mbar during the deposition, can be explained by formation of a nonsteady shock front (also called a blast wave). It is formed, when pressure of the expanding plume reaches the pressure of the background gas [Sae93b]. Inside of the plume the particles have high kinetic energies (ultrasonic expansion), which is typical for pulsed laser deposition. Behind this front the particles are thermalized and deposition will have thermal character, like by normal thermal evaporation techniques. With the increasing background gas pressure the plume is getting more confined, the effect become more pronounced and the position, where the shock front is formed, moves closer to the target. In our case, at the pressure of approximately 3×10^{-2} mbar and given laser fluence, the shock front formed as close to the target as 9.5 cm. Thus, at the higher pressures the deposition regime is more like by thermal evaporation. Plasma particles are thermalized and do not posses high kinetic energy. This causes amorphous, not very dense films with low refractive index to be produced. Low kinetic energy particles also cannot deposit enough energy to stimulate the growth of large crystallites. The formation of a shock front has been also observed, for example, during the laser ablation of high temperature superconductors [Sco90, Gup91]. The effect of refractive index change can be for example utilized to produce photonic structures (like Bragg mirrors) or waveguides using a single material, deposited under different conditions.

Another effect observed due to the increase of the background oxygen pressure is a drop of the deposition rate (figure 4.9). However, it should be mentioned, that in some case change of the deposition rate, cannot be explained by obvious change in deposition conditions, like for the series of films deposited at different substrate temperatures (figure 4.6). Thus, it was found that the deposition conditions were not fully reproducible. Two possible reasons for this behavior were later identified. Aging of the excimer gas laser caused higher voltage to be applied to achieve the predefined energy per pulse. Due to the thermal effects the laser beam profile varied. Consequently, changes in the ablation spot shape on the target were observed. Also modification of target surface in the course of the ablation influenced the deposition process.

The intensity of scattered light measured using integrating sphere do not reveal distinct dependency on any deposition parameter or film characteristics, except for substrate temperature (figure 4.6). The values are statistically distributed, as for example presented in figure 4.9 for oxygen pressure. Thus, it was concluded that this technique is not quite suitable for estimation of scattering in the PLD-films.

Summarizing the results of this section, the highest crystalline quality of the films was obtained for the substrate temperature of 700°C, background oxygen pressure of 10^{-3} mbar - 10^{-2} mbar, for the laser fluence of 2.5 J·cm^{-2} and the target-substrate distance of 9.5 cm. The temperature of 700°C degrees is the maximal achievable temperature. As it is discussed in sections 7.2.2 and 7.2.3, the higher deposition temperatures can possibly improve the film quality.

Chapter 5. X-ray Diffraction Analysis

In this chapter the results of structural characterization of ytterbia, YAG, scandia, and lutetia PLD-films by means of X-ray diffraction are presented. The crystalline quality of the deposited films is an important factor for active materials doped with rare-earth ions. The peak emission and absorption cross-sections and the excited states lifetimes of the dopants strongly depend on the quality of the crystalline lattice of the host material. Since high gain materials are preferred in order to reduce the size of active elements, high quality crystalline films are required. Moreover, an oriented crystalline growth can be desired in some cases, e.g. in order to reduce light scattering at the grain boundaries.

The XRD measurements in this chapter and their analysis were performed as described in section 3.1.

§5.1 Ytterbia Films

The ytterbia films[1] with thicknesses in the range of 20-500 nm have been deposited on sapphire and quartz substrates. The oxygen pressure during the deposition was 1×10^{-2} mbar, the substrate temperature was 700°C, and the target-substrate distance about 8 cm. The laser fluence on the target was 3.3 $\mathrm{J\cdot cm^{-2}}$. The spectroscopic properties of the ytterbia films are discussed later in section 7.2.1.

The X-ray diffraction patterns of the films are presented in figures 5.1 and 5.2, respectively, for the films deposited on (0001)-cut sapphire and quartz substrates. All the films reveal only <222> and <444> reflection peaks with no visible hints on other orientations. It should be noted, that the diffraction peaks are generally stronger for the films deposited on α-Al_2O_3

---

[1] Y01, Y02, Y04 and Y07-Y09 (appendix A).

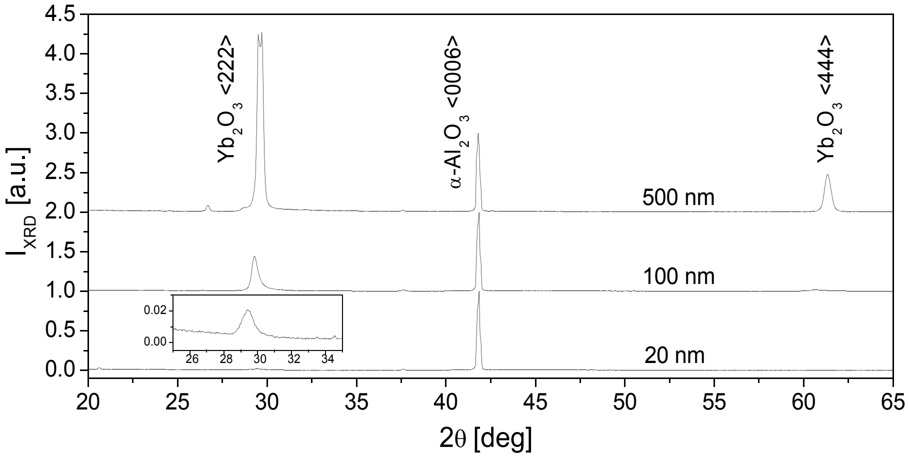

Figure 5.1: X-ray diffraction patterns of the Yb_2O_3 PLD-films deposited on α-Al_2O_3 substrates. The inset shows the magnification of the pattern for the 20 nm film.

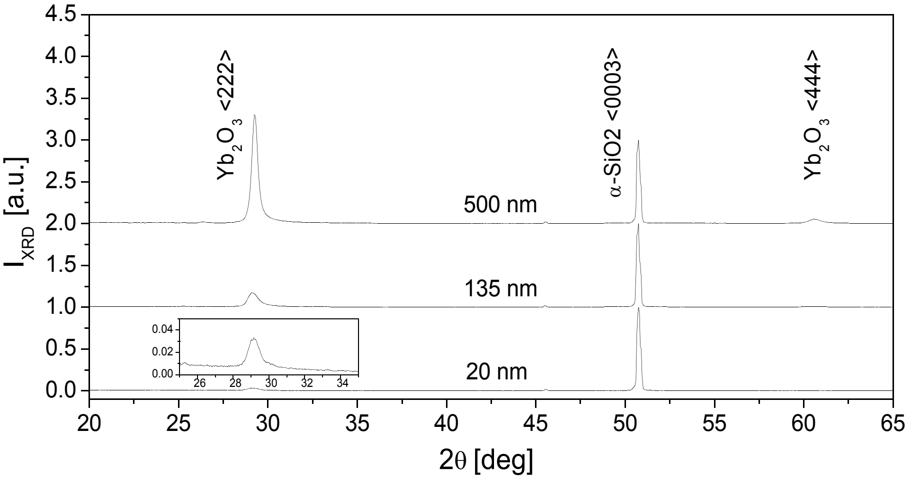

Figure 5.2: X-ray diffraction patterns of the Yb_2O_3 PLD-films deposited on α-SiO_2 substrates. The inset shows the magnification of the pattern for the 20 nm film.

Table 5.1. Results of high resolution θ-2θ and ω-scans of the <222> diffraction peak for the Yb_2O_3 PLD-films.

Sample	**ω-scan width (Δω) [deg]**	**θ-2θ peak width (Δ2θ) [deg]**	**Crystallite size (L) [nm]**
500 nm Yb_2O_3 on α-Al_2O_3	2.0	0.14	68
100 nm Yb2O3 on α-Al_2O_3	3.7	-	-
500 nm Yb_2O_3 on α-SiO_2	4	0.3	31
135 nm Yb2O3 on α-SiO_2	5.4	-	-

than on α-SiO$_2$ substrates. Also rocking-curve scans have revealed narrower peaks for the films on sapphire substrates (see table 5.1). For the both 500 nm films also high resolution θ-2θ scans of the <222> reflection peak have been performed. For the thinner films the signal was too weak. The peak widths, measured as described in section 3.1, and the dimensions of the crystallites, estimated according to equations 3.4 and 3.5, are also presented in table 5.1. The results confirm the higher crystalline quality of the films deposited on sapphire substrates. It is believed that this effect is caused by the phase transition of quartz at 573°C. As discussed in section 2.4, quartz changes its structure from the β- into the α-form when the sample is cooled down after the deposition. This rapid change in crystal structure of the substrate deteriorates the structure of the film.

§5.2 YAG Films

In this section the structural characterization of YAG PLD-films doped with ytterbium is presented. Again, the spectroscopic properties of the films and their possible application and their are discussed later in section 7.2.3.

Two YAG PLD-films[1] have been prepared, one on a sapphire substrate and one homoepitaxially on a YAG substrate. Both films were about 4 µm thick and were deposited under the same conditions: T_{sub}=700°C, $d_{targ\text{-}sub}$=9 cm, $P_{O2}=1\times10^{-2}$ mbar, Φ=2.5 J·cm^{-2}. The ytterbium dopant concentration was 10 mol.% for both films. The deposition rate achieved was approximately 0.014 nm/pulse. Both samples were cut in two parts and one part of each sample was annealed in air at 1200°C for 1 hour.

Both “as deposited” samples proved to be amorphous, since no diffraction peaks apart from the substrate peaks were detected (figure 5.3). For the homoepitaxially grown sample the substrate and film diffraction some peaks coincide and can not be separated. However, the spectroscopic investigations confirmed, that no YAG phase was formed in this case as well (section 7.2.3). After annealing the films have shown polycrystalline

---

[1] Y14 and Y15 (appendix A).

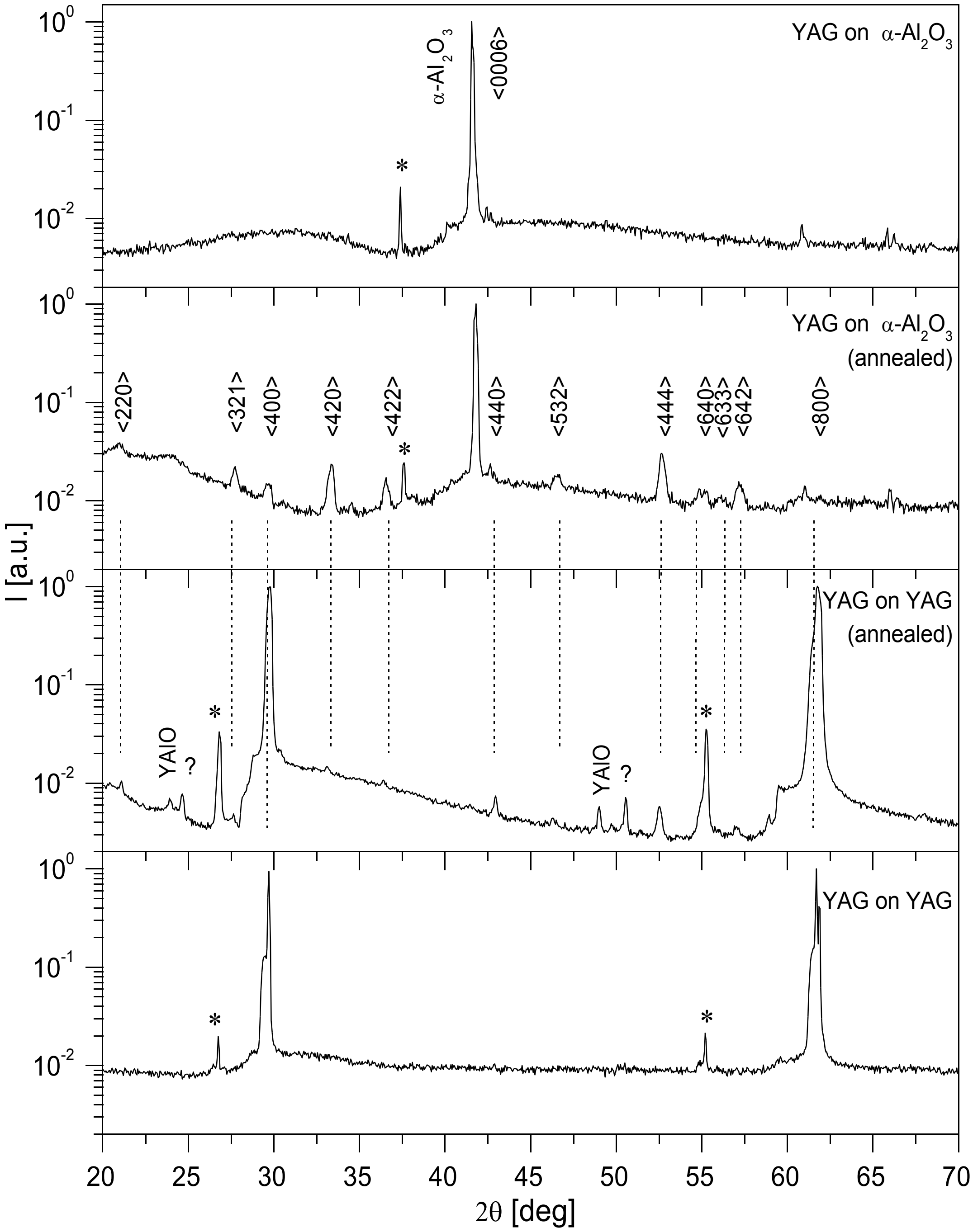

Figure 5.3: X-ray diffraction patterns of the Yb:YAG PLD-films. "$*$" denote diffraction peaks resulting from the residual Cu-Kβ emission. "?" denote diffraction peaks that can not be associated with the YAG lattice.

behavior. A number of diffraction peaks, characteristic for the YAG structure, have been detected. All the peaks are very weak and quite broad, which indicates that only crystallites with dimensions in the nanometer range have been formed. The YAG film grown homoepitaxially also revealed some peaks that could not be associated with the YAG lattice. Some of them can be assigned to the $YAlO_3$ - perovskite phase of the Y-Al-O mixture. The annealed films show spectroscopic properties similar to that of the Yb:YAG bulk crystal. Thus, it can be concluded that the temperature of 700°C is not sufficient for the YAG crystal structure to be formed and that temperatures up to 1200°C are needed to thermally initiate the growth of YAG crystallites.

§5.3 Lutetia and Scandia Films

This section presents the results of structural investigations of ytterbium-doped lutetia and scandia films[1] by X-ray diffraction. The spectroscopic properties of the films are discussed later in section 7.2.2. Two $Yb{:}Lu_2O_3$ films have been deposited on a (0001)-oriented α-Al_2O_3 and on a (111)-oriented Lu_2O_3 substrates, respectively. In the similar way two $Yb{:}Sc_2O_3$ films have been produced on a (0001)-oriented α-Al_2O_3 and on a (111)-oriented Sc_2O_3 substrates. The Yb^{3+} concentration was 5 mol.% and 4 mol.% for Lu_2O_3 and for Sc_2O_3 films, respectively. The films have been produced under the same conditions as the YAG films discussed above in section 7.2.3. The lutetia films were 3.3 μm and 3.5 μm thick for the films deposited on sapphire and on lutetia substrates, respectively. Both scandia films were 4 μm thick. The films deposited on sapphire substrates were cut in two parts and one half of each sample was annealed in air at 900°C for 1 hour.

Lutetia Films

In figure 5.4 the X-ray diffraction patterns for Lu_2O_3 films are presented. For the homoepitaxially grown film only <222> and <444> reflection peaks are present in the diffraction pattern. The peaks are asymmetric and broader than those of the uncoated Lu_2O_3 substrate. The film

---

[1] Y10-Y13 (appendix A).

deposited on the sapphire substrate shows polycrystalline behavior. Beside the expected <222> and <444> reflection peaks also <211>, <440>, and <622> reflection peaks are present in the diffraction pattern. All the peaks are quite broad, but after annealing the peak widths are reduced. In order to evaluate this effect quantitatively, high resolution scans of the <222> reflection peaks have been performed (figure 5.5). The peak widths were measured as described in section 3.1 and crystallites dimensions have been estimated using equations 3.4 and 3.5. Also rocking curves were recorded for all the films as well as for a Lu_2O_3 substrate, which was used as a reference. The results are summarized in table 5.2. One can see that for the film deposited on the sapphire substrate only quite small crystallites of 25 nm were formed; after annealing the crystallite size increased up to 47 nm. Also the width of the rocking curve slightly decreased from 3.8° to 3.0° after annealing.

Another effect to be noted is the diffraction peak position. For the film deposited on sapphire substrate the peaks are shifted by 0.37° in the direction of lower values in comparison with the bulk crystal. According to equation 3.1, this means that the lattice constant for Lu_2O_3 film is about 1.2% larger than that for the Lu_2O_3 crystal (10.391 Å). After annealing the peak moved to the position almost corresponding to the

Table 5.2. Results of high resolution θ-2θ and ω-scans of the <222> diffraction peak for the $Yb:Sc_2O_3$ and $Yb:Lu_2O_3$ PLD-films.

Sample	**ω-scan width (Δω) [deg]**	**θ-2θ peak width (Δ2θ) [deg]**	**Crystallite size (L) [nm]**
Lu_2O_3 crystal	0.15	0.042	-
Lu_2O_3 on α-Al_2O_3	3.8	0.37	25
Lu_2O_3 on α-Al_2O_3 (annealed)	3.0	0.20	47
Lu_2O_3 on Lu_2O_3	0.6	0.049	>330
Sc_2O_3 crystal	0.082	0.042	-
Sc_2O_3 on α-Al_2O_3	0.78	0.049	>330
Sc_2O_3 on α-Al_2O_3 (annealed)	0.65	0.063	195
Sc_2O_3 on Sc_2O_3	0.092	0.038	>330

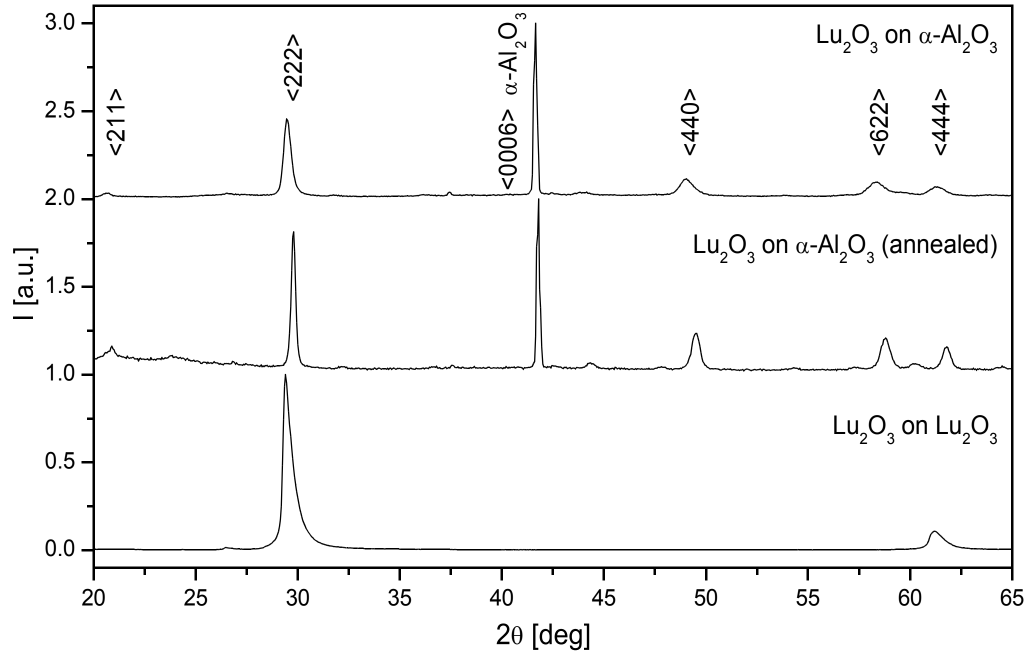

Figure 5.4: X-ray diffraction patterns of the Yb:Lu_2O_3 PLD-films.

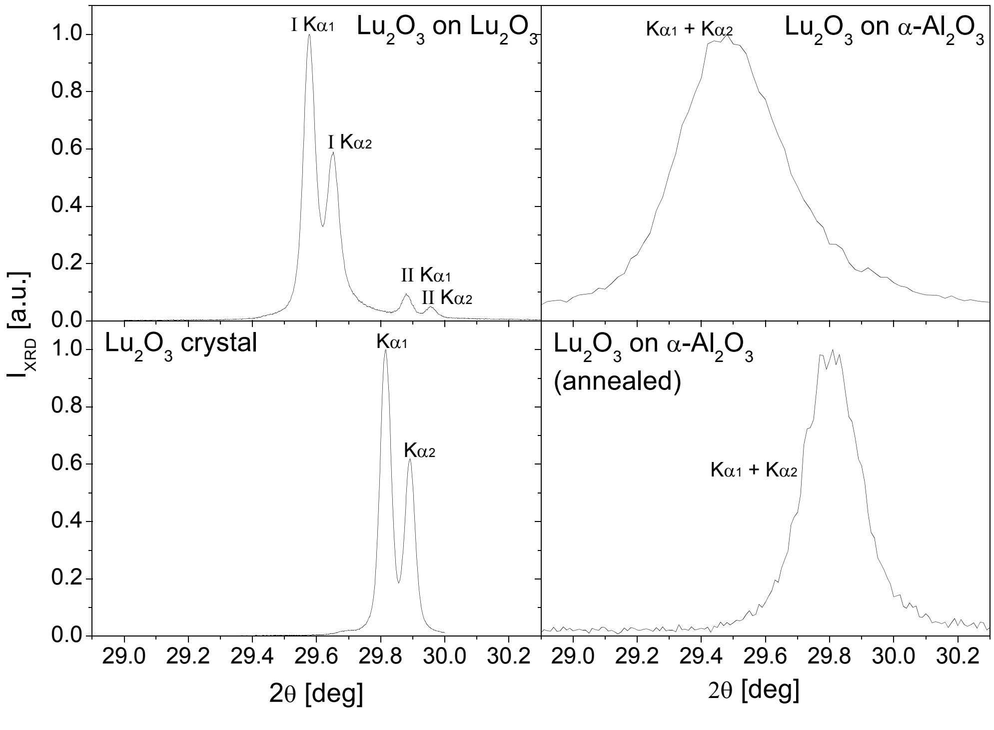

Figure 5.5: High resolution θ-2θ scans of the <222> diffraction peak for the Yb:Lu_2O_3 PLD-films.

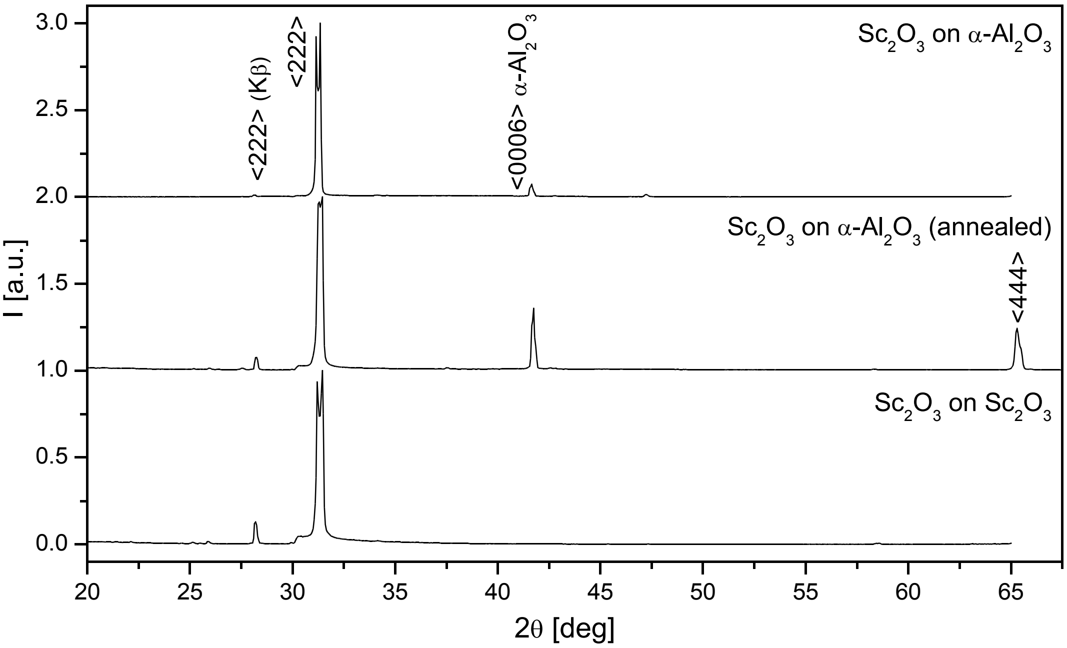

Figure 5.6: X-ray diffraction patterns of the Yb:Sc$_2$O$_3$ PLD-films.

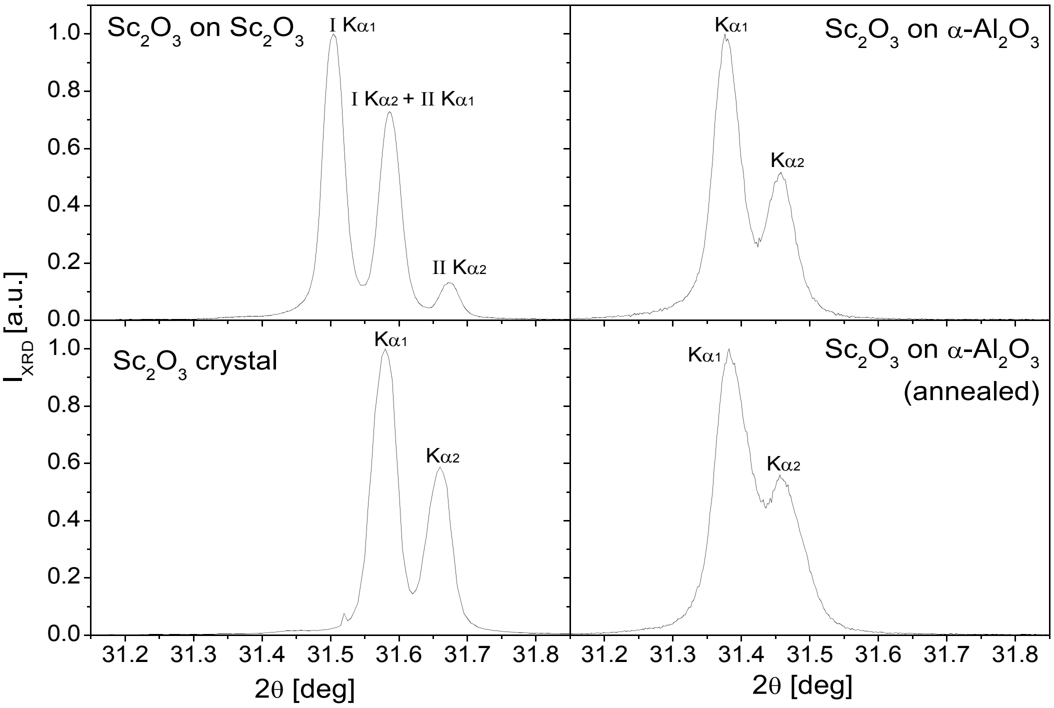

Figure 5.7: High resolution θ-2θ scans of the <222> reflection peak for the Yb:Sc$_2$O$_3$ PLD-films.

bulk crystal value. The residual shift was only 0.02°, which lies within an experimental error.

In the diffraction pattern of the homoepitaxially deposited film unexpectedly two peaks are observed. The first peak is believed to be associated with the deposited film, whereas the second peak belongs to the substrate. The rocking curve for the <222>-peak originating from the film is broader (0.6°) than that for the bulk crystal (0.15°). The lattice constant is by 0.8% larger for the Lu_2O_3 film compared to the Lu_2O_3 crystal. The peak width for the homoepitaxial film reached the resolution limit and the estimated crystallite size is >330 nm.

Scandia Films

Figure 5.6 presents the X-ray diffraction patterns for the Sc_2O_3 films. In contrast to the Lu_2O_3 films discussed above, all Sc_2O_3 films reveal only <222> and <444> reflections. One should also note the intensity of the <222> reflection peaks, which are even stronger than the reflection of the Al_2O_3 substrate. This indicates the high crystallinity of the films.

High resolution θ-2θ scans for the scandia films are presented in figure 5.7 (see section 3.1 for the experimental details). The estimated crystal dimensions as well as the results of the rocking-curve scans can be found in table 5.2. The scandia films reveal much better crystallinity than the lutetia films. The peak width for the film grown on the α-Al_2O_3 substrate is close to the resolution limit and the crystallites are estimated to be larger 330 nm. Unexpectedly, the annealing of the Sc_2O_3 film caused a certain broadening of the <222> reflection peak, so that the estimated crystallite size decreased down to approximately 200 nm. The film grown homoepitaxially revealed the <222> reflection peak to be as narrow as the bulk crystal one, which means that the real reflection width is below the resolution of the diffractometer.

As in the case with the lutetia films, a shift of the <222> reflection peak position was observed and two <222> reflection peaks were detected for the homoepitaxially grown film. The peaks were shifted by 0.2° and 0.08°, respectively for the film grown on sapphire and for the homoepitaxially grown film. This corresponds to about 0.6% and 0.25% lattice constants increase. Annealing did not influence the peak position and, correspondingly, the lattice constant in the case of scandia.

§5.4 Summary and Discussion

The X-ray diffraction analysis of the PLD-films presented in this chapter showed, that the ytterbia, lutetia, and scandia films form a cubic lattice typical for these sesquioxides and the crystallites are preferably <111>-orientated.

Sc_2O_3 films have been proved to be highly textured in <111>-direction. Crystallites with the dimensions of several hundred nanometers have been formed. In some case the resolution limit of the diffractometers have been reached so that only the lower limit for the crystallite's size could be estimated.

Substantially smaller crystallites are formed in Yb_2O_3 films (up to ~70 nm) and Lu_2O_3 films grown on sapphire substrates (up to ~50 nm). The Lu_2O_3 film grown homoepitaxially revealed crystallites in the range of hundreds nanometers. Additionally, the lutetia films revealed crystallite orientations other than <111>. Lu^{3+} and Yb^{3+} have higher mass compared to Sc^{3+}, which means, that at the same temperature Lu- and Yb-ions will have lower mobilities in comparison with lighter Sc-ions. Thus, the higher mobility of the Sc-ions on the substrate surface is believed to stimulate the growth of larger crystallites. In case of the ytterbia films a higher laser fluence was used during the deposition. Hence, higher kinetic energies of the plasma particles seem to compensate for the lack of thermal energy of the ions.

In the upper layers of the 3.3 μm thick Lu_2O_3 film grown on α-Al_2O_3 the <111> orientation predefined by the substrate is apparently lost, due to the substantially smaller size of crystallites compared to the film thickness and, consequently, a high density of the grain boundaries. This was evidenced by the presence in the XRD patterns of the diffraction peaks corresponding to other orientations. Perfect lattice matching in case of homoepitaxial growth initiates the formation of larger, strongly orientated crystallites, so that the orientation predefined by the substrate is preserved at the film thickness of 3.5 µm.

The lattice constants for the PLD-films have been found to be slightly larger compared to the bulk crystal values by up to 1.2% for Lu_2O_3 and up to 0.6% for Sc_2O_3. This effect may originate from the high kinetic energies of the ions in the plasma plume. The ions are not only deposited on the surface, but are also implanted into the already formed lattice and disturb its structure. Due to the relatively low temperature during the deposition (700°C) compared to the melting point (~2400°C), the recrystallization effect might be limited. After annealing at 900°C the lattice constant for the lutetia film was almost equal to the crystal value. In the case of the scandia films post annealing have no effect on the lattice constant. The increase of the lattice constant can also result from the relatively high concentration (4 mol.%) of the Yb^{3+}-ions in Sc_2O_3 films, which are larger (0.87 Å) compared to the Sc^{3+}-ions (0.75 Å). Whereas the radius of Lu^{3+} (0.86 Å) is almost equal to that of Yb^{3+}. The fact, that annealing do not influence the lattice constant of scandia films, confirms, that in this case the effect is most probably due to the dopant.

Yb-doped YAG films deposited on α-Al_2O_3 and YAG substrates at 700°C did not reveal any indications of a crystalline YAG structure. Only randomly oriented YAG nanocrystallites have been formed after annealing of the samples at 1200°C. This correlates with the annealing experiments with thin amorphous Eu:Y_2O_3 films on sapphire substrates [Bär05]. The films showed typical Eu:Y_2O_3 emission spectra for annealing temperatures up to 1000°C; above 1000°C emission lines assigned to Eu:YAG were also detected in the emission spectrum. On the other hand, Ezaki *et al.* [Eza96] reported crystalline growth of pulsed- laser-deposited YAG films starting from 500°C substrate temperature. However, these films were deposited under ultra-high vacuum conditions ($\sim 1 \times 10^{-7}$ mbar). Also gadolinium-gallium garnet (GGG) films, which have the same structure with YAG, have been shown to grow in a crystalline form at relatively low temperatures of 650°C [Gri04b] (Nd:GGG) and up to 800°C [Lan05] (Pr:GGG). In both reports relatively high oxygen pressures of 2-5 $\times 10^{-2}$ mbar were used; however, the target-substrate distance was as short as ~5 cm. It is believed, that the high kinetic energy of the plasma particles, due to low oxygen pressure or short working distance, contributed to the crystalline growth. Another reason, that can hinder the growth of crystalline YAG films in our case, is quite high concentration of Yb^{3+}-ions (10 mol.%). Yb^{3+} has a different mass and ionic radius compared to Y^{3+}, which can influence the YAG lattice formation.

Chapter 6. Waveguiding Sesquioxide PLD-Films

The introduction of this chapter discusses the motivation for the fabrication of waveguiding films and introduces basics of waveguide theory as well as the concept of the waveguide laser. Then the results of spectroscopic and waveguiding characterization of produced PLD-films are presented. First waveguiding experiments have been performed with a Eu:Y_2O_3 PLD-film. The emphasis, however, is placed on the spectroscopic and waveguiding characterization of Nd:Sc_2O_3 films. The analysis of the propagation losses of the waveguiding films has been performed as well. Finally the results of the first structuring experiments are presented at the end of the chapter.

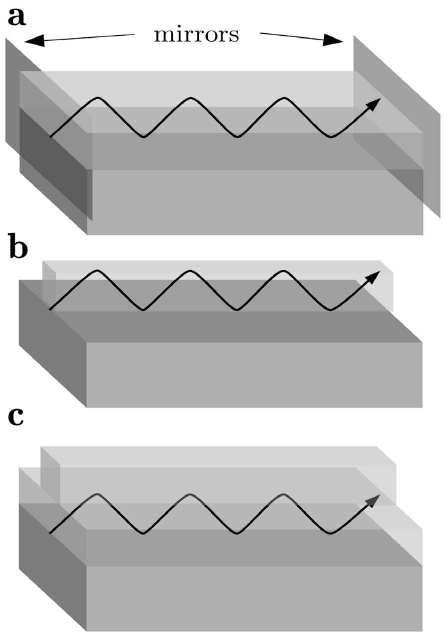

Figure 6.1: Illustration of: (a) planar waveguide, mirrors can be placed to provide feedback for the laser action; (b) channel waveguide; (c) rib waveguide geometry.

§6.1 Introduction

Recently, compact elements for integrated optical devices have acquired much attention, since they are promising for communication, data processing and sensing applications. A variety of individual elements for integrated optics – e.g. light amplifier [Kik03], logic gate [Ibr04], micro ring resonator [Ger04, Dri04] – have been already reported. However, a number of individual elements are still to be developed. Two of the key elements are laser light sources and amplifiers. The most favorable configuration in this case is a waveguide. The main advantages of waveguide lasers are low threshold, due to confined prorogation of emission and pump light, and compactness. The starting point for realization of such a laser or amplifier is a planar waveguide (figure 6.1a). In many cases light confinement in two dimensions is required, thus a channel waveguide could be a solution in this case (figure 6.1b). A similar effect can be achieved by depositing a rib on the planar waveguide (figure 6.1c), so that the light is confined in lateral direction due to the effective refractive index change. Either external or directly onto the end faces deposited mirrors should be used to provide the feedback in order to achieve laser oscillation (figure 6.1a).

Active optical elements like light emitters or amplifiers require high gain materials in order their size can be reduced. Neodymium-doped materials, which are well known for high gain and effective laser operation, fulfill this requirements. The following Nd-doped waveguiding PLD-films have been already reported: Nd:YAG [Cha92], Nd:GGG [Gil96, Gri04a], Nd:YAP [Son98], Nd:KGW [Ata00]. The waveguide laser operation have been demonstrated in the garnet (YAG and GGG) films. Apart form the Nd-doped films , laser action in a Ti:Al_2O_3 PLD-film was achieved [And97]. Thus, PLD seems to be a favorable technique for the deposition of active oxide films.

Beside the well known YAG also scandia is a promising host material for RE-ions. It exhibits higher thermal conductivity than YAG and rare earth ions in scandia have high absorption and emission cross-sections. Scandia also exerts a very high crystal field on rare earth ions, which, for example, causes neodymium to provide spectral lines on wavelengths, that are not achievable in other host materials. This property of Nd:Sc_2O_3 can be favorable for sensing or spectroscopic applications. Effective laser action in bulk Nd:Sc_2O_3 has been demonstrated by Fornasiero *et al.* [For99a]. Due to the high emission and absorption cross-sections of Nd:Sc_2O_3, the laser generation in the waveguide configuration should be achievable as well.

6.1.1 Theory of Waveguiding

In this section the basic ideas of waveguiding are discussed. Different models describing this phenomenon can be found in the literature. The approach presented here is based on the considerations of Yariv [Yar89] and Lee [Lee86], as well as on more recent analysis by Bonner [Bon00] and Bär [Bär04].

In the simplest way waveguiding of light in a layered structure can be explained in a geometrical optics model. Let us consider a layer of dielectric material, which is surrounded by substrate at the bottom and superstrate at the top (figure 6.2). If the refractive index of the layer is larger than that of the surrounding media, then the light, which is traveling in the layer at the angles (θ) larger than a certain angle (θ_{crit}), is not transmitted into those media. The expression for the critical angle θ_{crit} is given by

$$\sin(\theta_{crit})=\frac{n_{sub,sup}}{n_f} \quad . \tag{6.1}$$

The propagation of the light in the waveguide is usually described in terms of wave vectors and not angles. For the light propagating in a medium with the refractive index n its value is given by $|\vec{k}|=\frac{2\pi n}{\lambda}$, where λ is the light wavelength in free space. Then for light propagating in the layer the wave vector projection on the z-axis will be $k_z=\frac{2\pi n_f}{\lambda}\sin(\theta)$. The

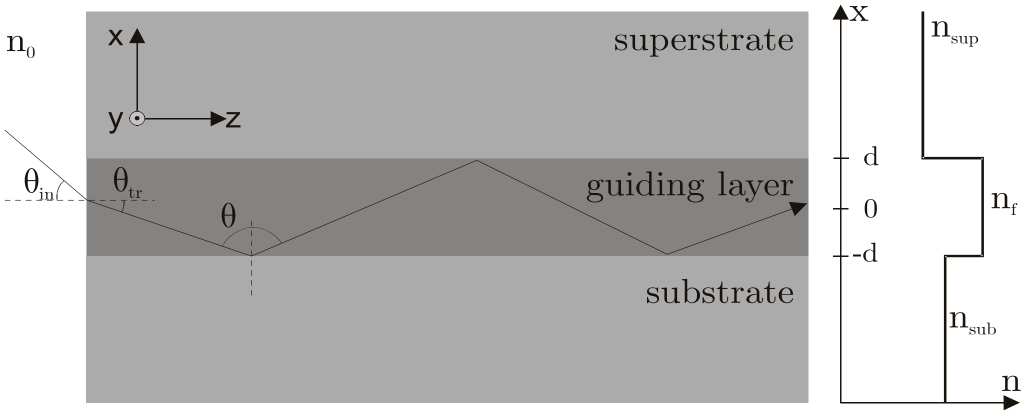

Figure 6.2: Propagation of light in planar waveguide.

quantity $n_f \sin(\theta)$ is often denoted as the effective refractive index n_{eff}. The guidance condition $\theta > \theta_{crit}$ is satisfied, if $n_{eff} > n_{sub,sup}$.

The restriction for the coupling angles (θ_{in}), which result in guiding of light can also be derived from the guidance condition $\theta > \theta_{crit}$

$$n_0 \sin(\theta_{in}) < \sqrt{n_f^2 - n_{sub,sup}^2} \quad . \tag{6.2}$$

The quantity $n_0 \sin(\theta_{in}^{max})$ is more convenient from the experimental point of view and is referred to as numerical aperture of the waveguide (NA).

However, the geometric optics model cannot give the accurate consideration of all effects. Thus, for example, a discrete number of guided modes can not be explained. The correct treatment of the subject can be derived from Maxwell's equations

$$\nabla \times \vec{E}(\vec{r},t) = -\frac{\partial \vec{B}(\vec{r},t)}{\partial t} \tag{6.3}$$

$$\nabla \times \vec{H}(\vec{r},t) = \frac{\partial \vec{D}(\vec{r},t)}{\partial t} + \vec{j}(\vec{r},t) \tag{6.4}$$

$$\nabla \cdot \vec{D}(\vec{r},t) = \rho(\vec{r},t) \tag{6.5}$$

$$\nabla \cdot \vec{B}(\vec{r},t) = 0 \quad , \tag{6.6}$$

where $\vec{E}$ and $\vec{B}$ are the electric and magnetic fields respectively, $\vec{D}$ is the electric displacement vector, $\vec{H}$ is the magnetic flux density, ρ and $\vec{j}$ are charge and current densities, respectively. In the case of isotropic dielectric media ($\rho = 0$, $\vec{j} = 0$, $\vec{D} = \varepsilon \vec{E}$, $\vec{B} = \mu \vec{H}$) the equation for $\vec{E}$ is given by

$$\nabla^2 \vec{E} = \frac{n^2}{c^2} \frac{\partial^2 \vec{E}}{\partial t^2} \quad , \tag{6.7}$$

which is termed the wave equation. The solution for equation 6.7 can be presented in the following form

$$\vec{E}(x,y,z,t) = \vec{E}(x,y,z) \mathrm{e}^{i\omega t} \quad . \tag{6.8}$$

Due to translation symmetry along the y-axis ($\frac{\partial \vec{E}}{\partial y}=0$) in the case of a planar waveguide (as presented in figure 6.2), this general solution splits into two groups: (1) $E_z=E_x=H_y=0$ ($\vec{E}$ is transversal to the incidence plane), referred to as TE-modes; (2) $H_z=H_x=E_y=0$ ($\vec{H}$ is transversal to the incidence plane), referred to as TM-modes.

In the following consideration, only transversal electrical (TE) modes are considered, the transversal magnetic modes can be treated analogously. In the case of a planar waveguide the solution for the TE-modes can be written as

$$E_y(x,y,z,t)=E_y(x)\mathrm{e}^{i(\omega t-k_z z)} \quad . \tag{6.9}$$

In order for the light to be guided, the solutions should be oscillating in the guiding layer and decaying in the substrate and superstrate. So we search solutions in the following form

$$E_y=\begin{cases} E_{\mathrm{sup}}\mathrm{e}^{-\alpha_{\mathrm{sup}}x} & ,x>d \\ E_{\mathrm{f}}\cos(k_x x+\psi) & ,-d\leqslant x\leqslant d \\ E_{\mathrm{sub}}\mathrm{e}^{\alpha_{\mathrm{sub}}x} & ,x<-d \end{cases} \quad , \tag{6.10}$$

where $E_{\mathrm{sup,sub,f}}$ are the electric field amplitudes in the corresponding regions, ψ is the phase shift, $\alpha_{\mathrm{sup,sub}}$ and k_x are the wavenumbers, which are derived from the solution of the wave equation 6.7 and are given by

$$\begin{aligned} \alpha_{\mathrm{sup}}&=k\sqrt{n_{\mathrm{eff}}^2-n_{\mathrm{sup}}^2} \\ k_x&=k\sqrt{n_{\mathrm{f}}^2-n_{\mathrm{eff}}^2} \\ \alpha_{\mathrm{sub}}&=k\sqrt{n_{\mathrm{eff}}^2-n_{\mathrm{sub}}^2}\,. \end{aligned} \tag{6.11}$$

From the continuity condition $\frac{\partial E_y}{\partial x}=0$ at the interfaces $x=\pm d$, one can eliminate the phase ψ and the following equation can be obtained

$$2k_x d-\arctan\frac{\alpha_{\mathrm{sup}}}{k_x}-\arctan\frac{\alpha_{\mathrm{sub}}}{k_x}=p\pi \quad . \tag{6.12}$$

This equation is termed a mode guidance condition for the mode number p. Solving this equation for the mode p, one can determine, if the mode is guided (solution can be found), and obtain n_{eff} for this mode. Thus α_{sup}, α_{sub}, and k_x can be determined and the mode intensity profile $I(x)=|\vec{E}(x)|^2$ can be calculated.

§6.2 Eu-doped Yttria Waveguide

Eu:Y_2O_3 is a very well studied material and is widely used as a phosphor. First stimulated emission studies of Eu:Y_2O_3 have been performed in the 1960es [Cha63] and a first report of an yttria waveguide found in the literature is [Cha72]. Lately also yttria waveguides produced by pulsed laser deposition have been reported: Eu/Er:Y_2O_3 [Via00], Er:Y_2O_3 [Kor01]. The first waveguiding experiments in the course of this work have been performed with an Eu:Y_2O_3 PLD-film.

A 1.2 µm thick Eu-doped yttria waveguide has been deposited on a $10\times10\times0.5$ mm^3 both-sides-polished quartz substrate[1]. The substrate temperature during the deposition was 700°C, background atmosphere was oxygen with the pressure of 1×10^{-2} mbar. The excimer laser was operating at 20 Hz, energy density at the target was 3.3 J·cm^{-2}. The achieved deposition rate was 0.0047 nm/pulse (older PLD set-up with small aperture, piezo-driven mirror was used, see section 4.2). The Eu^{3+}-dopant concentration was 2 mol.%. After the deposition two end faces of the sample were polished in order to be able effectively launch light into the film. The length of the sample after polishing was approximately 6 mm.

6.2.1 Optical Spectroscopy

All the Eu^{3+}-doped materials reveal relatively intense red-orange luminescence in the range 610 nm – 620 nm, depending on the host. This emission is caused by a strong $^5D_0\rightarrow{}^7F_2$ transition and is widely utilized in the Eu-doped phosphors. This transition reveals a hypersensitive behavior with respect to the crystal field, therefore Eu^{3+} can also be used as a

---

[1] W06 (appendix A).

probe of crystalline quality of deposited films.

In figure 6.3 the emission spectrum of the Eu:Y_2O_3 film is shown. Only some minor deviations from the bulk spectrum can be observed. The width of the 611 nm line for the PLD-film is 1.7 nm, which is only 0.2 nm broader than for the bulk crystal spectrum. This confirms the high crystalline quality of the deposited film. For example emission spectra for amorphous Eu:Y_2O_3 films [Bär04] or the monoclinic phase of Eu:Y_2O_3 [Lan04] reveal essential deviations form the bulk crystal spectrum.

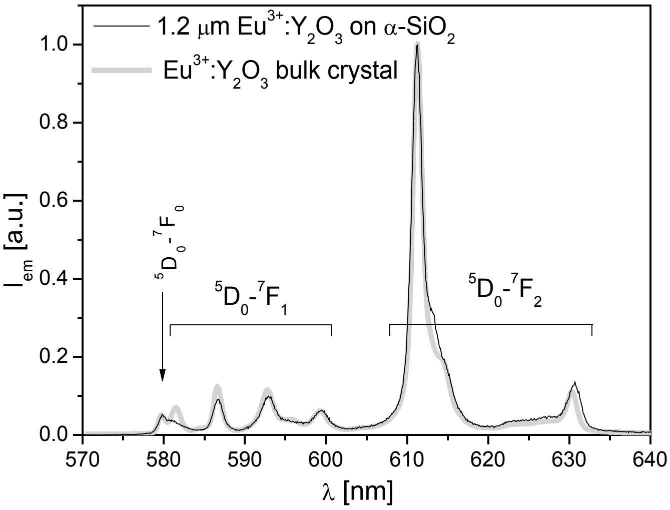

Figure 6.3: Emission spectra of the 1.2 μm Eu:Y_2O_3 PLD-film and Eu:Y_2O_3 bulk crystal (λ_{ex}=240 nm).

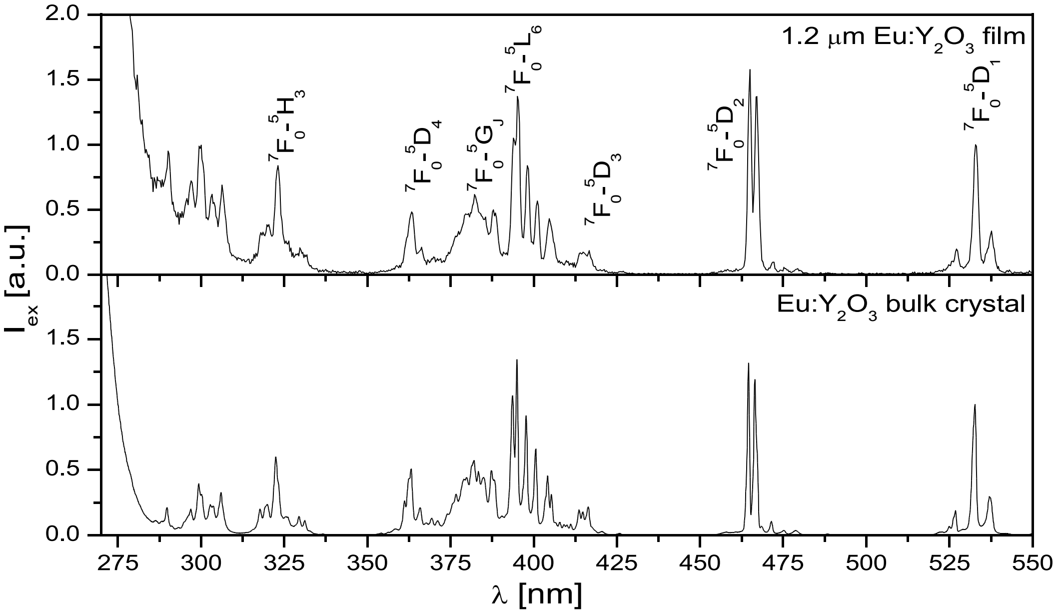

Figure 6.4: Excitation spectra of the 1.2 μm Eu:Y_2O_3 PLD-film and Eu:Y_2O_3 bulk crystal (λ_{em}=611 nm).

Figure 6.4 presents the excitation spectrum of the same PLD-film. The spectrum is very close to the corresponding bulk crystal spectrum down to 350 nm. In the range of shorter wavelengths one can observe the slowly rising edge of the very strong wide band, which starts only at ~280 nm for the bulk Eu:Y_2O_3. This band is an absorption into the charge transfer (CT) state, which is often utilized to excite the Eu^{3+} emission, since the excitation from the CT-state is very efficiently transferred to ^5D_J states of Eu^{3+}. This expansion of the charge-transfer absorption band to the longer wavelength is believed to be related to the imperfection of the crystalline lattice of the Eu:Y_2O_3 PLD-film.

6.2.2 Waveguiding Experiments

Experimental Setup

Waveguiding experiments with the Eu:Y_2O_3 film have been performed using the set-up presented in figure 6.5. The light emitted by a GaN laser diode (Toptica DL100) was focused into the PLD-film by a triplet with 6.5 mm focal length. The laser was operating at the wavelength of 398 nm, which very good coincide with one of the absorption lines of the $^7F_0 \rightarrow {}^5L_6$ transition of the Eu^{3+}-ion. The sample was clamped in a specially designed plastic holder, which was installed on a precision 3D positioning table. The end face of the waveguide has been imaged by a 50x microscope objective onto a CCD-chip of a video camera operated without any lens. The image from the camera has been captured using a computer. Image magnification could be adjusted by positioning the camera at various distances from the sample end face. The imaging

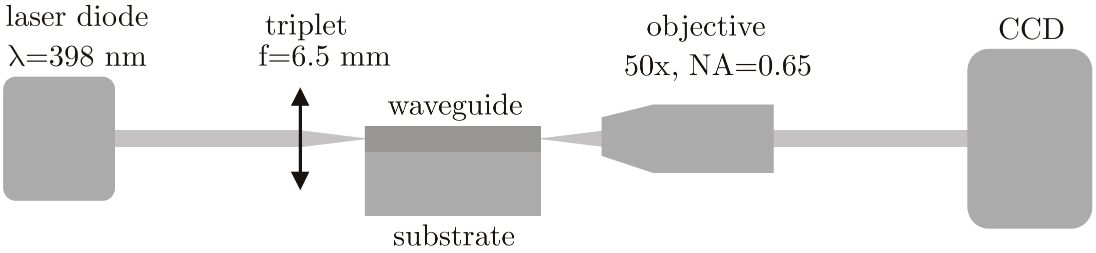

Figure 6.5: Scheme of set-up used for waveguiding experiments with the Eu:Y_2O_3 PLD-film.

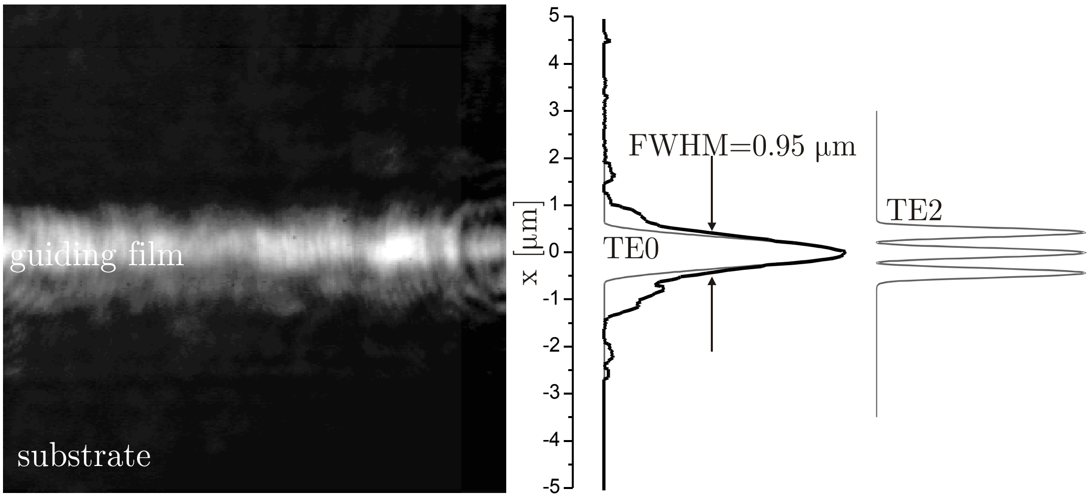

Figure 6.6: Image of the guiding 1.2 μm thick Eu:Y_2O_3 film deposited on α-SiO_2 substrate, when 397 nm laser-diode radiation is coupled in (left). The integrated intensity profile and the calculated profiles for TE0 and TE2 modes (right).

objective and the triplet were mounted on positioning tables similar to the sample table. This configuration allowed maximum flexibility in the experiments. In some experiments a He-Ne laser was used as light source instead of the laser diode.

Discussion of Results

In the course of the experiments light has been successfully coupled into the Eu:Y_2O_3 PLD-film and guiding has been achieved. However, due to the thickness of only 1.2 μm, the set-up was very sensitive. Even minor displacements cause the coupling to be disrupted. A typical image observed with the camera is shown in figure 6.6. According to equation 6.2, the quite large refractive index difference (n=1.963 for Y_2O_3 and 1.568[1] for α-SiO_2 at λ=397 nm), causes all the light coupled into the film to be guided. Light guiding has been also achieved, when He-Ne laser emission (λ=632.8 nm) was coupled into the film.

The integrated profile of the guided light is present in the right part of figure 6.6. For comparison also calculated (equations 6.10-6.12) TE0 and

---

[1] Ordinary refractive index, experienced by a TE-guided mode in Y_2O_3-film on a <0001>-oriented α-SiO_2 substrate, is mentioned here.

TE2 mode profiles are given. In the center part the TE0 mode coincides quite well with the experimentally measured profile. The wings, however, show substantial deviation. This broadening is possibly caused by stronger scattering at the film interface to the air and to the substrate. This effect can be also due to the limited objective resolution or charge diffusion in the CCD-chip. For example, noticeable broadening of the image has been observed, when an objective with a lower NA and magnification (20x, NA=0.4) was employed.

One should also note inhomogeneous intensity distribution along the end face of the waveguide. It is believed that this effect is caused by scattering of light at at inhomogeneities inside the film or at the film surface. Since coherent laser emission is used, additionally interference effects can occur. Such behavior for example have not been observed for an amorphous 1µm thick Y_2O_3 waveguide produced by electron beam evaporation (EBV) [Kuz04].

Since the 397 nm emission of the laser diode meets the absorption line of Eu^{3+} ($^7F_0 \rightarrow {}^5L_6$), the typical red-orange europium luminescence is excited. It has been visually observed through a low pass filter, which blocked the bright blue laser emission. It is believed, that the red emission is also guided in the film, although an attempt to detect this guided red emission with a camera failed, presumably, due to its very low intensity.

§6.3 Nd-doped Scandia Waveguides

As a next step towards a waveguide laser neodymium-doped scandia films have been produced[1]. The spectroscopic and waveguiding experiments with two Nd-doped waveguiding films discussed in this section have been performed in a close cooperation with A. Kahn and are also discussed in his diploma thesis [Kah05]. The results presented in this section are also partly published in [Kuz06]

A 3 µm thick $Nd:Sc_2O_3$ film was grown using the older set-up with small aperture scanning mirror (see section 4.2). The concentration of the Nd^{3+}-

---

[1] W10 and W12 (appendix A).

dopant was 0.2 mol.%. The deposition parameters were as follows: the repetition rate of the excimer laser was 37 Hz, the radiation density on the ceramic target was 4 J·cm^{-2}, the target-substrate distance was 8 cm. During the deposition the substrate was heated up to 700°C. The background gas in the deposition chamber was molecular oxygen at the pressure of 3.3×10^{-3} mbar. The achieved deposition rate was 0.0033 nm/pulse.

The substrate was a 10×10×0.5 mm (0001)-oriented sapphire (α-Al_2O_3) polished at both sides with epitaxial quality. A 1.5 µm Al_2O_3 superstrate was deposited on top of the Nd:Sc_2O_3 film under the same conditions. This was made, in order to reduce scattering at the film-to-air interface and to make the refractive index profile of the waveguide more symmetric. The superstrate also served as a mechanical protection during the subsequent end face polishing process.

Another Nd:Sc_2O_3 film was deposited using the more recent set-up with large aperture mirror (section 4.2). This time considerably higher ablation rates of 0.024 nm/pulse were achieved. The neodymium concentration was the same as in the first film (0.2 mol.%) and again a sapphire substrate was used. The deposition took place under the following conditions: the repetition rate was 27 Hz, fluence on the target 2.5 J·cm^{-2}, oxygen pressure in the deposition chamber was 2×10^{-3} mbar. The film was 10 µm thick. Again an Al_2O_3 superstrate with a thickness of 5 µm was deposited on top.

Up to now this is the thickest sesquioxide PLD-film reported. The thickness in the tens of micrometers range is not very typical for pulsed-laser-deposited films. Thicker PLD-films have been reported only for Nd:GGG on YAG [Gri04b] (up to 135 µm) and Ti:Al_2O_3 on α-Al_2O_3 (12 µm) [And97].

6.3.1 Optical Spectroscopy

In order to evaluate the spectroscopic properties of the deposited films, emission and excitation spectra have been recorded using a Ti:Sapphire laser as the excitation source (see section 3.4 for the set-up description).

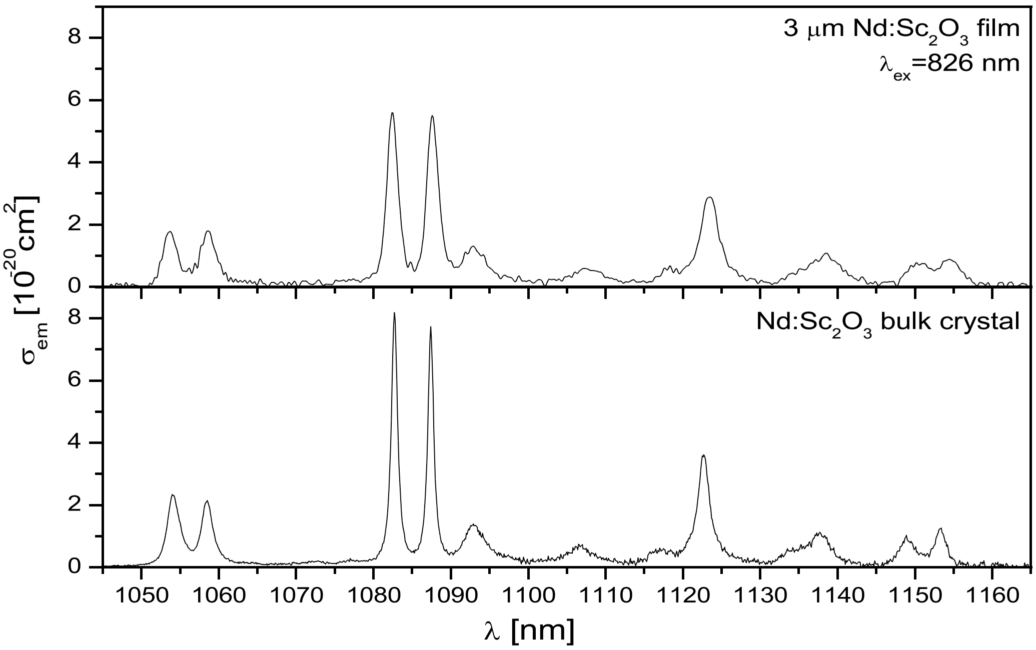

Figure 6.7: Emission cross-section spectra of the 3 μm Nd(0.2%):Sc_2O_3 PLD-film (above) and of the Nd(0.15%):Sc_2O_3 bulk crystal [For99] (below).

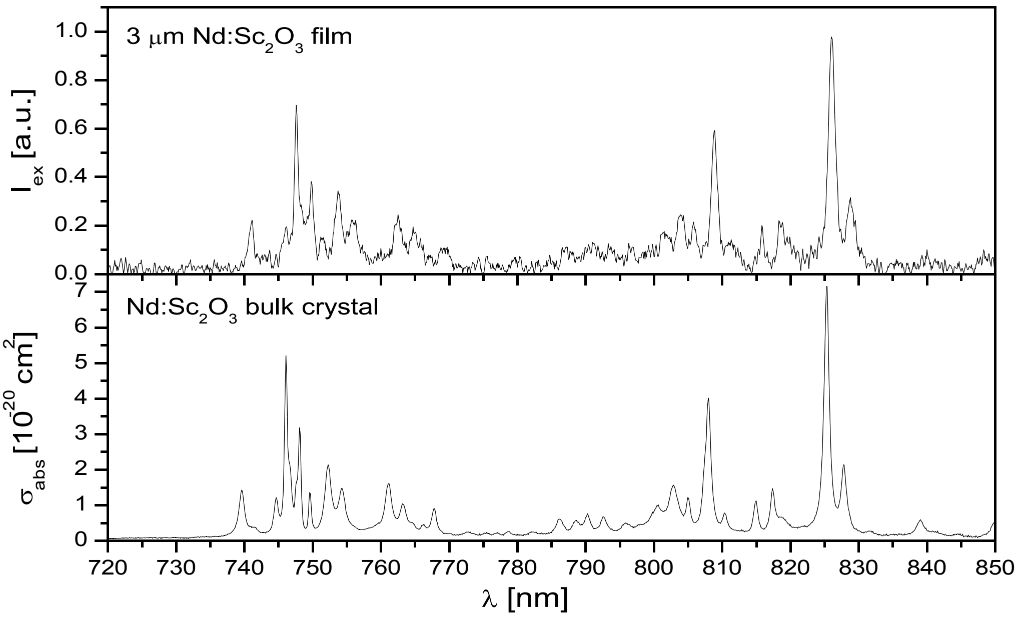

Figure 6.8: Excitation spectrum of the 3 μm Nd(0.2%):Sc_2O_3 PLD-film (above). Absorption cross-section spectrum of the Nd(0.15%):Sc_2O_3 bulk crystal [For99] (below).

Figure 6.7 shows the spectrum of the stimulated emission cross-section for the $^4F_{3/2}\rightarrow{}^4I_{11/2}(Nd^{3+})$ transition (λ_{ex}=826 nm), calculated using the Füchtbauer-Ladenburg equation 3.16 (β_{ij}=0.445 and τ=303 µs used). This transition is most often utilized for laser action in Nd-based materials, and in the case of the scandia lasing can be achieved either at 1082 nm or at 1087 nm. However laser operation was also demonstrated for the $^4F_{3/2}\rightarrow{}^4I_{9/2}$ transition at 966 nm and for the $^4F_{3/2}\rightarrow{}^4I_{13/2}$ transition at 1486 nm [For99, For99a].

The emission spectrum of the Nd:Sc_2O_3 film resembles the one of the bulk crystal closely. However, some broadening is observed, which leads to the fact, that the peak cross-section values are only about 68% of the corresponding bulk values.

It was not possible to measure an absorption spectrum of Nd-dopants by conventional methods. The signal was too weak due to the quite low Nd^{3+} concentration in the film. Therefore the excitation spectrum (λ_{em}=1082 nm) in the range of 720-850 nm has been measured for the 3 µm thick Nd:Sc_2O_3 film (figure 6.8), in order to estimate the best wavelength for pumping. The 826 nm line is the most beneficial and could be used for pumping with a Ti:Sapphire laser, but also the 808 nm line, where commercial laser diodes are available, can be utilized. The spectra for the 10 µm Nd:Sc_2O_3 PLD-film are almost identical to the ones presented in figures 6.7 and 6.8 for the 3 µm Nd:Sc_2O_3 film.

6.3.2 Lifetime Measurements

The luminescence decay curves for the $^4F_{3/2}\rightarrow{}^4I_{9/2}$ transition (966 nm) of Nd^{3+} in the 3 µm Nd:Sc_2O_3 film and in the ceramic target used as a reference are presented in figure 6.9. The excitation wavelength was 826 nm. The measurements have been done at the set-up described in section 3.4. It can be seen that the decay has a nonexponential behavior. This is caused by nonlinear processes (up-conversion, cross-relaxation and energy migration) taking place in spite of the low neodymium concentration. A similar effect was observed by Fornasiero for neodymium-doped bulk sesquioxide crystals [For99]. Therefore only the later part of the decay curve ($t\rightarrow\infty$) was used to estimate the exponential

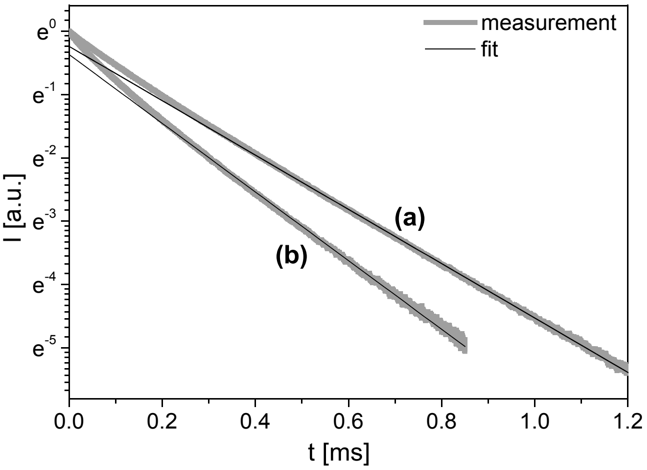

Figure 6.9: Luminescence decay curves for the $^4F_{3/2} \rightarrow ^4I_{9/2}$ transition of Nd^{3+} for: (a) Sc_2O_3 ceramic target; (b) 3 µm Sc_2O_3 PLD-film.

component of the decay. The fluorescence decay lifetime of the $^4F_{3/2}(Nd^{3+})$ multiplet was measured to be 180 µs for the $Nd:Sc_2O_3$ film and 230 µs for the ceramic target. High lattice defect density and structure irregularities in the film are believed to cause faster nonradiative depopulation of the $^4F_{3/2}$ excited state of Nd^{3+}-ions in the film. Only few reports of lifetime measurements for $Nd:Sc_2O_3$ can be found in the literature for comparison: 260 µs (0.5% Nd) [Zve67], 224 µs (0.7% Nd) [For99a], 285 µs and 303 µs (0.12% Nd) [For99]. In the latter reference the first value results from the fit of the fluorescence decay curve ($t \rightarrow \infty$) and the second value was obtained by determining the integral emission cross-section of the transition. This latter value has been used as the radiative decay rate in equation 3.16 for calculations of the emission cross-sections. Strong dependence on the neodymium concentration can be noted. This confirms, that processes other than spontaneous emission noticeably affect the luminescence decay of the $^4F_{3/2}$ multiplet of the Nd^{3+}-ion.

The reduced lifetime values observed in the $Nd:Sc_2O_3$ PLD-films in comparison with bulk crystal can result in a slightly higher threshold for continuous-wave laser operation.

6.3.3 Waveguiding Experiments

Experimental Setup

The waveguiding experimental set-up has been modified in comparison with the one used for experiments with the $Eu:Y_2O_3$ film (figure 6.10). A

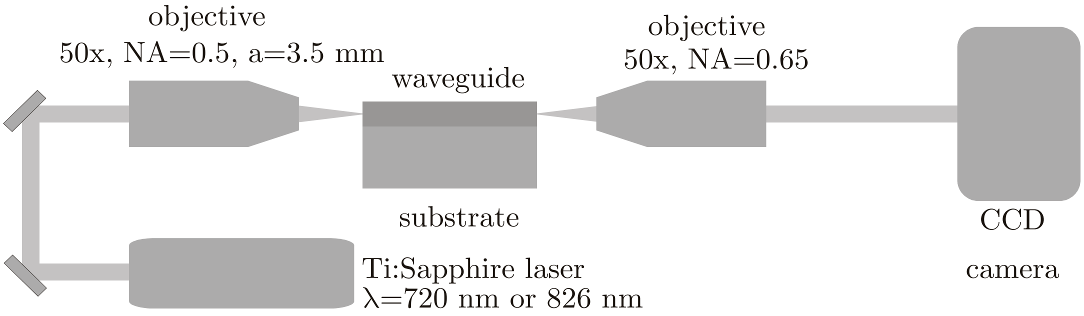

Figure 6.10: Scheme of set-up used for waveguiding experiments with Nd:Sc_2O_3 PLD-films.

Ti:Sapphire laser either at 720 nm or at 826 nm, where Nd^{3+}-ions can be excited, has been utilized for waveguiding experiments. Instead of the triplet a special microscope objective with relatively large working distance of 3.5 mm was used to couple the laser emission in. Large working distance allows a dielectric mirror to be placed directly at the film end face for laser experiments. Another microscope objective and a CCD camera have been used to detect the light coupled out of the end face of the sample.

Results

Due to the fact that the refractive index of scandia is larger than that of sapphire ($n_{Al2O3,od}$=1.763, $n_{Al2O3,ext}$=1.754, n_{Sc2O3}=1.981 at 720 nm) it was possible to achieve guiding of light in both 3 µm and 10 µm PLD-films.

The images of the end faces recorded with the camera are presented in figure 6.11. The waveguides can be easily recognized. However one can see, that, like in the case of the waveguiding Eu:Y_2O_3 film discussed above, the light distribution is quite inhomogeneous and resembles the speckle pattern, observed when coherent light is scattered at a rough surface. Thus, this phenomenon is interpreted as the interference of light scattered either at the crystallites boundaries inside the film or at the film surface. According to equation 6.12 up to 7 TE-modes are expected to be guided in the 3 µm Sc_2O_3 film and up to 24 TE-modes in the 10 µm thick film (at 720 nm). Multi-mode guiding has also been observed experimentally. For the 3 µm film the intensity profile deviates

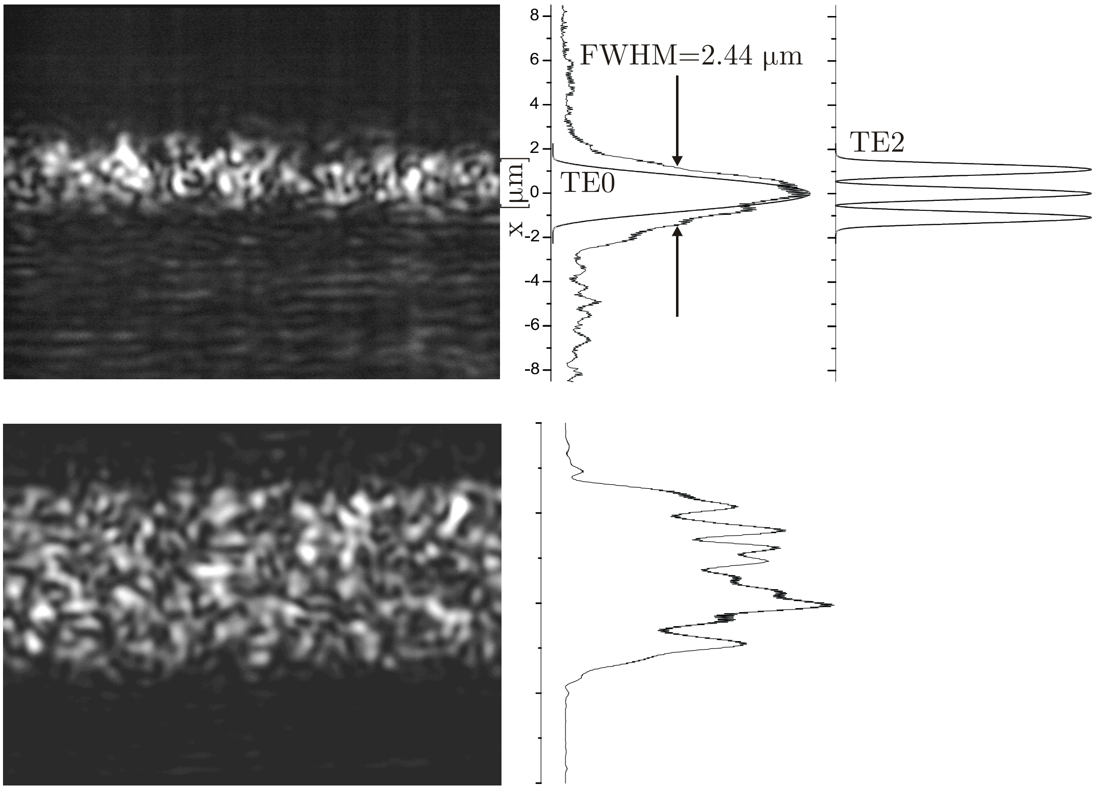

Figure 6.11: Image of the waveguiding 3 µm PLD-film and the integrated intensity profile compared to calculated TE0 and TE2 mode profiles (above). Image of the waveguiding 10 µm film and the integrated intensity profile (below) (approximately the same magnification as the image above, exact scale not determined).

substantially from the calculated TE0 mode, since multiple modes are excited. For the 10 µm film the effect is even more pronounced.

Luminescence of the neodymium dopant has been observed with the same CCD-camera from the side of the sample, when the Ti:Sapphire laser was tuned to the absorption line of Nd^{3+} (826 nm). An edge-filter was placed in front of the camera in order to block the scattered pump light. The emission was not detected, if the pump wavelength was detuned from the absorption peak. This confirms, that guiding of the Nd^{3+} emission and not residual pump was observed.

In order to achieve laser operation, mirrors highly reflecting at the Nd^{3+} emission wavelength have been placed at the two end faces of the waveguides. However, no laser emission was observed. Presumably, very high losses in the waveguides (as discussed below) hinder the laser operation. Thus, further optimization of the deposition process is still required to fabricate films with lower propagation losses.

6.3.4 Propagation Losses

In order for the laser operation to be achieved in a waveguide laser, the gain in the waveguide must compensate for losses, which can be separated into two groups: (a) coupling losses, which result from the finite transmission coefficient of resonator mirrors and imperfect coupling from and into the waveguide; (b) propagations losses, resulting from scattering and absorption in the medium itself. Whereas the former depends mostly on the laser cavity design and geometry, the latter to a greater extent depends on the properties of the waveguide itself. Thus, the propagation loss of the waveguide is one of the most important parameters, if laser operation is considered.

Since Sc_2O_3 is fully transparent in the visible and near infrared spectral range, the absorption for the $Nd:Sc_2O_3$ waveguides discussed here is determined only by absorption of the dopant and therefore easy to control. The scattering losses on the contrary are difficult to measure and their origin is often not obvious.

The standard technique for measurements of propagation losses in fibers is to shorten the fiber step-by-step and to measure the intensity of the transmitted light for each fiber length. However, since this is a destructive technique, it has not found wide application in the waveguide field. In case laser operation in the waveguide is achieved, the Findlay-Clay method [Fin66] based on the analysis of lasing characteristics can be applied. In the case of non-lasing waveguides the usual way is to observe the intensity of the guided or scattered light along the propagation direction.

For both 3 μm and 10 μm thick $Nd:Sc_2O_3$ waveguides the scattering propagation losses have been determined in the following way: the radiation of a Ti:Sapphire laser was coupled into the waveguide (λ=826 nm) and the decrease of the excited Nd^{3+} luminescence along the sample was analyzed. Thus, the emission of the Nd-dopant served as a probe for the intensity of the light propagating in the waveguide. The emission wavelength of the Ti:Sapphire laser was changed and the measurements have been performed at a number of different absorption peaks of Nd^{3+}. In this way it was possible to separate the varying intensity decay due to Nd^{3+} absorption from that due to scattering, which was considered constant with regard to the wavelength. The light propagation losses of 19.5 $dB{\cdot}cm^{-1}$ and 12 $dB{\cdot}cm^{-1}$ were estimated for 3 µm and 10 µm thick films, respectively. A thorough description of the measurements and the technique and can be found in [Kah05].

Analysis of Reflectometer Signal

In contrast to classical lasers, where the light is propagating through the volume medium, in a waveguide the light is being constantly reflected from the interfaces of the waveguide with the surrounding media. Thus, both scattering in the volume and at the surface of the guiding layer can play an important role. Some estimations have been made analyzing the behavior of the reflectometer signal, which was recorded during the deposition of the 10 µm $Nd:Sc_2O_3$ film. The details on the principles of reflectometry and its experimental realization can be found in sections 3.2 and 4.2.

Figure 6.12a presents the simulated reflectometer signal for the case of a lossless medium, as it is described by equation 3.12. The volume losses can be introduced by assuming a complex refractive index for the film material. As the thickness of the film increases, the intensity of all higher order reflections decreases, the signal oscillation becomes less pronounced and the intensity converges to the value defined by the first reflection from the front surface of the film (figure 6.12b). Figure 6.12c presents the case, when the front surface of the film is assumed to become less smooth (stronger scattering) with the increasing thickness of the film. The scattering was introduced through the decrease of both reflection and transmission coefficients at the front surface of the film. Equation 3.9 was used to calculate the resulting reflected intensity, since equation 3.12 assumes the sum of reflection and transmission coefficients to be unity,

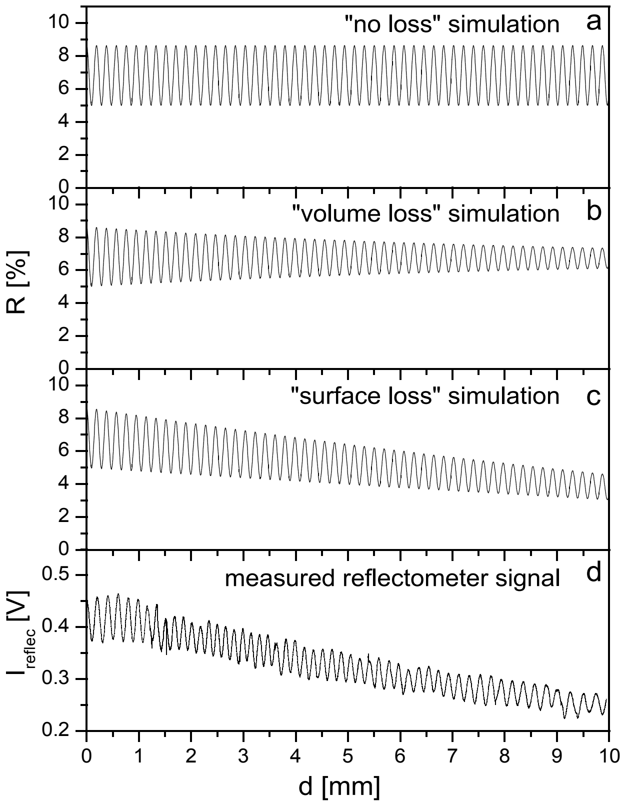

Figure 6.12: Simulated reflectometer signal curves for: (a) "no losses" model; (b) scattering in film volume; (c) scattering at film surface. (d) Reflectometer signal recorded experimentally during deposition of the 10 µm Nd:Sc_2O_3 PLD-film.

which is not the case here. The first five terms of the infinite series were used, which was proven to provide sufficient precision. In this model the reflection and transmission coefficients were assumed to decrease linearly with the increasing film thickness. The model with the surface-related losses was found to reflect the behavior of the experimental result (figure 6.12d) more adequately. A similar reflectometer signal behavior was observed during the deposition of the 3 µm waveguide.

Thus, presumably the scattering effects at the surface seem to play the major role for the Nd:Sc_2O_3 waveguides discussed here. A possible reason is scattering at the crystallite boundaries, however measurements in the integrating sphere (section 3.3) have not revealed any dependency of the scattered light intensity on the crystallite dimensions. It is believed, that droplets and particulates at the surface of the film can cause the scattering of the light. Apart from the deposition parameters, like laser fluence or gas pressure, which can influence the particulate density, one of the critical points can be the use of ceramic targets for the deposition. Since a ceramic is not completely dense, particulates in the micrometer range can be torn out during the ablation and adhere at the substrate without being evaporated. Even if a bulk crystal is used as the target, additional steps, like surface polishing, can further reduce the particulate density [Lan05]. The problem of particulates in PLD-process is also discussed by Barrington in his thesis [Bar01].

§6.4 Structuring Experiments

The planar waveguide geometry discussed above can be suitable for the implementation of a single light emitter, however, in the domain of integrated optics more control over the light prorogation is required. Channel or rib waveguide geometry can satisfy this demands. Up to now only few reports on structuring of crystalline oxide materials can be found in the literature. For example structures in sapphire PLD-films produced by Ar^+-beam etching [Gri04c] or in sapphire crystals produced by combination of He^+-beam/wet-etching [Cru03] have been demonstrated. In this section two approaches to the fabrication of such structures in sesquioxide films are presented: lift-off technique and milling with an Ar^+-beam.

6.4.1 Lift-off Technique

Figure 6.13 schematically presents the steps of fabrication of stripes on a sapphire substrate with the lift-off technique. A photoresist mask was produced by the common photolithography process at INSTITUT FÜR ANGEWANDE PHYSIK, UNIVERSITÄT HAMBURG. After exposure through a metallic mask and developing, photoresist was removed from ~80 µm broad stripe-shaped areas. Two photoresist layers with different solubilities were utilized in order to obtain edges like presented in figure 6.13b. Thus, the material was deposited with some spacing to the photoresist. The thickness of the lower mask layer was 350 nm. A 330 nm $Eu:Y_2O_3$ PLD-film was deposited subsequently over the photoresist mask. The deposition conditions were as follows: 1×10^{-2} mbar oxygen atmosphere, the laser fluence 2.5 $J\cdot cm^{-2}$, the target-substrate distance 9.5 cm. The substrate was not heated, since the photoresist mask could have been destroyed otherwise. After the deposition of the film the substrate was placed into a solvent for 24 hours in order to remove the remaining photoresist and simultaneously the yttria layer deposited on

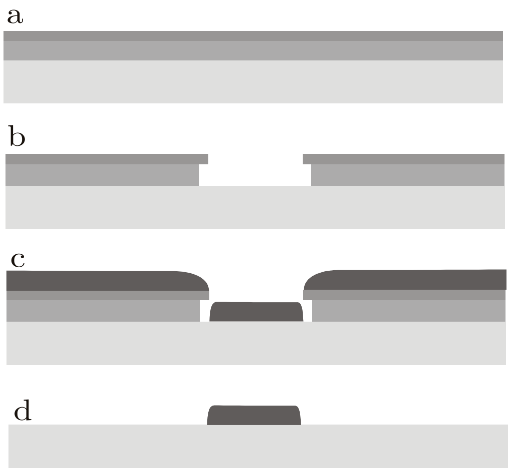

Figure 6.13: Scheme of the lift-off technique: (a) two layers of photoresist are deposited; (b) photoresist is exposed through a mask and developed; (c) Y_2O_3 is deposited by PLD process; (d) photoresist is removed together with Y_2O_3 on it.

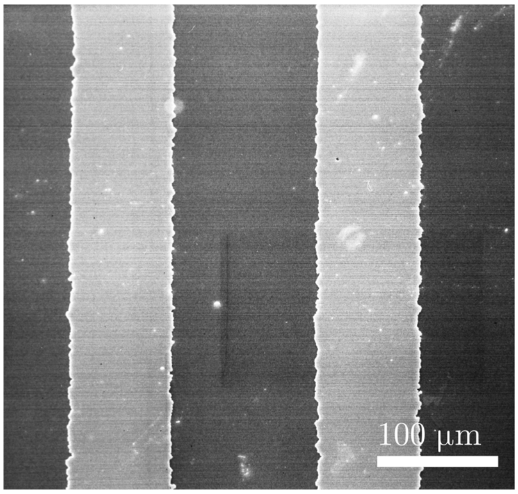

Figure 6.15: SEM image of the Eu:Y_2O_3 stripes on sapphire substrate produced by the lift-off technique.

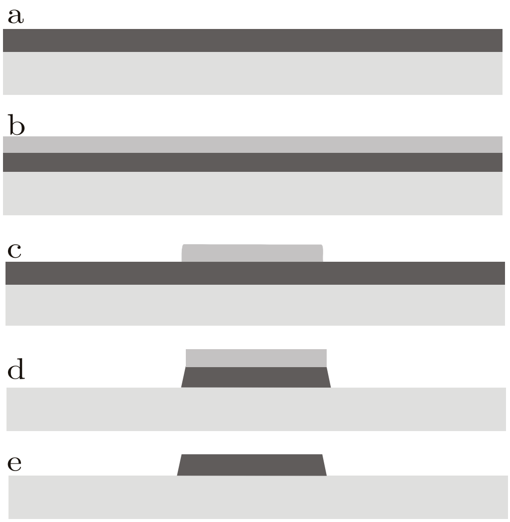

Figure 6.14: Scheme of the Ar^+-beam etching process: (a) Y_2O_3 PLD-film is deposited, (b) photoresist is deposited on top; (c) photoresist is exposed through a mask and developed; (d) Y_2O_3 is etched with Ar^+-beam; (e) photoresist is removed.

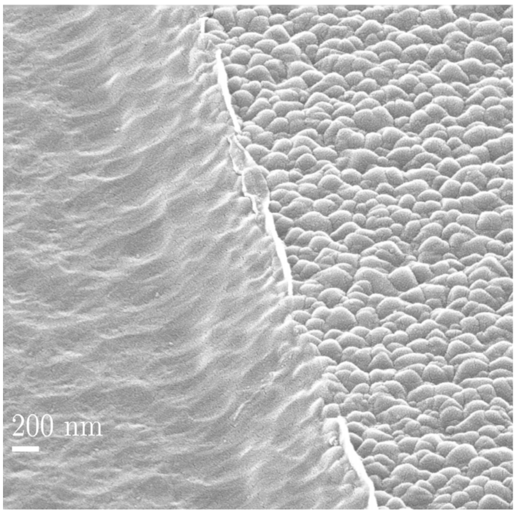

Figure 6.16: SEM image of step in the Eu:Y_2O_3 PLD-film produced by Ar^+-beam etching.

top. An ultrasound assistance was employed to accelerate the process. Subsequently, scanning electron microscopy (SEM) of the sample was performed at Fachhochschule Wedel. The SEM-image is presented in figure 6.15. One can see that yttria film deposited in the photoresist-free areas remained on the substrate and photoresist with the yttria film on top was fully removed. The uneven edges of the yttria stripes result from the old slightly damaged mask taken for the first experiments. The irregular edges were observed in the mask itself, before the PLD-film was deposited.

6.4.2 Ion-Beam Etching

Another approach to produce channel waveguides is to structure the already deposited film. A rib-waveguide geometry (figure 6.1c) can also be produced in the same way, if a superstrate is structured instead of the guiding film itself. Ar^+-beam etching experiments and SEM-imaging presented here were performed at Forschungszentrum Jülich. The scheme of the etching process is presented in figure 6.14. First a 2 µm thick $Eu{:}Y_2O_3$ film was deposited on a sapphire substrate. The deposition parameters were the same as for the deposition with the photoresist mask discussed above. In this case also a photolithography technique was used in order to produce a photoresist mask above the yttria film. Narrow stripes of the photoresist in the range 2-10 µm did not adhere to the substrate and detached during the developing stage. Thus 130 µm broad stripes were produced. Photoresist AZ5206 together with HMDS (Hexamethyl-disilazane) as an adhesion promoter was utilized. Afterwards Ar^+-beam milling was employed to remove Y_2O_3 not covered by the mask. The etching rate was 10 nm/min, a step with the height of 400 nm was produced. The SEM-image of the edge of the fabricated step in the yttria films is presented in figure 6.16. One can see, that the etching process did not result in a sharp, but rather an oblique step.

§6.5 Summary and Discussion

In this chapter spectroscopic and waveguiding properties of $Eu{:}Y_2O_3$ and $Nd{:}Sc_2O_3$ PLD-films have been discussed. Waveguiding has been demonstrated in a 1.2 µm thick Eu:Y_2O_3 film as well as in 3 µm and 10 µm thick Nd:Sc_2O_3 films. The 10 µm film is up to now the thickest sesquioxide film produced by pulsed laser deposition.

Spectroscopic investigations have revealed, that emission and excitation spectra of the rare-earth (RE) dopants (Eu^{3+}, Nd^{3+}) in PLD sesquioxide films resemble closely the corresponding bulk crystal spectra. Some deviations are observed in the UV-region (charge-transfer absorption band expands to longer wavelengths). Irregularities of the crystalline lattice in the PLD-films lead to slight inhomogeneous broadening of the RE-ion spectra and, consequently, to lower peak cross-sections. For Nd:Sc_2O_3 peak emission cross-sections have been estimated to decrease by about 30% with respect to the bulk. The fluorescence decay lifetime of $^4F_{3/2}(Nd^{3+})$ in a Sc_2O_3 film is 180 µs, which is about 60% compared to the value for a bulk crystal found in the literature. The reduced fluorescence lifetime and peak emission cross-sections can cause somewhat higher threshold for laser operation. However the effect is not dramatic and spectroscopic properties of the Nd:Sc_2O_3 PLD-films look promising for the realization of a waveguide laser or amplifier.

The propagation losses for Nd:Sc_2O_3 films have been analyzed. For 3 µm and for 10 µm thick films the propagation losses are 19.5 $dB\cdot cm^{-1}$ and 12 $dB\cdot cm^{-1}$, respectively. This is much higher than the loss values obtained for other neodymium-doped waveguides (e.g. [Gri04a]). It is believed that particulates at the film surface could result in scattering of the propagating light.

First experiments on structuring the deposited PLD-film have been performed employing the lift-off technique and Ar^+-beam etching. Structuring of the deposited films is required for the realization of two-dimensional guiding, in order to be able to control the propagation of light more precisely. Further research is still required before a channel or rib waveguide can be produced.

Chapter 7. Ytterbium-Doped PLD-Films

In this chapter spectroscopic properties of ytterbium-doped PLD-films are discussed. These films are considered in the context of their possible application as an active medium for thin disk lasers. The first section introduces the concept of the thin disk laser and discusses the advantages of Yb-doped materials. subsequently the experimental results are presented, which include investigations of ytterbia (Yb_2O_3), ytterbium-doped scandia ($Yb:Sc_2O_3$) and lutetia ($Yb:Lu_2O_3$), as well as an ytterbium-doped yttrium-aluminum garnet (Yb:YAG) films. Also possible application of PLD for fabrication of microcavities is discussed.

The employed experimental techniques include emission and excitation spectroscopy and fluorescence lifetime measurements. The knowledge of excitation and emission spectra is necessary for material, which is supposed to be utilized as an active medium. Since they help to choose the wavelength most favourable for pumping and estimate the possible lasing wavelength. Additionally, the crystalline quality of the films can be evaluated through the analysis of the spectrum broadening. Since peak emission cross-sections and the fluorescence lifetime influence the threshold for the laser operation, it is quite important to estimate them for a possible laser material. The quantum efficiency of the dopant emission can also be estimated through the fluorescence lifetime.

§7.1 Introduction

7.1.1 Thin Disk Laser Concept

Historically, the domain of high power lasers used for material processing was dominated by gas lasers, and in particular by CO_2-lasers. It is simple and robust, however its emission in the far infrared region (10.6 μm)

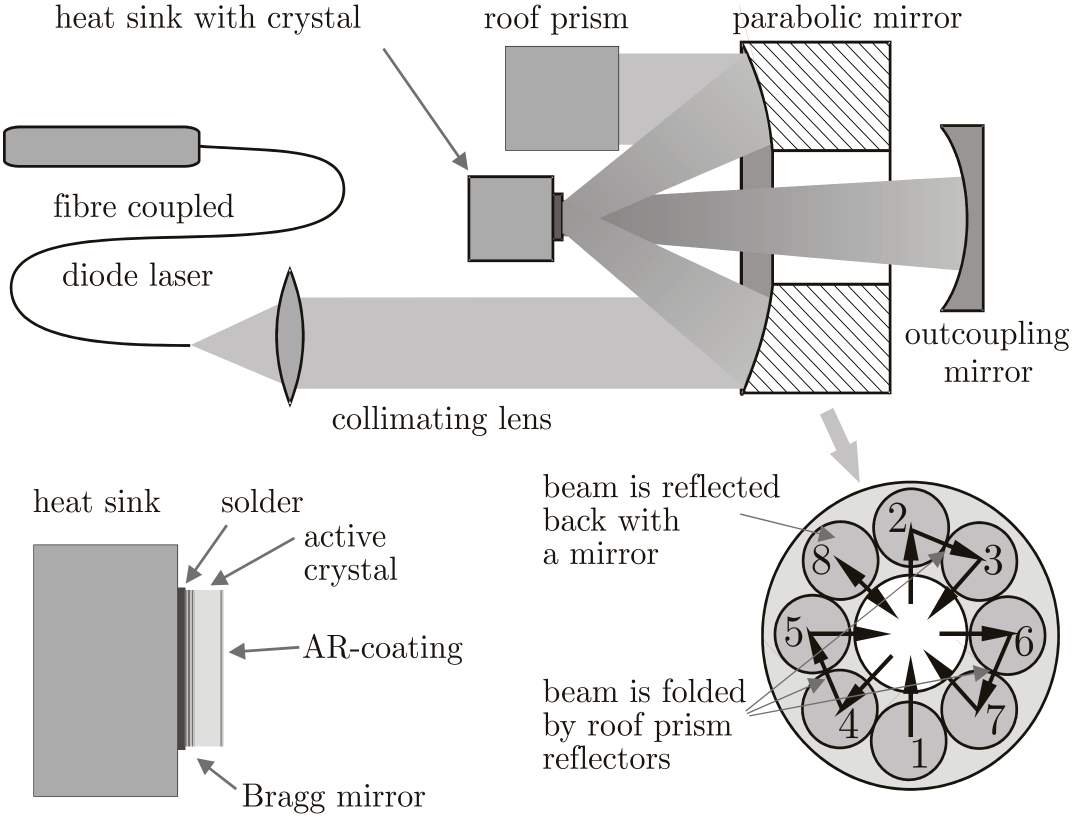

Figure 7.1: Thin disk laser set-up (above). Laser head design (below, left). Pump beam reflections scheme for 16x passes – 8x forward and 8x backward (below, right).

makes it difficult to transfer and handle the radiation. Later, semiconductor laser bars have been stacked to achieve power in kW range. But the very low beam quality hinders their application in such fields as, for example, cutting and drilling, were precise focusing is necessary. Solid-state lasers are also employed, but they are usually more complex and expensive. However, after the invention of the thin disk laser set-up [Gie94], solid-state lasers have received an increased attention as possible candidates for high-power applications. This design has addressed the problem of the heat dissipation, which is one of the main challenges in fabrication of a high-power solid-state laser.

A scheme of the thin disk laser set-up is presented in figure 7.1. The main idea of the concept is achieve the heat flow parallel to the light propagation direction. This eliminates the temperature gradient in the lateral direction, accordingly eliminating the thermal lens effect, which often limits the achievable output of a solid-state laser.

Additionally, thin active crystals (disks) and large laser mode diameters are utilized, thus even further improving the heat flow and the reducing thermal load. Nowadays, disks with the thickness down to 100 µm are used. However, this raises the problem of low absorption of the pump light in the thin active medium. The typically used solution is to fold the pump beam and make it pass the crystal several times (as presented in figure 7.1). Sometimes also side pumping is employed. In this case the light of the laser diode is focused into the active crystal, so that it is guided inside of the crystal due to the total internal reflection.

Why Pulsed Laser Deposition?

The typical way of fabrication of active media for a thin disk laser is to cut a disk out of a grown bulk crystal and polish it to the necessary thickness and quality. Sometimes it is subsequently bonded onto an undoped substrate for mechanical stability. On the one side the high-reflective dielectric Bragg mirror (HR) for both pump and laser wavelengths is deposited, the other side is usually anti-reflex (AR) coated. Afterwards the mirrored side of the crystal is soldered onto a heat sink.

However, some difficulties may arise during fabrication and handling of such thin crystals (a few 100 µm), as well as during bonding them onto a heat sink. An alternative technique is a deposition of the active material directly onto an undoped substrate. Following this route, Ubizskii *et al.* produced highly Yb-doped epitaxial YAG films by liquid-phase epitaxy (LPE), which subsequently showed continuous-wave laser action in a thin disk set-up [Ubi04]. However, unidentified absorption bands and lifetime reduction have been observed in some films, possibly due to contamination from the flux. The pulsed laser deposition can be an even more favorable technique. In principle, it allows fabrication of high quality crystalline films with high peak emission and absorption cross-sections of dopants. Another important quality of PLD is that, due to the nature of the process, it minimizes the possibility of contamination of the deposited films. In the contrast to LPE, where impurities can be incorporated from the flux, or to classical crystal growth methods, where impurities are present in the crucible material, in the PLD process the material is transferred directly from a target onto a substrate in vacuum or suitable atmosphere. The only limiting factor in this case is the purity of the source materials. As it will be discussed below impurities are an important issue for highly Yb-doped materials.

Alternating the materials used for evaporation, also the dielectric coatings (Bragg mirror and anti-reflection coating) could be fabricated by pulsed laser deposition. Pulsed-laser-deposited films typically reveal the crystalline character with the density approaching that of a bulk crystal. This ensures high refractive index and mechanical stability of the films. The fact, that the active media for thin disk laser together with all coatings can be produced in one technological process, makes pulsed laser deposition a very interesting technique for this application. Up to now, no research in this area have been noticed. All investigations of active PLD-films were carried out with respect to their possible applications as active media for waveguide lasers or amplifiers. The PLD-films reported in the literature typically have the thickness of a few micrometers, which is not enough for thin disk laser applications. However, in the course of these work a Nd:Sc_2O_3 waveguiding PLD-film with the thickness of 10 µm have been successfully fabricated (see section 6.3). Also some examples of thick PLD-films can be found in the literature: up to 12 µm Ti:Sapphire [And97a, And97b], up to 135 µm Nd:GGG [Gri04b]. Thus, the film thicknesses, that are necessary for a thin disk laser, seems to be achievable with the pulsed laser deposition.

7.1.2 Microcavities

Another possible application for pulsed-laser-deposited, layered structures could be fabrication of compact devices such as, for example, Fabri-Perot microcavities. A microcavity consists of two Bragg mirrors (interchanging high and low refractive index layers with the optical thickness of a quarter design wavelength) and a cavity with optical thickness multiple to a half of the design wavelength. Otherwise a microcavity can be considered a one-dimensional photonic crystal (periodic structure) with a defect (cavity). When light is incident on such a structure, a standing light wave is built up inside of the cavity, due to multiple interference of the waves traveling in both directions. The intensity inside of the cavity can considerably exceed the intensity of the incident light. These two effects, localization of electric fiend due to the standing wave, and intensity gain can be utilized if strong field-matter interaction is desired, as, for example, for lasers light amplifiers or for nonlinear optical devices.

A model of such a microcavity, designed for 1 μm wavelength, is presented in figure . Each Bragg mirror consists of four pairs of high/low refractive index materials having refractive indices of 1.96 and 1.53 (scandia and quartz(n_o)). The thicknesses are 127 nm and 163 nm for high and low

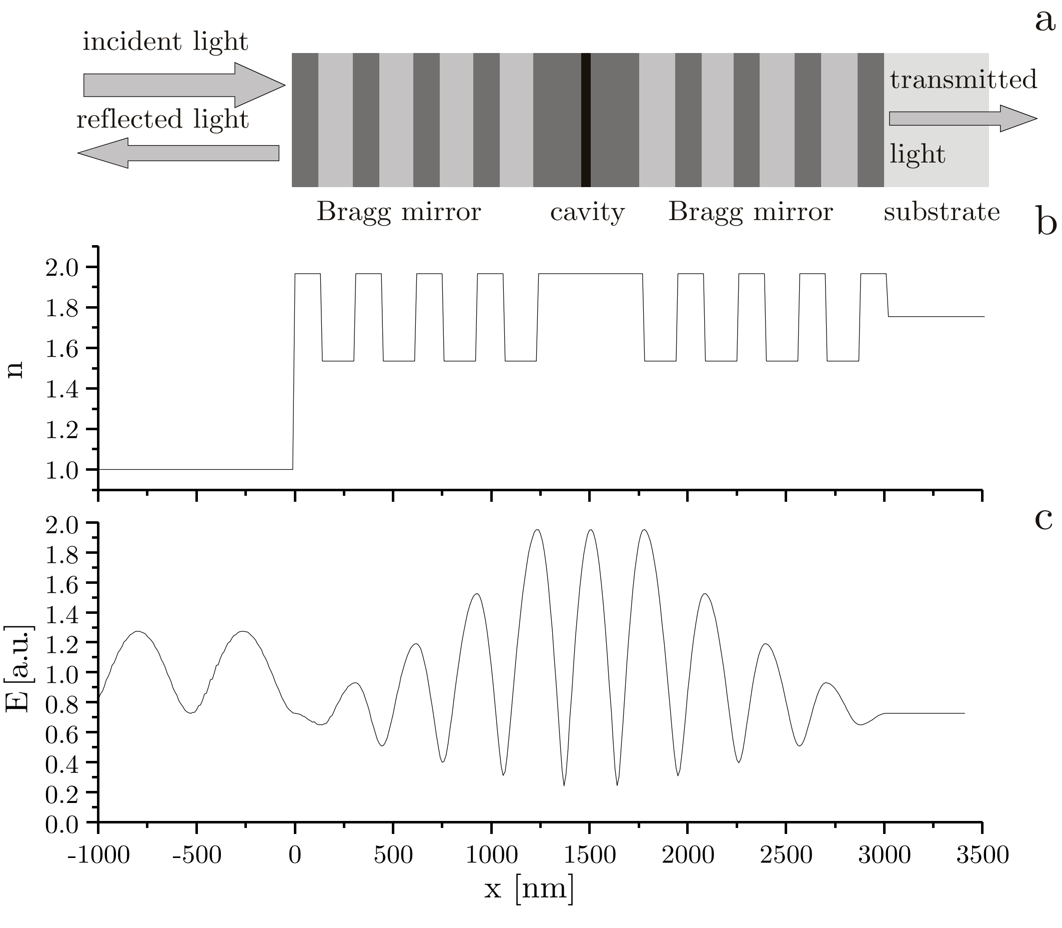

Figure 7.2: (a) model of a microcavity, *dark gray* – high refractive index material, *light gray* – low refractive index material; *black* – active medium should be placed here; (b) refractive index profile; (c) strength of electric field, normalized to the incident light.

index layers, respectively. Scandia has also been taken as the cavity material. The thickness of the cavity is 508 nm, thus the optical length corresponds to one design wavelength. The distribution of the amplitude of the electric field E (figure c) has been calculated using the transfer-matrix method (TMM). It is normalized to the amplitude of the incident light. The varying amplitude in the region to the left of the structure is caused by the interference with the reflected light. For the presented case, the field strength in the cavity is about two times higher than that of the incident light. For the intensity the effect is larger, since it is proportional to the square of the electrical field. In order to achieve stronger effect, the reflectivity of the mirrors should be improved. Either more pairs of high/low index layers or materials with higher refractive index contrast should be used. In the discussed case reflectivity of both Bragg mirrors is only about 70% at the design wavelength.

The first theoretical investigations of microcavity effect was done by Purcell [Pur46]. But the first microchip laser was demonstrated much later by De Martini [DeM88]. Details on microcavity effects and microcavity lasers can be found for example in a review by G. Björk [Bjö96]. In recent time also enhancement of nonlinear light-matter interaction in microcavities received much attention, e.g. Bosco *et al.* [Bos04] have experimentally demonstrated second harmonic generation (SHG) in a one-dimensional AlGaAs/Al_2O_3 photonic structure. The microcavity effect is also utilized in vertical cavity semiconductor lasers [Tro04].

However, further research is still required in order to achieve the accuracy in the control of the pulsed laser deposition process, which is necessary to deposit such complex structures.

7.1.3 Ytterbium-Doped Materials

Originally, Nd-doped materials have been widely used as an active medium for high-power lasers. The Nd^{3+}-ion has high absorption and emission cross-sections in many materials and laser operation with its four-level scheme for the $^4F_{3/2} \rightarrow {}^4I_{11/2}$ transition is easy to realize. Also suitable high-power laser diodes as pump source are commercially available. All this make Nd-doped materials a favorable choice.

However, the invention of the thin disk laser set-up stimulated an increasing interest to the Yb-doped oxide materials. Due to a smaller quantum defect compared to the widely used Nd-doped materials, the heat dissipation is reduced, thus even further minimizing thermally induced problems. The very simple energy level structure of the Yb^{3+}-ion also eliminates the possibility of the depopulation of the upper laser level due to cross-relaxation and up-conversion processes and nonradiative decay. This is an important advantage at high doping concentrations and pump rates used in a thin disk laser. Due to relatively broad emission lines, Yb-doped materials are also suitable for mode-locked operation regimes.

The most widely used host material for Yb^{3+}-ions is yttrium aluminum garnet (YAG), which is also a classical host material for the Nd^{3+}-dopant. This is due to favorable spectroscopic properties of Yb:YAG, developed growth technology of YAG crystals, and low cost of source materials. It is mechanically stable and reveals high thermal conductivity. For example, a Yb:YAG thin disk laser with output power of 650 W using one disk or 1070 W using four disks has been demonstrated [Ste00]. Also a mode-locked Yb:YAG thin disk laser has been used recently to demonstrate a multi-watt RGB laser source [Bru04].

Apart from YAG, the sesquioxides (e.g. Sc_2O_3, Y_2O_3, Lu_2O_3) are very promising host materials for high-power laser applications [Pet02b]. Their thermal conductivity is even higher than that of YAG (see table 2.1). Also very high absorption and emission cross-sections of trivalent rare-earth ions in these materials make them an interesting alternative. Effective mode-locked laser operation has been also demonstrated recently using $Yb:Sc_2O_3$ [Klo04] and $Yb:Lu_2O_3$ [Grib04] single crystals. Details on the spectroscopic and lasing properties of Yb-doped sesquioxides can be found in [Mix99] and [Pet01].

Lutetia is possibly the most interesting among the sesquioxides as a host material for Yb^{3+}-ions. Lu^{3+} and Yb^{3+} ions in the sixfold coordination have almost the same effective radius of 0.86 Å and 0.87 Å, respectively, and, consequently, lutetia and ytterbia have close lattice constants (10.391 Å and 10.439 Å). Thus, lutetia can be doped with any amount of ytterbium without distorting the crystal structure. Intrinsically high thermal conductivity of lutetia does not degrade at the high doping levels, since the lutetium and ytterbium ions have similar mass. Both qualities are especially beneficial in the case of the thin disk laser applications. Due to the difference in ionic radii of Sc^{3+} and Yb^{3+}, scandia may have some limits in accepting Yb-ions without distorting the crystal structure. But scandia is still an interesting host, since the Yb-dopant has the highest emission and absorption cross-sections in comparison with the other sesquioxides or YAG.

As it has been mentioned above, laser action at high doping concentrations of Yb^{3+} is possible due to its simple energy level structure. Effective laser operation has been demonstrated for concentrations up to 1.38×10^{21} cm^{-3} (10 mol.% Yb:YAG). Even higher concentrations are required to reduce the thickness of the active medium. However, with higher concentration causes the mean Yb-Yb distance decreases reduce and the energy migration rate increases rapidly. From the Förster-Dexter theory [För48, Dex53] the energy transfer rate $W(t)$ is given by the following expression (only electric dipole interaction is considered)

$$W(t) = \frac{3\hbar^4 c^4}{4\pi n^4} \frac{Q_A A_D}{R_{DA}^6(t)} \int \frac{f_D(E) f_A(E)}{E^4} dE \quad , \tag{7.1}$$

where Q_A is integral acceptor absorption cross-section, A_D radiative rate of donor, and $f_A(E)$ is form of the acceptor absorption line (area normalized). $f_D(E)$ is form of the donor emission line (area normalized), n refractive index, and $R_{AD}(t)$ is mean acceptor-donor distance, which can be pumping rate and time dependent. From equation 7.1 follows, that the migration rate

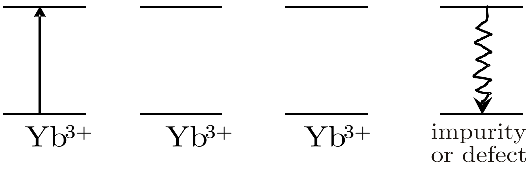

Figure 7.3: Illustration of energy migration model in highly Yb-doped materials.

increases inversely proportional to the sixth power of the interionic distance. Fast migration rates lead to the situation, when the excitation is rapidly transferred from ion to ion and can be finally transferred to an impurity or a defect (see figure 7.3), which can be radiatively or nonradiatively deexcited. It has been shown that impurities in the ppm range can cause significant quantum efficiency degradation at high Yb-concentrations [Pet05]. Degradation of the efficiency at high pumping rates in Yb:YAG crystals have been reported as well [Lar05].

§7.2 Characterization of Yb-Doped PLD-films

7.2.1 Ytterbia Films

Since the thickness of the active medium in the thin disk laser set-up is a concern, ytterbia (Yb_2O_3) can be a possible candidate. Due to the very high Yb^{3+} density, it would result in the thinest possible design for a given absorption among all Yb-doped materials.

Two series of ytterbia films with different thicknesses in the range of 20 nm – 500 nm were deposited on sapphire and quartz substrates[1]. The X-ray diffraction analysis of the films were performed in order to investigate the crystalline structure of the films. These results as well as the fabrication conditions are discussed in detail in section 5.1. The films deposited both on sapphire and on quartz substrates are crystalline and highly textured in <111>-direction. Room temperature spectroscopic measurements were performed under continuous IR excitation using a Ti:Sapphire laser and under pulsed IR excitation with an OPO. In both cases no Yb^{3+}-emission could be detected. Emission measurements of the ytterbia films under UV excitation have been performed at the SuperLumi experimental set-up. The mentioned experimental set-ups are described in section 3.4.

Figure 7.4 shows the emission spectra of the 500 nm thick Yb_2O_3 film on a quartz substrate under 220 nm excitation. The spectra reveal the well-known Yb^{3+} ($^4F_{5/2}\rightarrow{}^4F_{7/2}$) emission in the 975 nm – 990 nm spectral region

---

[1] Y01, Y02, Y04 and Y07-Y09 (appendix A).

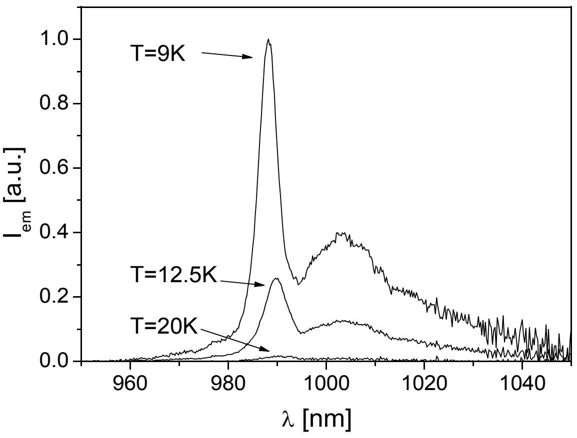

Figure 7.4: Low temperature emission spectra of the 500 nm Yb_2O_3 film on α-SiO_2 substrate under 220 nm excitation.

(zero-phonon line) at temperatures below 20 K. Above 20 K the intensity of the Yb^{3+} emission decreases very rapidly. At room temperature no emission has been detected. A similar effect has been observed also for a bulk ytterbia crystal used as a reference. The emission at the room temperature was still present in this case, but the intensity was essentially lower than at the low temperatures. This effect is attributed to the very fast energy migration due to very dense packing of ytterbium ions. However, the migration is prevented, if the temperature is low enough. The position of the energy levels of every individual atom is slightly different, due to slight inhomogeneity of the crystal structure and, consequently, the microscopic crystal field. Thus, for migration to occur, some additional energy is transmitted to or absorbed from the lattice in the form of phonons. At low temperatures the lattice phonons are not excited, so the migration is suppressed and the quantum efficiency of the luminescence increases.

A slight shift of the zero-line peak position can be noticed: 988.2 nm at 9 K, 989.6 nm at 12.5 K, and 990.9 nm at 20 K. This is explained by populating the higher vibronic- and Stark-sublevels of the ground state, which lead to the reabsorption of the emitted light and cause only longer wavelength (lower energies) to be detected. This is confirmed by the fact that the energy corresponding to the temperature change (kT) have the order of magnitude of that corresponding to the wavelength shift.

In figure 7.5 a broadband emission from the same Yb_2O_3 film is presented. The spectrum was recorded under 220 nm excitation, at a temperature of 9 K. Such double band emission have been also observed in many Yb-doped materials, including Yb:Y_2O_3 and Yb:Sc_2O_3 among the others. It is considered to be the radiative decay of the charge transfer[1] (CT) state. Throughly this kind of luminescence has been studied by L. van Pieterson in her thesis [Pie01]. The distance between the maxima of the bands corresponds to the energy distance of the both Yb^{3+} multiplets. Hence, it is supposed that low energetic band is caused by the same excitonic state, where some amount of energy is spent to excite an Yb^{3+}-ion. The fact that this emission is observed conform with the crystalline character of the films, as periodic lattice should exist in order to observe charge transfer emission.

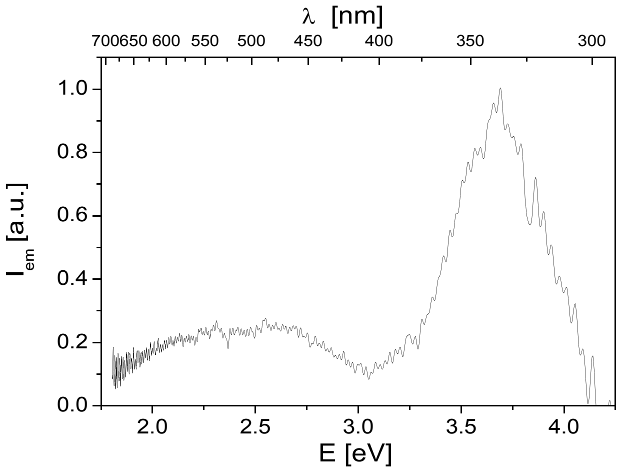

Figure 7.5: Broadband visible emission of the 500 nm Yb_2O_3 film on α-SiO_2 substrate detected under 220 nm (5.6 eV) excitation (T=9K).

7.2.2 Yb-doped Sesquioxide Films

In order to reduce the energy migration rates, materials with lower Yb^{3+} density are required. Implementing this idea, ytterbium-doped lutetia and scandia films[2] have been grown and spectroscopically investigated. Two Yb:Lu_2O_3 films have been deposited on a (0001)-oriented α-Al_2O_3 and homoepitaxially on a (111)-oriented Lu_2O_3 substrates. In the same way two Yb:Sc_2O_3 films have been produced on a (0001)-oriented α-Al_2O_3 and on a (111)-oriented Sc_2O_3 substrates. The thicknesses of the films are 3.3 μm and 3.5 μm for lutetia and 4 μm for both scandia films,

---

[1] Charge transfer state is an electronic state, where the large fraction of an electronic charge is transfer from one molecular entity to another, in this case from ligand (O^{2-}) to metal (Yb^{3+}).

[2] Y10-Y13 (appendix A).

respectively. The ytterbium concentrations are 5 mol.% (1.43×10^{21} cm^{-3}) and 4 mol.% (1.34×10^{21} cm^{-3}) for Yb:Lu_2O_3 and Yb:Sc_2O_3 films, respectively. The doping levels have been chosen to give approximately the same concentration of Yb^{3+} per unit volume for all Yb-doped films (including Yb:YAG films discussed below). This allows to compare the materials properties, excluding the non-equal influence of the energy migration effects.

The films deposited on sapphire substrates have been cut in two parts and one part of each sample was annealed in air at 900°C for 1 hour. This was made to investigate the influence of the higher temperatures on the film properties, since the maximum achievable substrate temperature during the deposition process was 730°C. The visual examination revealed that the “as deposited” films are fully transparent, however after annealing both lutetia and scandia films become foggy. The films have been suspended and covered during annealing, so one can exclude possible sintering with dust or particles from the vessel.

Emission and Excitation spectroscopy

The emission and excitation spectra have been recorded under continuous IR excitation with a Ti:Sapphire laser (see section 3.4 for details). The spectra for Yb:Lu_2O_3 and for Yb:Sc_2O_3 films are presented in figures 7.6 and 7.7, respectively. For comparison, the corresponding bulk crystal spectra are shown as well. The peak emission cross-sections of Yb^{3+} have been calculated using the Füchtbauer-Ladenburg method (equation 3.16). Both emission and excitation spectra of Yb:Lu_2O_3 films closely resemble the absorption[1] and emission spectra of the bulk crystal. The peak cross-sections of the zero-phonon line are slightly lower for “as deposited” films and reach the value of the bulk Yb:Lu_2O_3 crystal for the annealed films. The width of the emission peak is 3.0 nm for both “as deposited” films and decreased down to 2.8 nm after annealing. In the case of Sc_2O_3, the spectra are very close to the bulk spectra as well, however the film

---

[1] Due to the thermal coupling of all sublevels of the multiplets in the Yb^{3+}-ion energy scheme, the structure of absorption and excitation spectra of Yb^{3+} are similar.

deposited on sapphire substrate revealed ~30% lower peak emission cross-section. After annealing the spectrum has recovered and was almost identical to the bulk crystal spectrum. The width of the zero phonon line reduced from 2.4 nm to 2.0 nm after annealing . For the homoepitaxially grown film the width of the peak is 2.0 nm.

The zero-phonon line has been utilized to estimate the broadening of the spectrum caused by not quite perfect crystalline structure of the PLD-films. However, laser operation cannot be achieved at the zero-phonon line wavelength, because of strong reabsorption. Laser action in bulk Yb:Lu_2O_3 and Yb:Sc_2O_3 bulk crystals have been achieved using the lines at 1030-1045 nm and at 1080-1090 nm [Mix99]. This lines are quite broad and does not seem to be notably influenced by the crystal structure variations in the PLD-films.

Fluorescence Lifetime Measurements

The results of fluorescence lifetime measurements of Yb-doped scandia and lutetia films are presented in table 7.1. These experiments have been performed using the set-up described in section 3.4. The Yb-dopants were excited in the wavelength range of 940 nm – 950 nm and the emission was detected in the range of 975 nm – 977 nm. It can be noted that the lifetime values for the ytterbium-doped films are somewhat lower than

Table 7.1. Room temperature excited state lifetimes of the $^2F_{5/2}(Yb^{3+})$ multiplet in Sc_2O_3 and Lu_2O_3.

Host	**Yb-density, [10^{21} cm^{-3} (mol.%)]**	**Lifetime (τ) [μs]**
Lu_2O_3 film on α-Al_2O_3	1.43 (5)	545
Lu_2O_3 film on α-Al_2O_3 (annealed)	1.43 (5)	516
Lu_2O_3 film on Lu_2O_3	1.43 (5)	420
Sc_2O_3 film on α-Al_2O_3	1.34 (4)	497
Sc_2O_3 film on α-Al_2O_3 (annealed)	1.34 (4)	458
Sc_2O_3 film on Sc_2O_3	1.34 (4)	573
Lu_2O_3 crystal	0.13 (0.46) / 2.81 (10)	820 / 530 [Pet01]
Sc_2O_3 crystal	0.1 (0.3) / 3.36 (10)	730 / 776 [Pet01]

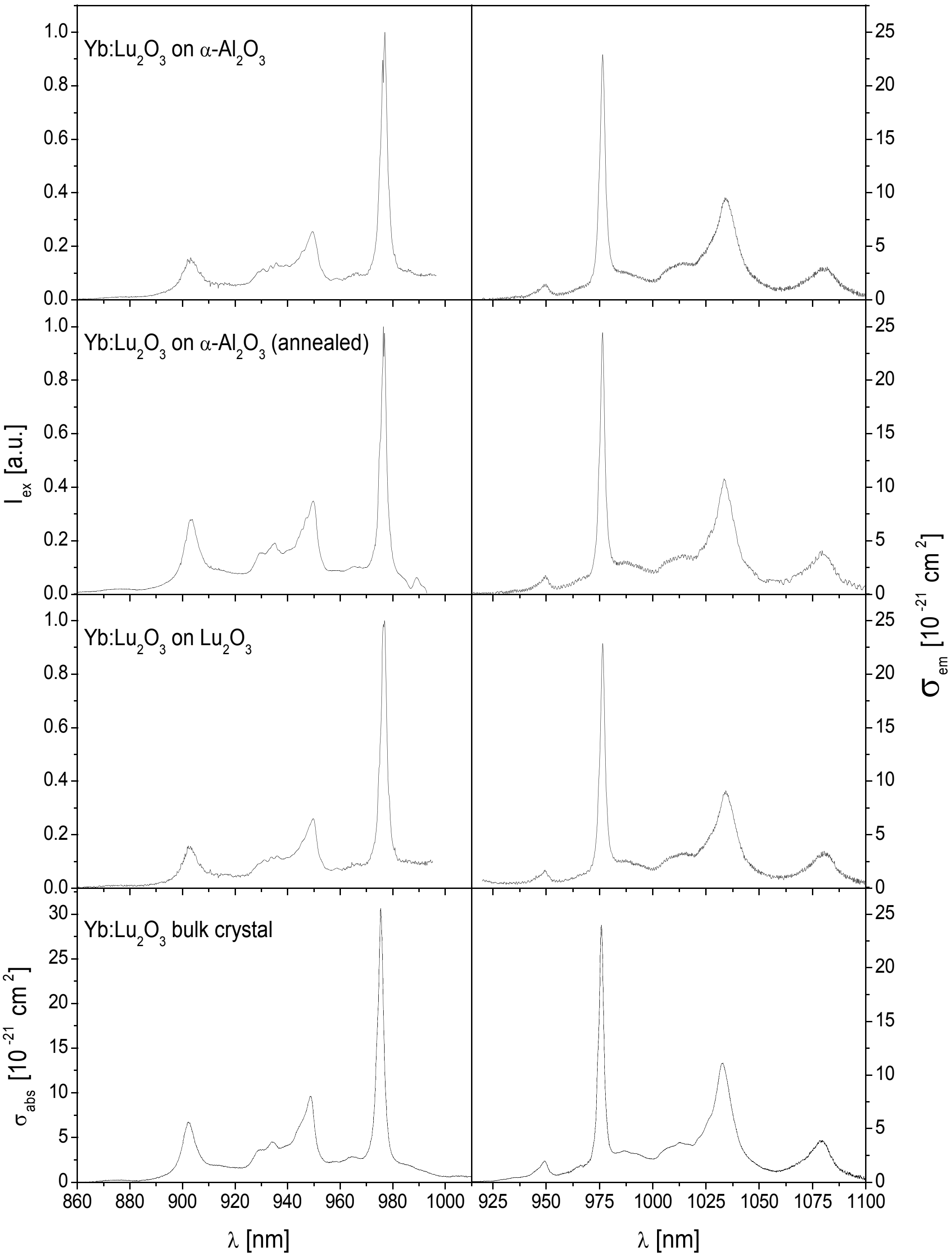

Figure 7.6: Excitation (left, λ_{em}=1030 nm) and emission cross-section (right, λ_{ex}=902.5 nm) spectra of the Yb:Lu$_2$O$_3$ PLD-films. Yb:Lu$_2$O$_3$ bulk crystal emission and absorption spectra [Pet01] presented for comparison.

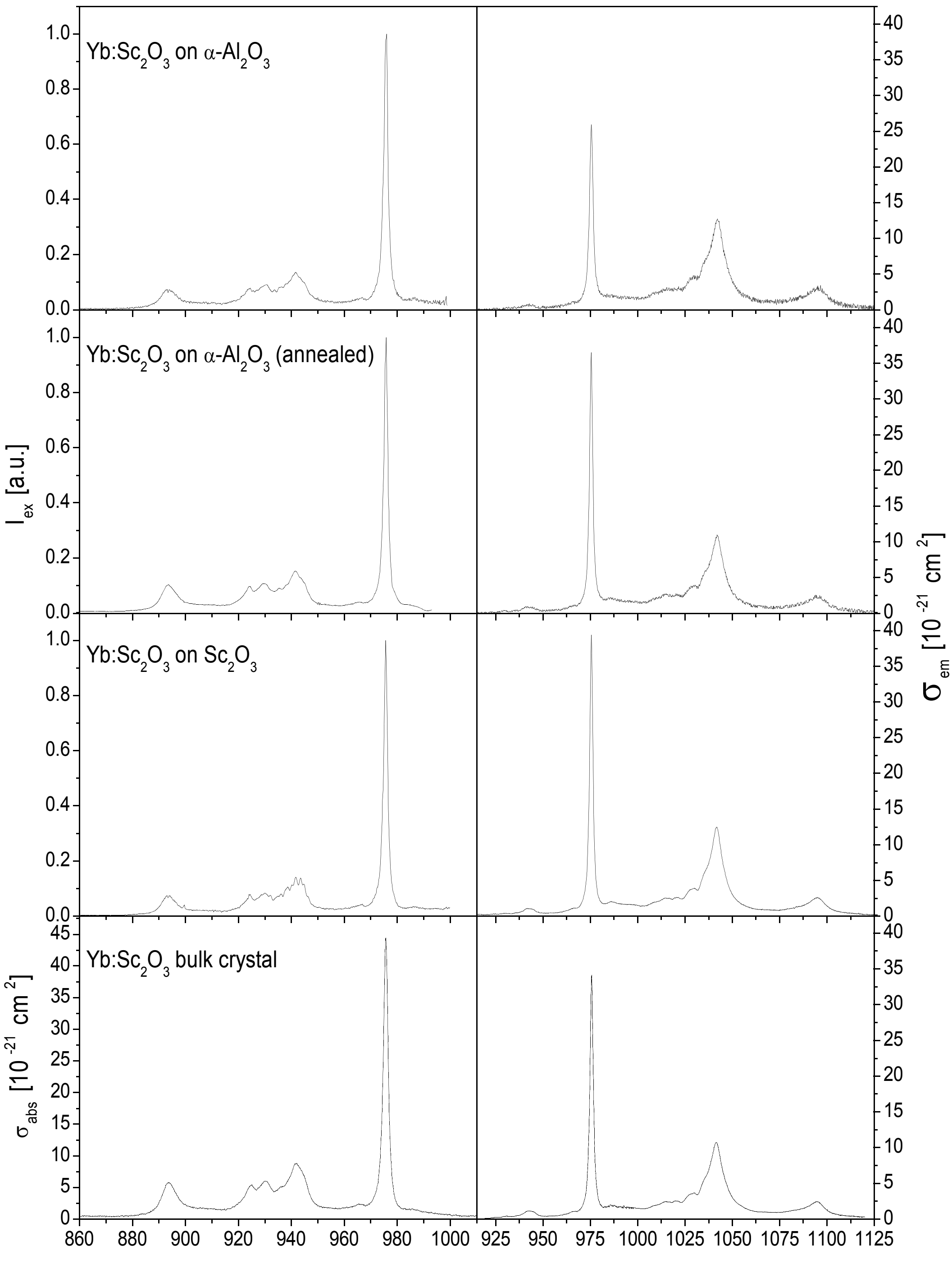

Figure 7.7: Excitation (left, λ_{em}=1042 nm) and emission cross-section (right, λ_{ex}=893.5 nm) spectra of the Yb:Sc$_2$O$_3$ PLD-films. Yb:Sc$_2$O$_3$ bulk crystal emission and absorption spectra [Pet01] presented for comparison.

that of the corresponding bulk crystal. This indicates that quantum efficiency of the Yb^{3+} luminescence is reduced, presumably due to higher density of crystal lattice defects. The quantum efficiency can be estimated using equation 3.18 and was found to be in the range of 51%-66% for the $Yb:Lu_2O_3$ films and 68%-78% for $Yb:Sc_2O_3$ films. The fluorescence decay lifetimes for the low-doped bulk crystals have been taken as the radiative lifetimes. This assumption can be made, since at such low concentrations the migration rate to the defects or impurities is negligible and other deexcitation channels are not present in the Yb^{3+}-ion. These lifetimes values have been also used in equation 3.16 for calculations of emission cross-sections.

The lifetime drop for the annealed lutetia and scandia films in the comparison with the "as deposited" films should be mentioned. However up to now no explanation for this effect have been found. Since improved crystallinity, as it follows from the sharper spectral lines, and higher peak cross-sections, should also result in lower defect density and longer lifetimes. One of the possible explanations can be increased migration rate, due to the reduced inhomogeneous broadening and better overlap of the energy levels of individual Yb^{3+}-ions.

7.2.3 Yb-doped YAG Films

Currently, Yb-doped yttrium-aluminum garnet is the most widely used host material for thin disk lasers. This section presents the results of spectroscopic investigations of Yb-doped YAG PLD films.

Two Yb:YAG have been deposited on a (0001)-oriented α-Al_2O_3 substrate and homoepitaxially on a (100)-oriented YAG substrate[1]. Subsequently both samples have been cut in two parts and one half of each sample has been annealed in the air at 1100°C during 1 hour. Again, as in the case of sesquioxide films, the annealed samples have been found to be foggy. Crystalline structure investigation and deposition parameters of the YAG films are discussed in section 5.2. Briefly, the XRD analysis showed that

---

[1] Y14-Y15 (appendix A).

the “as deposited” films are amorphous and the annealed samples showed polycrystalline behavior.

Emission and Excitation spectroscopy

Both excitation and emission spectra of “as deposited” films do not show the typical Yb:YAG spectra (figure 7.8). The zero-phonon line can be easily identified, however it is broadened and the broad band emission is observed instead of the expected side bands. The position of the zero phonon line and the intensity distribution has been found to resemble the absorption[1] and emission spectra of Yb:Y_2O_3 more closely than those of Yb:YAG. The annealed films on the contrary reveal the well-known, almost undistorted Yb:YAG spectra. Thus it can be concluded that the deposition temperature of 700°C was not high enough for the YAG lattice to build up and the deposited films are amorphous or, possibly, nanocrystallites of Yb:Y_2O_3 are formed. It seems, that temperatures higher than 700°C is required for YAG lattice to beformed. The results confirming this fact are observed, when amorphous 100 nm Eu:Y_2O_3 films on sapphire substrates have been annealed at the different temperatures [Bär05]. Up 1000°C typical Eu:Y_2O_3 spectrum was observed, but for the temperatures over 1000°C also Eu:YAG lines appear in the spectrum. In this case YAG was formed due to mutual indiffusion of Y_2O_3 and Al_2O_3. Similar effect have been observed by C. Grivas *et al.* for Nd-doped gadolinium-gallium garnet (GGG) films deposited at 650°C. The emission spectra of Nd^{3+} was noticeably broadened [Gri04a], in spite of the fact that the x-ray diffraction analysis have shown epitaxial growth of the Nd:GGG films on YAG substrates [Gri04b].

Fluorescence Lifetime Measurements

The result of the fluorescence lifetime measurements of the $^2F_{5/2}$ multiplet of Yb^{3+}-ion in the Yb:YAG films are presented in table 7.2. Yb^{3+}-ions were excited at the wavelength of 940-950 nm and emission at 975 nm or

---

[1] Due to the thermal coupling of all sublevels of the multiplets in the Yb^{3+}-ion energy scheme, the structure of absorption and excitation spectra of Yb^{3+} are similar.

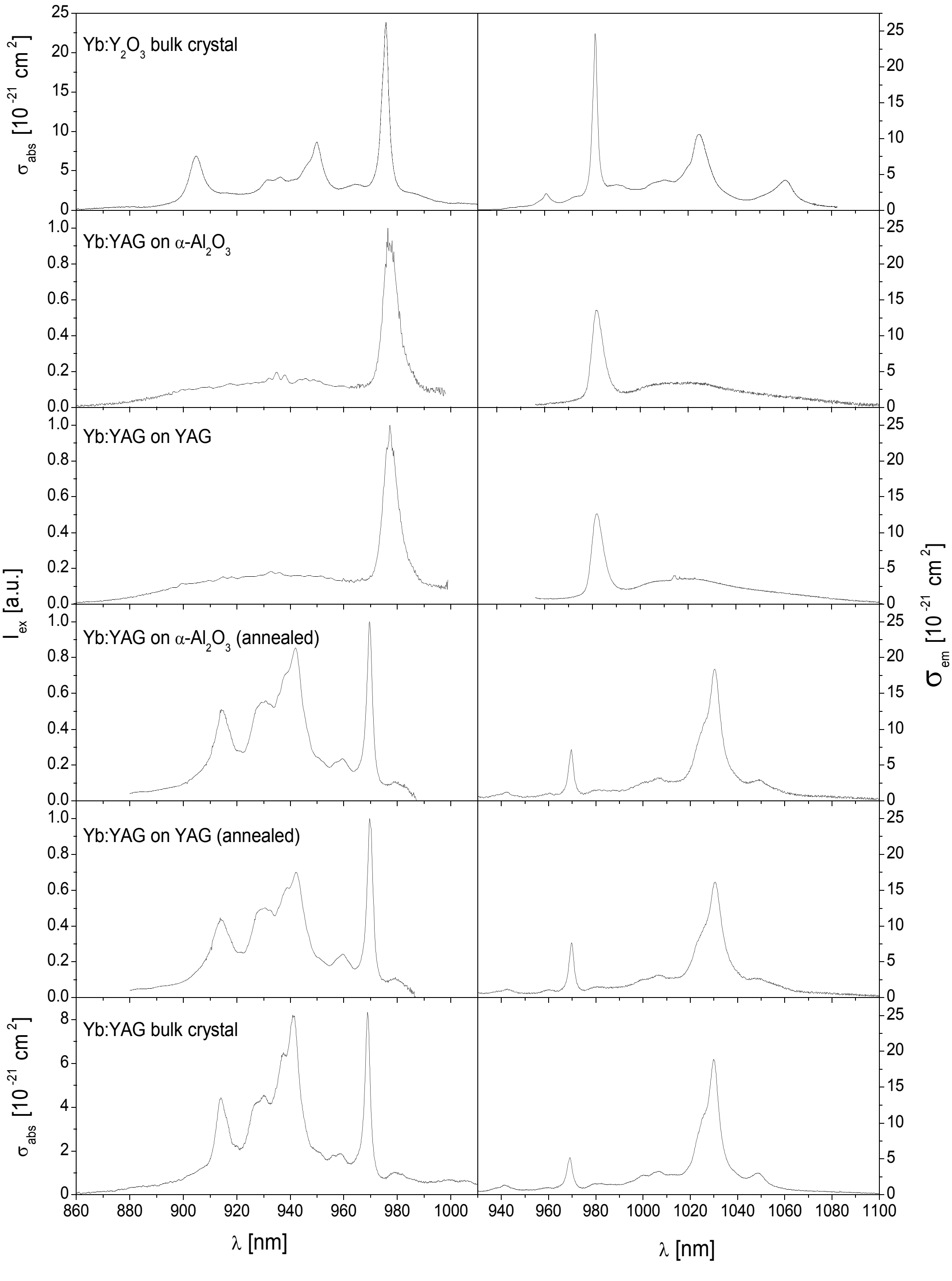

Figure 7.8: Excitation (left, λ_{em}=1020-1030 nm) and emission cross-section (right, λ_{ex}=915-930 nm) spectra of the Yb:YAG PLD-films. Yb:YAG and Yb:Y_2O_3 bulk crystal emission and absorption spectra [Pet01] are presented for comparison.

Table 7.2. Room temperature excited state lifetimes of the $^2F_{5/2}(Yb^{3+})$ multiplet in YAG.

Host	Yb-density [10^{21} cm^{-3} (mol.%)]	Lifetime (τ) [μs]
YAG film on α-Al_2O_3	1.38 (10)	608
YAG film on α-Al_2O_3 (annealed)	1.38 (10)	763
YAG film on YAG	1.38 (10)	606
YAG film on YAG (annealed)	1.38 (10)	784
YAG crystal	2.0 (15)	1040 [Pet05]
Y_2O_3 crystal	0.07 (0.26) / 2.39 (8.9)	790 / 580 [Pet01]

1030 nm was analyzed. The lifetimes of $^2F_{5/2}(Yb^{3+})$ for both samples increased substantially after annealing. Such a behavior can be expected for the Yb^{3+} in a YAG crystalline lattice, in comparison with amorphous films or Y_2O_3 nanocrystallites. According to equation 3.18 quantum efficiency is estimated to be 58% for "as deposited" films and up to 75% for annealed samples.

§7.3 Summary and Discussion

In this chapter the properties of Yb_2O_3, Yb:Lu_2O_3, Yb:Sc_2O_3, and Yb:YAG PLD-films have been discussed. The Yb_2O_3 films have been found to be not suitable for application as an active medium. Due to very high density of Yb^{3+}-ions, the energy migration process is so fast, that even extremely low concentration of impurities, believed to be already present in source material, causes fast nonradiative deexcitation.

The emission cross-section and excitation spectra of Yb:Lu_2O_3 films resemble closely the corresponding spectra of the bulk Yb:Lu_2O_3 crystal. However, the luminescence quantum efficiency of 66% can be too low for applications as a effective laser medium and need to be improved. Yb:Sc_2O_3 have revealed higher quantum efficiency up to 78%. Together with higher peak emission cross-sections, Yb:Sc_2O_3 films look more interesting for applications than Yb:Lu_2O_3 films. However, as it can be noted on slightly broadened spectra of the Yb:Sc_2O_3 film on a sapphire substrate, deposition parameters still need some optimization. Though, since the annealing at the temperature of 900°C eliminated this broadening effect, it does not seem to be a fundamental problem.

The “as deposited” Yb:YAG films revealed very poor spectroscopic properties. The films deposited at 700°C did not reveal spectra characteristic for Yb:YAG. After annealing at 1200°C typical Yb:YAG spectra and improved lifetimes have been observed. The quantum efficiency of the luminescence was found to be up to 75% for the annealed films. It can be concluded that the higher substrate temperatures are required for the deposition of the crystalline Yb:YAG films directly.

The effect of the annealing is found to be quite contradictory. On the one side it eliminates the spectral broadening. On the other side, in the case of the Yb-doped sesquioxide films, it caused degraded lifetimes of the excited state of Yb^{3+}. The fact, that all annealed films become partly scattering (foggy), is another drawback of the annealing. Presumably recrystallization at the surface can be a reason for this effect. Quite similar destruction of the surface structure was observed after annealing of bulk sesquioxides crystals.

The influence of the substrate on the spectroscopic properties of the film has been noticed for the case of Yb:Sc_2O_3 film. The spectra of the film deposited on the sapphire substrate was slightly broadened. This effect cannot be explained by poorer crystallinity of the film in comparison with the homoepitaxially grown film, since the XRD analysis shows crystallines in the range of hundreds of nanometers. In the case of Lu_2O_3 the substrate have not influenced the spectroscopic properties of the deposited films. Spectra of the homoepitaxially deposited Yb:Lu_2O_3 film have been slightly broadened, as well as the spectra of the film deposited on a sapphire substrate.

Chapter 8. Conclusions

The subject of this thesis was the characterization of rare-earth-doped oxide films fabricated by pulsed laser deposition and the analysis of their possible application as active media, e.g for waveguide or thin disk lasers. The experimental results of the film preparation, the XRD analysis, the characterization of the waveguiding films, and the properties of the Yb-doped films were summarized at the end of chapters 4-7, respectively. This chapter resumes the results of this thesis and gives an outlook for future research.

§8.1 Summary of Results

Crystalline sesquioxide (scandia, yttria, ytterbia, and lutetia) PLD-films have been successfully grown in the course of this work. In case of scandia the properties of the films depending on the deposition parameters have been investigated in more detail.

As follows from the XRD investigations of the sesquioxide films in the framework of this thesis as well as from the results of previous works in the solid-state laser group at University of Hamburg [Bur02, Bär04, Rab04], higher crystalline quality is achieved for scandia PLD-films compared to lutetia or yttria films deposited under similar conditions. This effect is due to the low mass of the scandium ion and, consequently, the high mobility on the substrate surface, which results in a more effective lattice formation. For the 500 nm Sc_2O_3 films on sapphire substrates a lower limit for the crystallite dimensions was estimated to be about 330 nm. The real dimensions cannot be determined, since the resolution limit of the diffractometer was reached. In case of lutetia a comparable crystalline quality is achieved only for homoepitaxially grown PLD-films. The films deposited on sapphire substrates reveal crystallites sizes in the range of several tens of nanometers. The ytterbia films on sapphire substrates behave similarly.

The spectroscopic investigations on the Yb-doped scandia and lutetia films reveal, that their emission and excitation spectra resemble closely those of bulk crystals. Lower crystalline quality of lutetia films compared to scandia ones causes stronger broadening of the Yb-dopant emission and excitation spectra. In case of the Nd-doped scandia films the spectra are slightly broadened and the peak cross-sections reach about 70% of those of the bulk crystal values. The Eu-doped yttria film show bulk-like spectra.

Both for the Nd- and the Yb-doped films a decrease in the lifetime of the excited states compared to the corresponding bulk crystal is observed. This effect is due to the higher lattice defect density and the local symmetry distortion in the film structure compared to the bulk crystal. However, these negative effects are not dramatic and the spectroscopic properties of the Yb-doped films can be considered promising for applications as active media.

The ytterbia films show very poor spectroscopic properties, which presumably results from impurities present in the source material. The Yb:YAG PLD-films grown under conditions similar to that used for the sesquioxide films have been proven to be amorphous. This was confirmed by spectroscopic and XRD measurements. After annealing at 1200°C the films show polycrystalline behavior and their spectroscopic properties are bulk-like. Thus, a substrate temperature of 700°C was found to be too low for the deposition of crystalline Yb:YAG films. The post-annealing experiments at 900°C with the Yd-doped scandia and lutetia films delivered somewhat contradictory results. On the one hand the residual broadening of the spectra was reduced, on the other the excited state lifetimes decreased slightly. The latter effect is not yet fully understood. In addition, the annealed films have also become strongly scattering.

As a step towards the realization of a waveguide laser and active elements for integrated optical devices, the characterization of the Nd-doped scandia films was performed. The 3 μm and 10 μm thick waveguiding films have revealed relatively high light propagation losses of 19.5 dB·cm^{-1} and 12 dB·cm^{-1}, respectively. This is considered the main reason for the failure of laser experiments with these waveguides. The analysis of the scattering behavior revealed, that particulates at the film surface most probably cause the high propagation losses.

§8.2 Resumé and Outlook

The results of this thesis show, that scandia films of high crystalline quality can be produced by pulsed laser deposition. The spectroscopic properties of the rare-earth-doped lutetia, scandia, yttria, and YAG PLD-films are close but not identical to those of the corresponding bulk crystals. Further optimization of the deposition conditions should be performed to obtain higher quality films. However, the film properties are suitable for applications as active media.

In the course of this work some technical limitations have been found to influence the achievable quality of the PLD-films. Thus, the maximum substrate temperature available with the used set-up was not high enough and deposition at higher substrate temperatures can improve spectroscopic properties of the films. In order to achieve laser operation in the PLD-waveguides, the propagation losses should be reduced. The use of dense, crystalline targets instead of ceramic ones should reduce the number of particulates and, consequently, the scattering losses.

Some further experimental techniques can be utilized to characterize the fabricated films. Recently, experiments using RHEED (Reflection High Energy Electron Diffraction) have been started in order to investigate the film growth process in situ. Additionally, AFM (Atomic Force Microscopy) will be employed to analyze the roughness of the film surface. Thus, optimal deposition parameters can be determined for the deposition of smooth, weakly scattering films.

The range of available wavelengths can be expanded using other rare-earth ions (Er^{3+}, Tm^{3+}, Ho^{3+}, Pr^{3+}, etc) as dopants, which will make such PLD-films interesting for telecommunication, sensing, or display applications.

Further research is still necessary before devices based on rare-earth-doped oxide films can be produced. For realization of integrated optical devices, the techniques for structuring of oxide materials have to be developed. The application of oxide PLD-films as an active medium in the thin disk laser set-up seem to be currently limited by their thickness. The fabrication of coatings or photonic structures, like Bragg mirrors or microcavities, can be a promising application for oxide PLD-films as well.

Appendix A. List of Deposited Films

Here the deposition conditions for the films deposited and characterized in the course of the work are summarized. “Lxx” series is discussed in section 4.3; “Wxx” in chapter 6; and “Yxx” in chapters 5 and 7.

Name	Material	Dopant (mol.%)	h, nm	Sub-strate	T_{sub}, °C	P_{O2}, mbar	$d_{targ\text{-}sub}$, cm	Φ, J·cm^{-2}	ν_{laser}, Hz	N_{pulses}, 10^3	Comments
L01	Sc_2O_3	Nd(0.2)	1000	α-Al_2O_3	20	1×10^{-3}	9.5	2.5	27	38.3	
L02	Sc_2O_3	Nd(0.2)	1000	α-Al_2O_3	20	1×10^{-3}	9.5	2.2	27	61.4	
L03	Sc_2O_3	Nd(0.2)	1000	α-Al_2O_3	20	1×10^{-3}	9.5	1.3	43	158.7	
L04	Sc_2O_3	Nd(0.2)	525	α-Al_2O_3	20	1×10^{-3}	9.5	1.2	27	76.8	
L05	Sc_2O_3	Nd(0.2)	500	α-Al_2O_3	20	1×10^{-3}	9.5	1.8	27	51.8	
L06	Sc_2O_3	Nd(0.2)	500	α-Al_2O_3	20	1×10^{-3}	9.5	2.5	27	39.0	
L07	Sc_2O_3	Nd(0.2)	500	α-Al_2O_3	300	1×10^{-3}	9.5	2.5	27	31.2	
L08	Sc_2O_3	Nd(0.2)	510	α-Al_2O_3	500	1×10^{-3}	9.5	2.5	27	27.1	
L09	Sc_2O_3	Nd(0.2)	500	α-Al_2O_3	700	3×10^{-4}	9.5	2.5	31	28.9	
L10	Sc_2O_3	Nd(0.2)	500	α-Al_2O_3	700	1×10^{-3}	9	2.5	31	27.4	
L11	Sc_2O_3	Nd(0.2)	500	α-Al_2O_3	700	3×10^{-3}	9	2.5	31	26.4	
L12	Sc_2O_3	Nd(0.2)	500	α-Al_2O_3	700	1×10^{-2}	9	2.5	31	50.3	
L13	Sc_2O_3	Nd(0.2)	500	α-Al_2O_3	700	3.1×10^{-2}	9	2.5	31	47.0	
L14	Sc_2O_3	Nd(0.2)	500	α-Al_2O_3	700	1×10^{-1}	9	2.5	31	68.4	
L15	Sc_2O_3	Nd(0.2)	500	α-Al_2O_3	700	1.8×10^{-2}	9	2.5	31	36.8	
L16	Sc_2O_3	Nd(0.2)	500	α-Al_2O_3	700	3.4×10^{-2}	9	2.5	31	50.3	

Name	**Material**	**Dopant (mol.%)**	**h, nm**	**Sub-strate**	**T_{sub}, °C**	**P_{O2}, mbar**	**$d_{targ\text{-}sub}$, cm**	**Φ, J·cm^{-2}**	**ν_{laser}, Hz**	**N_{pulses}, 10^3**	**Comments**
W06	Y_2O_3	Eu(1.5)	1200	α-SiO_2	730	1×10^{-2}	10.5	3.5	20	253.0	showed waveguiding
W10	Sc_2O_3	Nd(0.2)	3000	α-Al_2O_3	690	3.3×10^{-3}	8	3.5	37	899.7	showed waveguiding 1.5 µm Al_2O_3 superstrate
W12	Sc_2O_3	Nd(0.2)	10000	α-Al_2O_3	700	2×10^{-3}	8	2.5	31	414.4	showed waveguiding 5µm Al_2O_3 superstrate
Y01	Yb_2O_3	-	520	α-Al_2O_3	700	1×10^{-2}	8	3.5	31	391.5	
Y02	Yb_2O_3	-	100	α-Al_2O_3	700	1×10^{-2}	8	3.5	31	216	
Y03	Yb_2O_3	-	300	α-Al_2O_3	700	1×10^{-2}	8	3.5	31	68.0	
Y04	Yb_2O_3	-	20	α-Al_2O_3	700	1×10^{-2}	8	3.5	31	5	
Y05	Yb_2O_3	-	100	α-Al_2O_3	700	1×10^{-2}	8	3.5	31	36.5	
Y06	Yb_2O_3	-	5	α-Al_2O_3	700	1×10^{-2}	8	3.5	31	1.75	
Y07	Yb_2O_3	-	500	α-SiO_2	660	1×10^{-2}	8	3.5	31	210.7	
Y08	Yb_2O_3	-	135	α-SiO_2	660	1×10^{-2}	8	3.5	31	46.9	
Y09	Yb_2O_3	-	20	α-SiO_2	660	1×10^{-2}	8	3.5	31	6.9	
Y10	Lu_2O_3	Yb(5)	3300	α-Al_2O_3	700	1×10^{-2}	9	2.5	31	525.1	½ annealed (900°C, 1h)
Y11	Lu_2O_3	Yb(5)	3500	Lu_2O_3	700	1×10^{-2}	9	2.5	31	555.6	
Y12	Sc_2O_3	Yb(4)	4000	α-Al_2O_3	700	1×10^{-2}	9	2.5	31	227.7	½ annealed (900°C, 1h)
Y13	Sc_2O_3	Yb(4)	4000	Sc_2O_3	700	1×10^{-2}	9	2.5	31	219.9	
Y14	YAG	Yb(10)	3950	α-Al_2O_3	700	1×10^{-2}	9	2.5	31	269	½ annealed (1200°C, 1h)
Y15	YAG	Yb(10)	4000	YAG	700	1×10^{-2}	9	2.5	31	290	½ annealed (1200°C, 1h)

Appendix B. Fresnel Equations

σ-polarization (TE)
(Transversal Electric field)

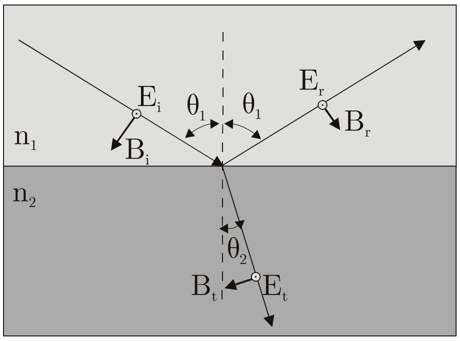

$$r^{\sigma}=\frac{n_1\cos(\theta_1)-n_2\cos(\theta_2)}{n_1\cos(\theta_1)+n_2\cos(\theta_2)} \tag{B.1}$$

$$t^{\sigma}=\frac{2\,n_1\cos(\theta_1)}{n_1\cos(\theta_1)+n_2\cos(\theta_2)} \tag{B.2}$$

π-polarization (TM)
(Transversal Magnetic field)

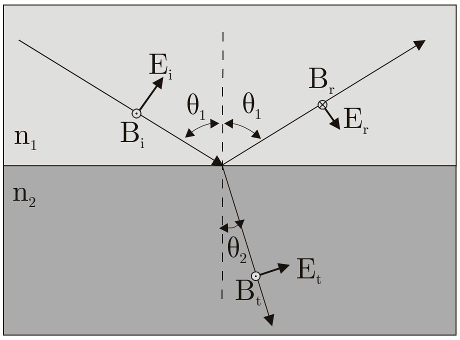

$$r^{\pi}=\frac{n_1\cos(\theta_2)-n_2\cos(\theta_1)}{n_1\cos(\theta_2)+n_2\cos(\theta_1)} \tag{B.3}$$

$$t^{\pi}=\frac{2\,n_1\cos(\theta_1)}{n_1\cos(\theta_2)+n_2\cos(\theta_1)} \tag{B.4}$$

Bibliography

[Abr78] V. N. Abramov and A. I. Kuznetsnov, *Fundamental absorption of Y_2O_3 and $YAlO_3$*, Sov. Phys. Solid State, **20 (3)** (1978) 399.

[And97] A. A. Anderson, R.W. Eason, L. M. B. Hickey, M. Jelinek, C. Grivas, D. S. Gill, and N. A. Vainos, *Ti:Sapphire planar waveguide laser grown by pulsed laser deposition*, Opt. Lett., **22** (1997) 1556-8.

[And97a] A. A. Anderson, R. W. Eason, M. Jelinek, C. Grivas, D. Lane, K. Rogers, L. M. B. Hickey, and C. Fotakis, *Growth of Ti:sapphire single crystal thin films by pulsed laser deposition*, Thin Solid Films, **300** (1997) 68-71.

[And97b] A. A. Anderson, R. W. Eason, L. M. B. Hickey, M. Jelinek, C. Grivas, D. S. Gill, and N. A. Vainos, *Ti:sapphire planar waveguide laser grown by pulsed laser deposition*, Opt. Lett., **22** (1997) 1556-8.

[And98] A. A. Anderson, *Crystalline Planar Waveguide Lasers Fabricated by Pulsed Laser Deposition.* PhD Thesis, University of Southampton, 1998.

[Ata00] P. A. Atanasov, R. I. Tomov, J. Perriere, R. W. Eason, N. Vainos, A. Klini, A. Zherikhin, and E. Millon, *Growth of Nd: potassium gadolinium tungstate thin-film waveguides by pulsed laser deposition*, Appl. Phys. Lett., **76** (2000) 2490.

[Aul82] B. F. Aull and H. P. Jenssen, *Vibronic Interactions in Nd:YAG Resulting in Nonreciprocity of Absorption and Stimulated Emission Cross Sections*, IEEE J. of Quant. Electr., **18** (1982) 925.

[Bar01] S. J. Barrington, *Planar Waveguide Devices Fabricated by Pulsed Laser Deposition.* PhD Thesis, University of Southampton, 2001.

[Bär04] S. Bär, *Crystalline Rare-Earth-doped Sesquioxide PLD-Films on α-Alumina (preparation and characterization).* Dissertation, Institut für Laser-Physik, Universität Hamburg, 2004.

[Bär05] S. Bär, *unpublished results* (Institut für Laser-Physik, Universität Hamburg, 2005).

[Bar57] C. Barta, F. Petru and B. Hajek, *Über die Darstellung des Einkristalls von Scandiumoxyd*, Die Naturwissenschaften, **45** (1957) 36.

[Bäu00] D. Bäuerle, Laser Processing and Chemistry (Springer-Verlag, Berlin, Heidelberg, New York, 2000).

[Bjö96] G. Björk, *Microcavity Lasers and QED* (in *Laser Sources and Applications: Proceedings of the Forty Seventh Scottish Universities Summer School in Physics, St. Andrews* /ed. by A. Miller and D. M. Finlayson), Institute of Physics, Bristol, 1996.

[Bon00] C. L. Bonner, *Mult-Wat, Diode-Pumped Planar Waveguide Lasers.* PhD Thesis, University of Southampton, 2000.

[Bos04] A. Bosco, M. Centini, L. Sciscione, C. Sibilia, E. Fazio, M. Bertolotti, A. Fiore, A. Convertino, L. Cerri, and M. Scalora, *Nonlinear type-II second-harmonic generation in AlGaAs/Al_2O_3 one-dimentional photonic crystal*, Appl. Phys. Lett., **84** (2004) 16.

[Bru04] F. Brunner, E. Innerhofer, S. V. Marchese, T. Südmeyer, R. Paschotta, T. Usami, H. Ito, S. Kurimura, K. Kitamura, G. Arisholm, and U. Keller, *Powerful red-green-blue laser source pumped with a mode-locked thin disk laser*, Opt. Lett., **29** (2004) 1921-3.

[Bur02] P. Burmester, *Optisch aktive, kristalline, Selten Erd-dotierte Y_2O_3-PLD-Schichten auf α-Al_2O_3.* Dissertation, Institut für Laser-Physik, Universität Hamburg, 2002.

[Cha63] N. C. Chang, *Fluorescence and Stimulated Emisson from Trivalent Europium in YttriumOxide*, J. Appl. Phys., **34** (1963) 3500.

[Cha72] D. J. Channin,J. M. Hammer, J. P. Wittke, *Dispersion and loss in new thin-film optical waveguides*, IEEE J. Quantum Elect., **8** (1972) 6.

[Cha92] I. Chartier, B. Ferrand, D. Pelenc, S. J. Field, D. C. Hanna, A. C. Large, D. P. Shepherdund A. C. Tropper, *Growth and low-threshold laser oscillation of an epitaxially grown Nd:YAG waveguide*, Opt. Lett., **17** (1992) 810.

[Chi99] W. Y. Ching and Y.-N. Xu, *Nonscalability and nontransferability in the electronic properties of the Y-Al-O system*, Phys. Rev. B, **59** (1999) 12815-21.

[Chr94] D. B. Chrisey and G. K. Hubler, Pulsed Laser Deposition of Thin Films (John Wiley & Sons, Inc., New York, 1994).

[Cru03] A. Crunteanu, G. Jänchen, P. Hoffmann, M. Pollnau, C. Buchal, A. Petraru, R. W. Eason, and D. P. Shepherd, *Three-dimentional structuring of sapphire by sequential He$^+$ ion-beam implantation and wet chemical etching*, Appl. Phys. A, **76** (2003) 1109-12.

[Cul78] B. D. Cullity, Elements of X-ray Diffraction (Addison-Wesley, London, 1978).

[DeM88] F. De Martini and G. R. Jacobovitz, *Anomalous sponteneous-stimulated-decay phase transition and zero-threshold laser action in a microscopic cavity*, Phys. Rev. Lett., **60** (1988) 1711-4.

[Dex53] D. L. Dexter, *A Theory of Sensitzed Luminescence in Solids*, J. Chem. Phys., **21** (1953) 836-50.

[Dij87] D. Dijkamp, T. Venkatesan, X. D. Wu, S. A. Shaheen, N. Jisrawi, Y. H. Min-Lee, W. L. McLean, and M. Croft., *Preparation of Y-Ba-Cu oxide superconductorthin films using pulsed laser evaporation from high Tc bulk material*, Appl. Phys. Lett., **51** (1987) 619.

[Dri04] A. Driessen, D. H. Geuzebroek, H. J. W. M. Hoekstra, H. Kelderman, E. J. Klein, D. J. W. Klunder, C. G. H. Roeloffzen, F. S. Tan, E. Krioukov, C. Otto, H. Gersen, N. F. van Hulst, and L. Kuipers, *Microresonators as building blocks for VLSI Photonics (invited Lecture)* (in *AIP Conference Proceedings Vol. 709. Proceedings of International School of Quantum Electronics, Erice-Sicily, 2003*), 2004, pp. 1-18.

[Ehl05] S. Ehlert, *Herstellung und Charakterzsierung ultradünner PLD-Sesquioxidschichten auf Quartz.* Diplomarbeit, Institut für Laser-Physik, Universität Hamburg, 2005.

[Eza96] M. Ezaki, M. Obara, H. Kumagai, and K. Toyoda, *Characterization of* $Nd:Y_3Al_5O_{12}$ *thin films grown on varoius subsrates by pulsed laser deposition*, Appl. Phys. Lett., **69** (1996) 2977-9.

[Fin66] D. Findley and R. Clay, *The measurements of internal losses in 4-level lasers*, Phys. Lett., **20** (1966) 3.

[För48] T. Förster, *Zwischenmolekulare Energiewanderung und Fluoreszenzen*, Annalen der Physik, **2** (1948) 55-75.

[For99] L. Fornasiero, Nd^{3+} *und* Tm^{3+}*-dotierte Sesquioxide*. Dissertation, Institut für Laser-Physik, Universität Hamburg, 1999.

[For99a] L. Fornasiero, E. Mix, V. Peters, E. Heumann, K. Petermann, and G. Huber, *Efficient Laser Operation of* $Nd:Sc_2O_3$ *at 966 nm, 1082 nm, and 1486 nm* (in *OSA Trends in Optics and Photonics. Vol.26. Advanced Solid-State Lasers.* /ed. by M. M. Fejer, H. Inejeyan, and U. Keller), Opt. Soc. America, Washington, DC, USA, 1999.

[Fre90] R. H. French, *Electronic Structure of* α*-*Al_2O_3 *, with Comparison to AlON and AlN*, J. Am. Chem. Soc., **73** (1990) 477-89.

[Ger04] H. Gersen, D. J. W. Klunder, J. P. Korterik, A. Driessen, N. F. van Hulst, and L. Kuipers, *Propagation of a femtosecond pulse in a microresonator visualized in time*, Opt. Lett., **29** (2004) 1291-3.

[Gie94] A. Giesen, H. Hügel, A. Voss, K. Wittig, U. Brauch, and H. Opower, *Scalable Concept for Diode-Pumped High-Power Solid-State Lasers*, Appl. Phys. B, **58** (1994) 365-72.

[Gil96] D. S. Gill, A. A. Anderson, R. W. Eason, T. J. Warburton, and D. P. Shepherd, *Laser operation of an* $Nd:Gd_3Ga_5O_{12}$ *thin-film optical waveguide fabricated by pulsed laser deposition*, Appl. Phys. Lett., **69** (1996) 10-12.

[Gri04a] C. Grivas, T. C. May-Smith, D. P. Shepherd, R. W. Eason, *Laser operation of a low loss (0.1 dB/cm)* $Nd:Gd_3Ga_5O_{12}$ *thick (40*μ*m) planar waveguide grown by pulsed laser deposition*, Opt. Commun., **229** (2004) 355-61.

[Gri04b] C. Grivas, T. C. May-Smith, D. P. Shepherd, R. W. Eason, *On the growth and lasing characteristics of thick Nd:GGG waveguiding films fabricated by pulsed laser deposition*, Appl. Phys. A, **79** (2004) 1203-06.

[Gri04c] C. Grivas, T. C. May-Smith, D. P. Shepherd, R. W. Eason, M. Pollnau, and M. Jelinek, *Broadband single-transverse-mode fluorescence sources based on ribs fabricated in pulsed laser deposited Ti:sapphire waveguides*, Appl. Phys. A, **79** (2004) 1195-98.

[Grib04] U. Griebner, V. Petrov, K. Petermann, and V. Peters, *Passively mode-locked Yb:*Lu_2O_3 *laser*, Opt. Express, **12** (2004) 3125-30.

[Gup91] A. Gupta, B. W. Hussey, A. Kussmaul, and A. Segmuller, *Defect formation caused by a transient decrease in the ambient oxygen concentration during growth of* $YBa_2Cu_3O_{7-x}$ *films*, Appl. Phys. Lett., **57** (1991) 2365-7.

[Hic98] L. M. B. Hickey, *Ti:sapphire waveguide laser by thermal diffusion of titanium into sapphire.* PhD Thesis, University of Southampton, 1998.

[Hoe66] H. R. Hoekstra, *Phase relationships in the rare-earth sesquioxides*, Inorg. Chem., **5** (1966) 754.

[Hos64] R. H. Hoskins and B. H. Soffer, *Stimulated Emission from* Y_2O_3:Nd^{3+}, Appl. Phys. Lett., **4** (1964) 22.

[Ibr04] T. A. Ibrahim, K. Amarnath, L. C. Kuo, R. Grover, V. Van, and P.-T. Ho, *Photonic logic NOR gate based on two symmetric microring resonators*, Opt. Lett., **29** (2004) 1579-81.

[Kah05] A. Kahn, *Verlustmessungen an* Nd^{3+} *dotierten planaren Wellenleitern and deren Charakterisierung für Laseranwendungen.* Diplomarbeit, Universität Hamburg, 2005.

[Kik03] P. G. Kik and A. Polman, *Cooperative upconversion as the gain-limiting factor in Er doped miniature* Al_2O_3 *optical waveguide amplifiers*, J. Appl. Phys., **93** (2003) 5008-12.

[Kle05] D. O. Klenov, L. F. Edge, D. G. Schlom,and S. Stemmer, *Extended defects in epitaxial* Sc_2O_3 *films grown on (111) Si*, Appl. Phys. Lett., **86** (2005) 51901-3.

[Klo04] P. Klopp, V. Petrov, U. Griebner, K. Petermann, V. Peters, and G. Erbert, *Highly efficient mode-locked Yb:*Sc_2O_3 *laser*, Opt. Lett., **29** (2004) 391-3.

[Kor01] M. B. Korzenski, P. Lecoeur, B. Mercey, P. Camy, and J. L. Doualan, *Low propagation losses of an Er:*Y_2O_3 *planar waveguide grown by alternate-target pulsed laser deposition*, Appl. Phys. Lett., **78** (2001) 1210.

[Kuz04] Y. Kuzminykh, S. Bär, H. Scheife, G. Huber, V. Apostolopoulos, and M. Pollnau, *Waveguiding thin* Y_2O_3 *films grown on sapphire substrates* (in *Europhysics Conference Abstracts Volume 28C. Proceedings of the 1st EPS-QEOD Europhoton Conference*), 2004, Fib10128 (ThC25).

[Kuz06] Y. Kuzminykh, A. Kahn, and G. Huber, Nd^{3+} *doped* Sc_2O_3 *waveguiding film produced by pulsed laser deposition*, Opt. Mater., **28** (2006) 883-7.

[Lan04] J. Lancok, C. Garapon, C. Martinet, J. Mugnier, and R. Brenier, *Influence of the PLD parameters on the crystalline phases and flourescence of Eu:*Y_2O_3 *planar waveguides*, Appl. Phys. A, **79** (2004) 1263-65.

[Lan05] J. Lancok, C. Garapon, M. Jelinek, J. Mugnier, and R. Brenier, *Optical and structural properties of Pr:GGG crystalline thin film waveguides grown by pulsed-laser deposition*, Appl. Phys. A, **81** (2005) 1477-83.

[Lar05] M. Larionov, K. Schuhmann, J. Speiser, C. Stolzenburg and A. Giesen, *Nonlinear decay of the excited state in Yb:YAG* (in *Advanced Solid-State Photonics 2005 Technical Digest on CD-ROM*), 2005, TuB49.

[Lee86] D. H. Lee, Electromagnetic Principles of Integrated Optics (John Wiley & Sons, New York, 1986).

[Lev62] R. A. Lefever, *Flame Fusion Growth of C-Type Rare-Earth Oxides*, Rev. Sci. Instr., **33** (1962) 1470.

[Mac01] J. I. Mackenzie, C. Li, D. P. Shepherd, H. E. Meissner, and S. C. Mitchell, *Longitudinally diode-pumped Nd:YAG double-clad planar waveguide laser*, Opt. Lett., **26** (2001) 10.

[Mix99] E. Mix, *Kristallzüchtung, Spektroskopie und Lasereingenschaften Yb-dotierter Sesquioxide.* Dissertation, Institut für Laser-Physik, Universität Hamburg, 1999.

[Möl86] T. Möller, P. Gürtler, E. Roick, and G. Zimmerer, *The experimental station SUPERLUMI: a unique setup for time- and spectrally resolved luminescence under state selective excitation with synchrotron radiation*, Nucl. Instrum. Meth. Phys. Res. A, **246** (1986) 461-4.

[NDL] *NASA Database of Laser Materials.*

[Neg03] E. Negodine, *Inter- and intraconfigurational luminescence of* $LiYF_4$*:*Er^{3+} *under selective VUV excitation.* Dissertation, Universität Hamburg, 2003.

[Pay92] S. A. Payne, L. L. Chase, L. K. Smith, W. L. Kway, and W. F. Krupke, *Infrared Cross-Section Measurements for Crystals Doped with* Er^{3+}*,*Tm^{3+} *and* Ho^{3+}, IEEE J. of Quant. Electr., **28** (1992) 2619.

[Pet01] V. Peters, *Growth and Spectroscopy of Ytterbium-Doped Sesquioxides.* Dissertation, Institut für Laser-Physik, Universität Hamburg, 2001.

[Pet02a] V. Peters, A. Bolz, K. Petermann, and G. Huber, *Growth of high-melting sesquioxides by the heat-exchanger method*, J. Cryst. Growth, **237-9** (2002) 879-83.

[Pet02b] K. Petermann, L. Fornasiero, E. Mix and V. Peters, *High melting sesquioxides: crystal growth, spectroscopy, and laser experiments*, Opt. Mater., **19** (2002) 67-71.

[Pet05] K. Petermann, D. Fagundes-Peters, J. Johannsen, M. Mond, V. Peters, J. J. Romero, S. Kutovoi, J. Speiser, A. Giesen, *Highly Yb-doped oxides for thin-disk lasers*, J. Cryst. Growth, **275** (2005) 135-40.

[Pie01] L. van Pieterson, *Charge Transfer and* $4f^{n} \leftrightarrow 4f^{n-1}5d$ *Luminescence of Lanthanide Ions.* Proefschrift, Universiteit Utrecht, 2001.

[Pur46] E. M. Purcell, *Spontaneous Emission Probabilities at Radio Frequencies*, Phys. Rev., **69** (1946) 681.

[Rab04] L. Rabisch, *Ultradünne, Eu-dotierte, thermisch aufgedampfte Sesquioxid-Schichten auf* α-Al_2O_3*-Substraten.* Dissertation, Institut für Laser-Physik, Universität Hamburg, 2004.

[Rot60] R. S. Roth and S. J. Schneider, *Phase equilibria in the systems involving the rare-earth oxides*, J. Res. Nat. Bur. Stand., **64A** (1960) 309.

[Sae93a] K. L. Sanger, *Pulsed laser deposition: Part I – A review of process characteristics and capabilities*, Proc. of Adv. Mat., **2** (1993) 1-24.

[Sae93b] K. L. Sanger, *Pulsed laser deposition: Part II – A review of process mechanisms*, Proc. of Adv. Mat., **3** (1993) 63-82.

[Sco90] K. Scott, J. M. Huntley, W. A. Phillips, J. Clarke, and J. E. Field, *Influence of oxygen pressure on laser ablation of* $YBa_2Cu_3O_{7-x}$, Appl. Phys. Lett., **57** (1990) 922-4.

[Smi65] H. M. Smith and A. F. Turner, *Vacuum deposited thin films using a ruby laser*, Appl. Optics, **4** (1965) 147-8.

[Son98] J. Sonsky, J. Lancok, M. Jelinek, J. Oswald, and V. Studniska, *Growth of active Nd-doped YAP thin-film waveguides by laser ablation*, Appl. Phys. A, **66** (1998) 583-6.

[Ste00] C. Stewen, M. Larionov, A. Giesen, K. Contag, *Yb:YAG thin disk laser with 1kW output power* (in *OSA Trends in Optics and Photonics. Vol. 34. Advanced Solid-State Lasers.* /ed. by H. Inejeyan, U. Keller, C. Marschall), Opt. Soc. America, Washington, DC, USA, 2000.

[Tom86] T. Tomiki, J. Tamashiro, Y. Tanahara, A. Yamada, H. Fukutani, T. Miyahara, H. Kato, S. Shin, and M. Ishigame, *Optical Spectra of* Y_2O_3 *Single Crystals in VUV*, J. Phys. Soc. Jpn., **55** (1986) 4543.

[Tro04] A. C. Tropper, H. D. Foreman, A. Garnache. K.G: Wilcox, and S. H. Hoogland, *Vertical-external-cavity semiconductor lasers*, J Phys. D: Appl. Phys., **37** (2004) R75-R85.

[Ubi04] S. B. Ubizskii, A. O. Matkovskii, S. S. Melnyk, I. M. Syvorotka, V. Müller, V. Peters, K. Petermann, A. Beyertt, and A. Giesen, *Optical properties of epitaxial YAG:Yb films*, phys. stat. sol. (a), **201** (2004) 791-7.

[Via00] B. Viana, O. Pons-y-Mall, N. Degory, E. Antic-Fidaneev, E. Millun, J. Perriere, C. Beloue, *Optical properties of rare earth doped yttrium oxide waveguides* (in *Conference Digest. 2000 Conference on Lasers and Electro-Optics Europe*), 2000, p.384.

[Vog05] A. Vogel, J. Noack, G. Hüttman, and G. Paltauf, *Mechanisms of femtosecond laser nanosurgery of cells and tissues*, Appl. Phys. B, **81** (2005) 1015-47.

[Xu91] Y.-N. Xu and W. Y. Ching, *Self-consistent band structures, charge distributions, and optical-absorption spectra in MgO, α-Al_2O_3, and $MgAl_2O_4$*, Phys. Rev. B, **43** (1991) 4461.

[Xu97] Y.-N. Xu, Z.-q. Gu, and W. Y. Ching, *Electronic, structural, and optical properties of crystalline yttria*, Phys. Rev. B, **56** (1997) 14993-15000.

[Xu99] Y.-N. Xu and W. Y. Ching, *Electronic structure of yttrium aluminum garnet ($Y_3Al_5O_{12}$)*, Phys. Rev. B, **59** (1999) 10530-35.

[Yar89] A. Yariv, Quantum Electronics (John Wiley & Sons, New York, 1989).

[Zel98] D. E. Zelmon, D. L. Small, and R. Page, *Refractive-index measurements of undoped yttrium aluminum garnet from 0.4 to 5.0 μm*, Appl. Optics, **37** (1998) 4933-5.

[Zve67] G. M. Zverev, G. Ya. Kolodnyi, I. Smirnov, *Optical Spectra of Nd^{3+} Single Crystals of Scandium and Yttrium Oxides*, Opt. Spectrosc. (USSR), **32** (1967) 325-7.

Acknowledgments

This thesis results from more than three years of research at the Institute of Laser Physics in Hamburg. It would not be possible without the help, assistance and support of many people.

First of all I would like to thank my supervisor Prof. Dr. Günter Huber for the opportunity of the interesting PhD studies in the “Solid State Lasers” group and support in accomplishing of this thesis. Also a lot of thanks to all members of the group for the wonderful spirit both at work and at leisure time. Special thanks goes to Dr. Sebastian Bär, Dr. Hanno Scheife, and Dr. Klaus Petermann for proofreading of this thesis and for the numerous discussions, advices, and explanations – whether related to the physics or concerning the “deutsche Sprache, Behörden, Gesetze, ...”.

Many greetings to all my former and current 'neighbours', who shared the office with me – Dr. Bert Neubert, Dr. Eugen Osiac, Dr. Takugo Ishii, Björn Michaelsen, and René Hartke. I enjoyed your company.

A lot of experiments have been made together with my colleagues. So, a big thanks to Friedjof Tellkamp, who helped to recondition the PLD-machine after “it happened again”, Stefan Ehlert, together with whom the first ever PLD-films were grown, Andreas Kahn, who 'guided' the waveguide experiments, Dr. Katja Rademaker, who suggested to make stripes, not films, Dr. Volker Peters, who teached me the 'real' crystal growth, Dr. Lutz Rabisch, for being ready to help anytime, and Bilge Ileri, for the 'last minute' measurements.

The technical assistance of Silke Frömmig, Robert Fischer, and Stephan Garbers helped to make many things faster and easier.

In the course of this work a number of collaborations arose. They excited many new ideas and allowed to realize the experiments, which would not be possible otherwise. So, many thanks to ...

... Dr. Gregory Stryganyuk and Prof. Dr. Georg Zimmerer at SuperLumi for a lot of opportunities to use the station, for assistance in the measurements and helpful discussions.

... Michael Pfeifers, Christian Krug, and Prof. Dr. Christoph Platte at Fachhochschule Wedel for the multiple possibilities to use their X-ray diffractometer.

... Dr. Vasilis Apostolopoulos and Dr. Marcus Pollnau at the EPF de Lausanne for the introduction into the field of waveguides.

... Klaudia Hagemann, Manfred Spiwek, and Horst Schulte-Schrepping at HasyLab for providing the X-ray machine for crystal orientation.

... Thomas Lipinsky at the Forschungszentrum Jülich for the Ar^+-beam etching experiments.

... Jan Podbielski at the Institut für Angewandte Physik for the fabrication of the photoresist mask for the lift-off experiments.

Last but not least, I would like to thank my friends, family, and especially Lena, who supported me outside of the work and helped to make all this possible.

This work was financially supported through the Graduiertenkolleg no. 463 “Spektroskopie an lokalisierten atomaren Systemen” funded by the Deutsche Forschungsgemeinschaft.